Nejdet PARAN

Ph.D. Thesis

AGU 2024

# HIGH-ENERGY COSMIC AND GAMMA RADIATION MEASUREMENT WITH REMOTE-CONTROLLED SECONDARY EMISSION IONIZATION CALORIMETRY MODULES

Ph.D. THESIS
SUBMITTED TO THE DEPARTMENT OF ELECTRICAL AND COMPUTER ENGINEERING
AND THE GRADUATE SCHOOL OF ENGINEERING AND SCIENCE
OF ABDULLAH GUL UNIVERSITY
IN PARTIAL FULFILLMENT OF THE REQUIREMENTS
FOR THE DEGREE OF
DOCTOR OF PHILOSOPHY

By
Nejdet Paran
August 2024

# HIGH-ENERGY COSMIC AND GAMMA RADIATION MEASUREMENT WITH REMOTE-CONTROLLED SECONDARY EMISSION IONIZATION CALORIMETRY MODULES

Ph.D. THESIS

SUBMITTED TO THE DEPARTMENT OF ELECTRICAL AND COMPUTER ENGINEERING

AND THE GRADUATE SCHOOL OF ENGINEERING AND SCIENCE OF ABDULLAH GUL UNIVERSITY

IN PARTIAL FULFILLMENT OF THE REQUIREMENTS

FOR THE DEGREE OF

DOCTOR OF PHILOSOPHY

By

Nejdet Paran

August 2024

## SCIENTIFIC ETHICS COMPLIANCE

I hereby declare that all information in this document has been obtained in accordance with academic rules and ethical conduct. I also declare that, as required by these rules and conduct, I have fully cited and referenced all materials and results that are not original to this work.

Name Surname: Nejdet PARAN
Signature :

## REGULATORY COMPLIANCE

Ph.D. thesis titled "**High-Energy Cosmic and Gamma Radiation Measurement with Remote-Controlled Secondary Emission Ionization Calorimetry Modules**" has been prepared in accordance with the Thesis Writing Guidelines of the Abdullah Gül University, Graduate School of Engineering & Science.

| Prepared By | Advisor | Co-Advisor |
|---|---|---|
| Nejdet PARAN | Assoc. Prof. Burak TEKGÜN | Assoc. Prof. Emrah TIRAŞ |

Head of the Electrical and Computer Engineering Program

Assoc. Prof. Samet GÜLER

## ACCEPTANCE AND APPROVAL

Ph.D. thesis titled "**High-Energy Cosmic and Gamma Radiation Measurement with Remote-Controlled Secondary Emission Ionization Calorimetry Modules**" and prepared by Nejdet PARAN has been accepted by the jury in the Electrical and Computer Engineering Graduate Program at Abdullah Gül University, Graduate School of Engineering & Science.

26/08/2024

**JURY:**

Advisor : Assoc. Prof. Dr. Burak TEKGÜN

Co-Advisor: Assoc. Prof. Dr. Emrah TIRAŞ

Member : Prof. Dr. Mehmet ŞAHİN

Member : Prof. Dr. Mehmet ERTAŞ

Member : Assoc. Prof. Dr. Ali Rıfat BOYNUEĞRİ

Member : Asst. Prof. Dr. Talha ERDEM

**APPROVAL:**

The acceptance of this Ph.D. thesis has been approved by the decision of the Abdullah Gül University, Graduate School of Engineering & Science, Executive Board dated ….. /….. / …….. and numbered ……..……. .

…….. /…….. / ……..
Graduate School Dean
Prof. Dr. İrfan ALAN

# ABSTRACT

# HIGH-ENERGY COSMIC AND GAMMA RADIATION MEASUREMENT WITH REMOTE-CONTROLLED SECONDARY EMISSION IONIZATION CALORIMETRY MODULES

Nejdet PARAN
Ph.D. in Electrical and Computer Engineering
Advisor: Assoc. Prof. Dr. Burak TEKGÜN
Co-Advisor: Assoc. Prof. Dr. Emrah TIRAŞ
August 2024

The demand for precise, robust, and reliable radiation-resistant particle detectors and ionization calorimeters intensifies, due to the escalating luminosity and unprecedented radiation conditions at particle colliders and accelerators. Secondary Emission (SE) Ionization Calorimetry is a novel technology designed to measure the energy of electromagnetic and hadronic particles, particularly in extreme radiation conditions. In this study, we have tested and investigated the development and radiation test of the novel SE modules. The modules were developed by modifying the conventional Hamamatsu single anode R7761 Photomultiplier Tubes. Three different voltage conditions for the same module were developed and the new modules were tested by using cosmic, gamma (Co-60) and neutron (AmBe) radiation sources. The results show that all three modes have good sensitivity to electromagnetic showers, and they are suitable for harsh radiation environments. This study also shows that SE module is a promising technology shedding light on future radiation-resistant nuclear and high-energy detectors. Here, we discuss the technical design, test characteristics and cosmic and particle interaction results of the newly developed SE modules. Since such detector systems are either in a high radiation area or in a closed room/box, remote mode changes allow us to continue the experimental process without interruption. By adding these signals to the interface where the modes are controlled, we can instantaneously observe the modes' effects.

*Keywords: Secondary Emission Ionization Calorimetry, Cosmic Radiation, Radiation Detectors, Particle Detectors, PMTs.*

# ÖZET

# UZAKTAN KONTROLLÜ İKİNCİL EMİSYON İYONİZASYON KALORİMETRİ MODÜLLERİ İLE YÜKSEK ENERJİLİ KOZMİK VE GAMA RADYASYON ÖLÇÜMÜ

Nejdet PARAN
Elektrik ve Bilgisayar Mühendisliği Anabilim Dalı Doktora
Tez Danışmanı: Doç. Dr. Burak TEKGÜN
İkinci Tez Danışmanı: Doç. Dr. Emrah TIRAŞ
Ağustos 2024

Parçacık çarpıştırıcıları ve hızlandırıcılarında artan parlaklık ve çok yüksek radyasyon koşulları nedeniyle hassas, sağlam ve güvenilir radyasyona dayanıklı parçacık dedektörleri ve iyonizasyon kalorimetrelerine olan talep artmaktadır. İkincil Emisyon (SE) İyonizasyon Kalorimetrisi, özellikle aşırı radyasyon koşullarında elektromanyetik ve hadronik parçacıkların enerjisini ölçmek için tasarlanmış yeni bir teknolojidir. Bu çalışmada, yeni SE modüllerinin geliştirilmesini ve radyasyon ölçümü test ettik ve araştırdık. Modüller, geleneksel Hamamatsu tek anotlu R7761 Foto çoğaltıcı Tüpleri modifiye edilerek geliştirilmiştir. Aynı modül için üç farklı voltaj modu geliştirilmiş ve yeni modüller kozmik, gama (Co-60) ve nötron (AmBe) radyasyon kaynakları kullanılarak test edilmiştir. Sonuçlar, her üç modun da elektromanyetik akıya karşı iyi bir duyarlılığa sahip olduğunu ve zorlu radyasyon ortamları için uygun olduklarını göstermektedir. Bu çalışma aynı zamanda SE modülünün gelecekteki radyasyona dayanıklı nükleer ve yüksek enerjili dedektörlere ışık tutan umut verici bir teknoloji olduğunu göstermektedir. Burada, yeni geliştirilen SE modüllerinin teknik tasarımı, test özellikleri ve kozmik ve parçacık etkileşim sonuçları tartışılmaktadır. Bu tür dedektör sistemleri ya yüksek radyasyonlu bir alanda ya da kapalı bir oda/kutu içerisinde olduğu için uzaktan kontrol ile mod değişimleri deneysel süreci kesintiye uğratmadan devam ettirmemizi sağlar. Bu sinyalleri modların kontrol edildiği arayüze ekleyerek modların etkilerini anlık olarak gözlemleyebiliriz.

*Anahtar kelimeler: İkincil Emisyon İyonizasyon Kalorimetrisi, Kozmik Radyasyon, Radyasyon Dedektörleri, Parçacık Dedektörleri, PMT'ler.*

# Acknowledgements

First and foremost, I extend my deepest gratitude and sincere appreciation to my advisor, Assoc. Prof. Burak TEKGÜN and Co-advisor Assoc. Prof. Emrah TIRAŞ. Their constant support and insightful guidance have been invaluable throughout my Ph.D. journey.

My cordial thanks also extend to Prof. Dr. Mehmet ERTAŞ, Prof. Dr. Mehmet ŞAHİN, Asst. Prof. Talha ERDEM and Assoc. Prof. Ali Rıfat BOYNUEĞRİ for serving on my dissertation defense committee.

I thank the Office of the Dean for Research for providing the Lab's infrastructure at the ARGEPARK building of Erciyes University and the Proofreading & Editing Office for proofreading the fourth chapter.

I am grateful for the financial support provided by Scientific Research Projects (BAP) of Erciyes University, Türkiye, under the grant contracts of FBA-2022-12207, FBG-2022-11499 and FDS-2021-11525.

Finally, my sincere appreciation goes to my family. Their patience, continuous support, and encouragement have been a source of strength in my pursuit of this thesis.

# TABLE OF CONTENTS

# LIST OF FIGURES

# LIST OF TABLES

# LIST OF ABBREVIATIONS

| | |
|---|---|
| CDF | Collider Detector at Fermilab |
| CERN | Conseil Européen pour la Recherche Nucléaire / The European Organization for Nuclear Research |
| COBE | Cosmic Background Explorer |
| CMB | Cosmic Microwave Background |
| CSV | Comma-Separated Values |
| Dy | Dynode |
| ENF | Excess Noise Factor |
| EMF | Electromotive Force |
| eV | Electron-Volt |
| FERMILAB | Fermi National Accelerator Laboratory |
| FWHM | Full Width at Half Maximum |
| GUI | Graphical User Interface |
| JP | Jumper |
| LHC | Large Hadron Collider |
| MCP-PMT | Photomultiplier Tubes Incorporating Microchannel Plates |
| nm | nanometer |
| PMT | Photomultiplier Tube |
| PCB | Printed Circuit Board |
| SE | Secondary Emission |
| SER | Single Electron Response |
| SM | Standard Model |
| UV | Ultraviolet |
| WFM | Waveform |

*Sevgili eşim ve çocuklarıma*

# Chapter 1

# Introduction

In high-energy and nuclear physics, one of the most applied methods to measure the momentum and energies of particles is energy measurement with calorimetry. Calorimeters are based on converting particle showers formed by primary particles into first light using crystal, quartz, or plastic scintillators and then electric signals using a photodetector. In high radiation environments, calorimeters made of crystalline materials or plastic scintillators need help in terms of long-term signal efficiency and calibration. In addition, they are usually unsuitable for fast and narrow-band signal production for fast triggering and event selection algorithms. Although the quartz-based calorimeters can produce fast and narrow-band signals and are very resistant to high radiation, the amount of signal produced per charged particle (photoelectron/GeV) is low, and they are primarily sensitive to the electromagnetic core of the hadronic showers. They might be used in detector areas that do not require high energy resolution or can be improved to get higher scintillation light. Therefore, most calorimeter research and development studies focus on new active material, radiation resistance, and high light yield due to particle interactions and detector designs to fill this gap.

## 1.1 Motivation and Objectives

Secondary Emission Ionization (SE) calorimetry is a novel technique to measure electromagnetic shower particles in extreme radiation environments [1–3]. There has been ongoing research and development studies on the SE calorimetry concept, but there are still many areas that need to be filled in terms of remote controllable electronics, and independent active modes. Also, some of the developed modes previously were tested with high-energetic protons, but there wasn't a comprehensive study with different sub-atomic particles such as cosmic particles, gamma and neutron radiation [2–5]. The

motivation of this study is to develop and produce a remotely controllable baseboard for SE calorimetry and similar calorimetric applicationsand characterize the newly developed module with cosmic, gamma, and neutron sources. n this thesis, the traditional PMT bias circuit is modified and re-designed for multiple anode signal outputs for characterization of different operation modes. The design of different operation modes, characterization measurements of both secondary emission modes and the traditional PMT mode are studied in detail. The required sensor front-end and back-end circuits are designed to enable the different operating modes, which allow fault-tolerant operation of SE calorimetry in radiation-harsh environments. In addition, a remote-control circuit with a computer interface program is designed to switch between different operating modes, which facilitates working with complex detector systems.

In this thesis, the design and implementation of front-end and back-end electronic circuit systems for such a calorimeter module focuses on multi-operating modes and remote-control features. We aim to have sensitive SE detector modules for electromagnetic shower particles as well as neutron radiation.

## 1.2 Thesis Outline

The following is an outline of how the remaining content of this thesis is structured.

The second chapter, a crucial foundation of our study, delves into the extensive literature on radiation and its detectors. Here, we provide comprehensive definitions, elucidating the intricate working principles of radiation detectors. After a brief overview of other detector types, our focus shifts to photomultiplier tube detectors, the core of our research. We meticulously explain the structure and working principle of photomultiplier tubes, including the intricate components such as the photocathode, dynode, anode, and input window. The parameters that shape the spectral response characteristics of a photocathode are thoroughly analyzed. Lastly, we specify the dimensions, pin names, and locations of the R7761 PMT, a key component in our study.

The third chapter meticulously details the preparatory phase of the testing process, a crucial step in our thesis. This phase involves a series of carefully planned and executed procedures to ensure the accuracy and reliability of our results. This chapter explains

the Secondary Emission Ionization (SE) calorimetry technique. It also discusses the design and manufacturing of the electronic board for the operation of the R7761 detector. Here, the differences in the design of manual-control and remote-control electronic boards are simulated and explained. Finally, the interface program to control the remote-control board via computer is discussed. In addition, we analyze the voltage-dependent signal size, dark current and gain measurements of the PMT we use.

In the fourth chapter, we begin by providing a comprehensive understanding of the technical background necessary for the experimental process. We then move on to the testing of the electronic cards obtained for the thesis study with the R7761 photomultiplier tube, and the results are meticulously evaluated. We also provide detailed information about the work carried out to solve the problems that occur in particle detectors operating in high-radiation environments. One of these solutions, the secondary electron calorimeter, is discussed. Finally, we present and interpret the graphs of the results of our tests with cosmic and gamma rays.

In the fifth chapter, we evaluate the results we have found throughout the thesis, especially in the fourth chapter. The graphs found as a result of the testing process are explained and interpreted.

In the last chapter, after giving a conclusion, we discuss how our work contributes to social and scientific studies and provide information about possible future studies.

# Chapter 2

# Literature Review and Background

## 2.1 Introduction

In this chapter, after giving general information about radiation, some types of radiation are explained. The standard model of particle physics is briefly explained. After describing the types of detectors used in particle detection, we give a description of the working principles of radiation detectors. After a brief overview of other types of detectors, our focus shifted to the subject of our research, photomultiplier tube detectors. We describe the structure and working principle of photomultiplier tubes, including the components of photomultiplier tubes such as photocathode, dynode, anode, and input window. The parameters that shape the spectral response characteristics of a photocathode are described. Finally, we specify the dimensions, pin names and locations of the R7761 PMT we used in our study.

## 2.2 Definition of Radiation and Some Types of Radiation

Radiation is the transmission or emission of energy in particles or waves through a material medium or space. Radiation consists of nuclei and subatomic matter, and non-matter particles. These particles can be charged or neutral heavy particles (e.g., protons, neutrons, electrons, nuclei, and nuclear fragments) and massless neutral particles such as X-rays and γ rays. The laws that govern subatomic particle interactions determine the mechanisms by which radiation impacts the surrounding world. This includes Electromagnetic radiation, particle radiation, acoustic radiation and gravitational radiation.

Modern particle accelerators like CERN-LHC may measure lengths up to $10^{-21}$ m. [6]. At this distance, neither the electron nor the quarks have any observable substructure. Therefore, as of today, quarks and electrons are the fundamental building blocks of atoms. Besides the electron and quarks, other fundamental particles such as muon, tau have been observed. Also, there is antimatter which was introduced in 1928 by Paul Adrien Maurice Dirac [7], and an antielectron ($e^+$) is more commonly called a positron, was found in 1932 by Carl D. Anderson [8].

A subatomic particle is one of the particles that make up an atom. Based on the Standard Model (SM), a subatomic particle can be either a composite particle or an elementary particle. A composite particle (for example, a proton, neutron, or meson) is one that contains two or more elementary particles. An elementary particle (for example, an electron, photon, or muon), also known as a fundamental particle, is not composed of other particles. Particle physics and nuclear physics investigate these particles and their interactions.

There are four fundamental forces of nature; gravitational, electromagnetic, strong nuclear, and weak nuclear. The interaction between elementary particles occurred by applying one or more of those forces. The main factor that determines which force will act significantly is the distance between them. Electroweak interaction means the unifying electromagnetic force and weak nuclear force in a mathematical description. Electroweak interactions affect all quarks and leptons. Neutrinos have no electric charge. Hence, they solely communicate through the weak force. Quarks (at distances of $10^{-18}$m) only feel the strong nuclear force.

## 2.3 Natural Source of Radiation

Whether they are charged or neutral particles, described by the term radiation. However, all elementary particles can be considered a form of radiation. In the vast universe, we find a multitude of radiation sources. These sources can be scientifically categorized into two main groups: natural and artificial. Natural radiation, which we encounter daily, originates from terrestrial, solar, or astronomical sources. These natural radiation sources are a part of our everyday lives, even if we don't always realize it [6].

### 2.3.1 Cosmic Microwave Background

The cosmic microwave background (CMB) is a unique form of radiation. It is the low-energy photons emitted from other galaxies that permeate the entire universe. This radiation, scattered throughout the universe, has a distinct millimeter-sized wavelength and appears as a glow. It is a thermal radiation that occurred about 380,000 years after the Big Bang, providing valuable information about that time. It is considered a relic of the early universe. Measured at a temperature of 2,725 kelvin, corresponding to the thermal radiation of a blackbody with a frequency of 160.2 GHz and a wavelength of 1.9 mm, it was precisely measured outside the atmosphere by the Cosmic Background Explorer (COBE) satellite.

The discovery of cosmic background radiation in 1964 by Penzias and Wilson was a groundbreaking moment in the field of astrophysics and cosmology. Using a horn reflector antenna at the Crawford Hill Laboratory [9,10], they stumbled upon a residual at a temperature of 3.5 ± 1.0 K while attempting to estimate the contribution of radiation with a wavelength of 7.3 cm. This marked the first tangible evidence of the cosmic microwave background Radiation. The CMB spectrum was later measured by the COBE satellite between 1989 and 1993, confirming the temperature radiation to be close to the emission of a black body with a temperature of T = 2.726 ± 0.010 K [11,12].

### 2.3.2 Cosmic Radiation

There is a continuous flux of particles reaching the Earth from galaxies in the Universe. When particles from the cosmic flux enter the Earth's atmosphere, they interact with particles in the atmosphere and produce a series of particles. These produced particles descend on the Earth like cosmic rain. These stable particles or nuclei entering the Earth's atmosphere have lifetimes of one or several million years. In astrophysical sources, accelerated cosmic radiation is called a 'primary' source (proton, electron, helium nucleus, etc.). These primary particles can interact with interstellar gas, producing a secondary type of cosmic radiation (antiprotons, positrons, etc.). Therefore, the diversity and density of particles in the atmosphere varies with altitude [6,13,14].

Two important instances of nucleon interactions between cosmic radiation and the atmosphere are as follows:

$$n + 14\mathrm{N} \rightarrow p + 14\mathrm{C}, \tag{2.1}$$

$$p + 16\ \mathrm{O} \rightarrow n + \pi + X. \tag{2.2}$$

The first reaction is the Carbon-14 (radiocarbon) method for dating organic materials. In the second reaction, muons and neutrinos are the products of the decay chain of charged mesons and pions produced in the upper layers of the atmosphere. Muons and neutrinos are the most abundant particles at altitudes up to about 4,000 meters, a significant altitude limit due to the decreasing density of the atmosphere with increasing altitude [15–17].

### 2.3.3 Solar Radiation

Solar radiation is a component of cosmic radiation that originates from the sun. Solar radiation consists of large particles such as protons and electrons from the sun's surface, electromagnetic radiation, and neutrinos from the nucleus. The ultraviolet part of the electromagnetic spectrum is the only harmful radiation that reaches sea level. At a temperature of 5,776 K, the spectrum of a blackbody is the same as the electromagnetic radiation of the sun. The majority of neutrinos are generated by the $p + p \rightarrow {}^{2}_{1}\mathrm{D} + e^{+} + v_e$ process called the *p-p* chain. More energetic neutrinos are produced by the so-called *p-e-p* reaction, $p + e^{-} + p \rightarrow {}^{2}_{1}\mathrm{D} + v_e$ ($E_{v_e} = 1.442$ MeV), or by the ${}^{8}_{5}\mathrm{B} \rightarrow {}^{8}_{4}\mathrm{Be}^{*} + e^{+} + v_e$ reaction (up to 15 MeV). The solar neutrino flux was first measured by the Homestake experiment [18].

### 2.3.4 Natural Radioactivity

There exist three distinct categories of natural radiation sources: cosmic, terrestrial, and interior. A nucleus is identified by its atomic number and mass number, which represent the number of protons and neutrons it includes, respectively. These values are often represented using letters and numbers. The most common types of nuclear emissions are referred to as β, γ and α decays. Table 2.1 summarize a concise overview of the primary forms of radiation generated by naturally occurring radioactive processes.

**Table 2.1 Table of some types of natural radioactive radiation.**

| Name | Particle Type | Origin | Charge [$e$] | Mass [$\mathrm{MeV}/c^2$] | Energy distribution |
|---|---|---|---|---|---|
| $\boldsymbol{\alpha}$ | $2p2n$ (nucleus) | Nuclear | +2 | 3.73 | Discrete [MeV] |
| $\boldsymbol{\beta^{\pm}}$ | $e^{\pm}$ | Nuclear | $\pm 1$ | 0.51 | Continuous [keV-MeV] |
| $\boldsymbol{\gamma}$ | EM radiation [$\lambda < 10^{-3}$ nm] | Nuclear | 0 | 0 | Discrete [keV-MeV] |
| Conversion | $e^{-}$ | Nuclear | -1 | 0.51 | Discrete [high keV] |
| Fission fragment | nuclei | Nuclear | $\cong 20$ | 80-160 | Continuous [30-150 MeV] |
| Neutron | n | Nuclear | 0 | 939.6 | Continuous or Discrete [keV-MeV] |
| X-ray | EM radiation [$\lambda \cong 0.01 - 10$ nm] | Atomic shell | 0 | 0 | Discrete [eV-keV] |
| Auger | $e^{-}$ | Atomic shell | -1 | 0.51 | Discrete [eV-keV] |

## 2.4 The Standard Model

The SM of particle physics explains the electromagnetic, weak, and strong forces interaction between elementary particles using the quantum mechanical relativistic theory. The Standard Model also classifies all known elementary particles in the Universe. Elementary particles have several classes. The two main classes are fermions and bosons. Fermions have a spin of 1/2, and they obey the Fermi-Dirac statistics [19,20]. Bosons have a spin of 1, and they obey the Bose-Einstein statistics [21].

## 2.5 Types of Particle Detectors

When a charged particle collides with electrons in atoms, they transfer their energy to the matter in which that atom is located. This energy causes atoms to be excited or ionized. The design of the detector indicates the form of the converted energy. Scintillators convert different types of incoming radiation into photons, helping the detector detect it. Although many different detectors have been developed for different purposes and applications, they all work on the same principle: measuring the incoming radiation by converting the radiation energy into the type of radiation that the detector can detect [22–25].

### 2.5.1 Ionization Detectors

Ionization detectors were the initial electrical devices created for radiation detection [26–30]. A charged particle passed through a gas chamber must have enough energy to ionize a molecule or gas atom along its path. The ions and electrons which ionize cause a current flow that can be measured.

### 2.5.2 Scintillation Detectors

Scintillation detectors are a highly prevalent and extensively utilized instrument for detecting particles. Scintillators are substance that scintillate when exposed to an ionizing radiation. If the scintillator is coupled with a photomultiplier, this combination can convert these scintillations into electrical pulses. These signals, which are first converted from the scintillator and then amplified through the photomultiplier tube and reach the anode, are measured and counted by means of appropriate electronic circuits [22,31].

### 2.5.3 Semiconductor Detectors

The low energy resolution of scintillators is a major constraint in their use. Such meters need to transform the energy from the incoming radiation into light and then produce an electrical pulse. This process occurs in many steps, resulting in reduced efficiency. The small number of statistical fluctuations limits the energy resolution that can be achieved. To address the decrease in energy resolution, it is necessary to augment the quantity of information carriers at each pulse. Using semiconductor detectors may provide more carriers for some radiation phenomena than other detectors. Semiconductor detectors give the highest level of energy resolution among all currently existing spectrometers. Semiconductor detectors possess a small size, rapid timing capabilities, and the ability to be made in any desired thickness. The disadvantages of semiconductor detectors are their small size and reduced efficiency due to damage caused by high radiation environments. Despite these drawbacks, the advantages of semiconductor detectors are a testament to their potential in radiation measurement [32–40].

## 2.6 Photomultiplier Tube (PMT) Detectors

The photoelectric effect, which originated in Hertz's experiments, is one of the earliest examples in modern physics of an observable effect of light's particle/photon nature [41]. An effect that played a crucial role in Einstein's explanation of the nature of light in terms of Planck's energy quantum [42]. The photoelectric effect also played an essential role in developing the photomultiplier tube, a device widely used today for single photon detection over a wide energy range. Since the beginning of the 20th century, the Geiger-Muller tube has been utilized to detect high-energy individual particles and photons in the X-ray and gamma-ray ranges. The detection of single photons at visible or lower energy became possible only after the introduction of the photomultiplier in the late 1930s.

Photomultipliers (PMTs) are very susceptible vacuum tubes that transform light into a quantitative electric current. PMTs are most often coupled with scintillation detectors in high energy and nuclear physics. Thanks to photomultiplier tubes which transform the very poor light output of scintillation signal into an observable electrical pulse, scintillators could widely be used in radiation detection and spectroscopy [43–50].

In many fields, from academia to industry, photomultiplier tubes (PMTs) serve as photodetectors for a variety of applications. Applications of PMTs include radiation monitors, high-energy physics experiments, medical diagnosis, environmental measurements, spectrophotometry, microscopy, life science measurements, non-contact industrial measurements, oil well logging, and solid surface analysis. PMTs are widely used for radiation measurements in nuclear power plants. Today, the loss or theft of nuclear materials has become a serious source of risk. Therefore, it has become very important to inspect and detect these nuclear materials at transfer points at national borders. Photomultiplier tubes with appropriate scintillators are also used for various radiation inspections [51–54]. In addition, a new field of application has emerged known as secondary emission ionization calorimetry in recent years. Calorimeters quantify the energy of secondary particles resulting from particle interactions [55]. Calorimeters are devices that transform the energy of particles into either light or an electric charge when discharged into matter. Typically, this is quantified using detectors that comprise an

inorganic scintillator, plastic scintillators and heavy metals combined with a photomultiplier tube.

### 2.6.1 Light Sensing

Photon detectors convert the information carried by light into an electrical analog signal. The time response of a detector is usually specified regarding some property of the pulse shape, such as rise time, or the response can be described in terms of bandwidth. All detectors are sensitive to the wavelength of a signal but cannot determine it directly; this requires additional instrumentation, such as a monochromator. Light detection is a complex quantum mechanical process that absorbs the energy of a photon to produce a free electron. Given sufficient photoelectron production per unit time, this intricate process allows us to measure this charge in terms of a current or voltage to measure the light input.

Photomultiplier (PMT) detectors, a significant milestone in light detection, are often used at infrared wavelengths with very low quantum efficiencies. Thanks to their high and relatively noise-free gain, PMTs can detect single photoelectrons. Until the 1970s, PMTs were the only commercially available detector capable of detecting photoelectrons.

Consider the case where a photocathode is illuminated by a random but constant light source, producing an $I_k$ photocurrent. By random, we mean that all frequency components are equally likely. By constant, we mean that the average current measured over sufficiently long, consecutive periods is constant. However, a random component superimposes this current as a result of the quantized nature of light and charge, a phenomenon called the Schottky effect. The rms noise current, $\langle i_s^2 \rangle^{1/2}$, is shot noise and is given by

$$\langle i_s^2 \rangle^{1/2} = (2eI_k\Delta f)^{1/2}, \tag{2.3}$$

where $e$ is the electronic charge and $\Delta f$ is the noise bandwidth. Shot noise exists only when a signal, $I_k$, is present, which can be interpreted as a random but measurable modulation on $I_k$. Equation (2.3) is one of the most important relationships in light measurement. Its impact on light detection is particularly noticeable when light levels are low. An important consequence of Equation (2.3) is that the precise measurement of $I_k$ is

a challenge due to the presence of this intrinsic noise, $\langle i_s^2 \rangle^{1/2}$. In PMT applications, current-to-voltage conversion is realized by including a load resistor, R, at the anode. All resistors are sources of electromotive force (EMF - is a battery's or cell's energy per coulomb (Q) of charge) with associated noise, whose magnitude is given by the Johnson noise formula below:

$$\langle i_j^2 \rangle^{1/2} = \left( \frac{4k\Delta f}{R} \right)^{1/2}. \tag{2.4}$$

where $k = 1.38x10^{-23}$ J/K is the Boltzmann constant, and $T$ is the absolute temperature, usually taken as 300 K. The thermal noise expression in terms of voltage follows Equations (2.4) and (2.5).

$$\langle i_j^2 \rangle^{1/2} = (4kTR\Delta f)^{1/2}. \tag{2.5}$$

It predicts an infinitely noisy EMF for an open circuit (infinite resistance). However, the unavoidable presence of stray capacitance, in addition to that deliberately added for bandwidth control, introduces finite impedance into the signal. At this point, it is worth emphasizing that wherever noise is involved, the appropriate bandwidth is $\Delta f = 1/4RC$ and not $1/2\pi RC$, the more familiar signal bandwidth, although the numerical difference is negligible. Equation (2.5) is then reduced to $\langle i_j^2 \rangle = kT/C$. Assuming typical values for the relevant parameters, comparing the relative contributions to noise from these two primary sources is beneficial.

For example, suppose a photocurrent of $I_k = 10^{-15}$ A corresponds to an average flux of 6300 photoelectrons (pe)/s. While this is a weak signal in terms of PMT, it is not very weak. The bandwidth, $\Delta f$, appears in both noise expressions and is taken as $\Delta f = 1$, R = 1, T = 300, and $\langle g \rangle = 106$ in equations (2.6) - (2.8) below for the current ratio metric analysis. There is no loss of generality, as the formulas can be easily scaled. The mean gain of the multiplier, $\langle g \rangle$ is enclosed in chevrons to emphasize its statistical nature. Shot noise arises from current flow at the photocathode but is enhanced by the multiplier gain $\langle g \rangle$ when observed at the anode. On the other hand, Johnson noise is outside the influence of the PMT because its source lies in an added load resistor. Taking $\Delta f$ and R equal to unity, the contributions from the shot and Johnson noise at the anode are Equations (2.6) and (2.5).

$$\langle i_s^2 \rangle^{1/2} = (2eI_k)^{1/2} \langle g \rangle = (2 \times 1.6 \times 10^{-19} \times 10^{-15})^{1/2} \times 10^6 = 18 \text{ pA}, \tag{2.6}$$

$$\langle i_j^2 \rangle^{1/2} = (4kT/R)^{1/2} = (4 \times 1.38 \times 10^{-23} \times 300)^{1/2} = 129 \text{ pA}. \quad (2.7)$$

The combined noise is given by adding the contributions in quadrature (Equation (2.8)), noting that Equation (2.6) depends on the signal and Equation (2.7) does not.

$$\langle i_{(s+j)^2} \rangle^{1/2} = \left( \langle i_s^2 \rangle^2 + \langle i_j^2 \rangle^2 \right)^{1/2} = (18^2 + 129^2)^{1/2} = 130 \text{ pA}. \quad (2.8)$$

Equations (2.3), (2.4), and (2.8) are plotted in Figure 2.1 as a function of R, considering a unit bandwidth as in standard practice. The graph compares the magnitudes of shot and Johnson noise at the anode for a cathode current of 1015 A and a multiplier gain of 106. The two noise sources have the same magnitude for a load resistance of 50 Ω, a value suitable for signal transmission over coaxial cable. The combined noise is the sum of the two sources taken in quadrature. The quadrature addition procedure makes the net effect of the shot contribution negligible in this case. The two contributions are equal if Equation (2.9)

$$\frac{\langle i_s^2 \rangle^{1/2}}{\langle i_j^2 \rangle^{1/2}} = \left( \frac{2eI_k R}{4kT} \right) \times \langle g \rangle = 1. \quad (2.9)$$

For $I_k = 10^{-15}$ A and $\langle g \rangle = 10^6$, Equation (2.9) shows that R is 50 Ω and independent of $\Delta f$. The Johnson noise in the load resistance determines the most minor measurable cathode current. The main characteristic of an electron multiplier is that it provides current amplification without resistance.

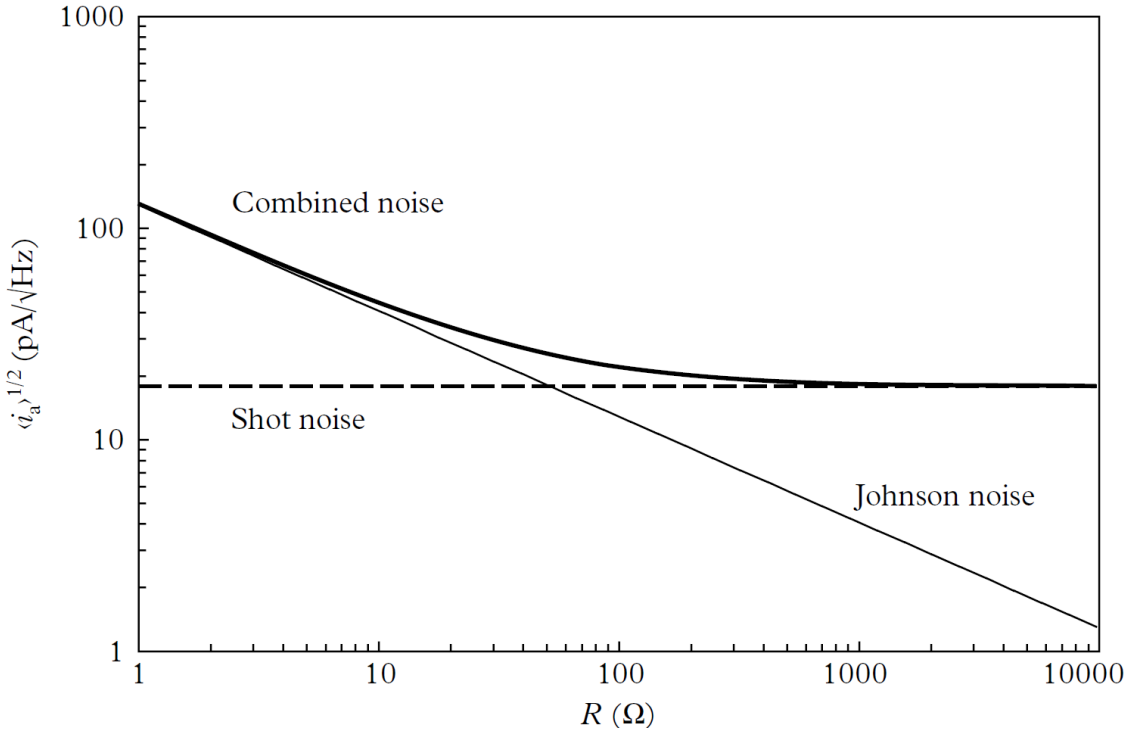


**Figure 2.1**: The graph compares the magnitudes of shot and Johnson noise at the anode for a cathode current of 1015 A and a multiplier gain of 106.

Processing fast, nanosecond rise time output pulses from a detector requires a bandwidth in the region of 100 MHz and preferably a load resistance of 50 Ω, for the reasons given earlier. The combined noise is

$$\langle i_{(s+j)^2} \rangle^{1/2} = \left( \frac{4kT}{R} + 2eI_k \langle g \rangle^2 \right)^{1/2} \times \Delta f^{1/2} = 2.56 \times 10^{-11} \times \sqrt{10^8} = 0.256\ \mu\text{A}. \qquad (2.10)$$

In this example, equal contributions are obtained from the two noise sources.

The effect of the wide bandwidth is to increase the noise from 25.6 pA rms at unity bandwidth to 0.256 μA rms at 100 MHz bandwidth.

Equation (2.11) gives the gain required for multiplier noise to exceed Johnson noise.

$$\langle g \rangle \geq \left( \frac{4kT}{2eI_k R} \right)^{1/2} = \left( \frac{0.052}{I_k R} \right)^{1/2} = \left( \frac{0.052}{10^{-9}} \right)^{1/2}, \langle g \rangle \geq 7000\ . \qquad (2.11)$$

### 2.6.2 DC Detection with a Photomultiplier Tube

A conventional PMT, a key component in photonics and optical detectors, is composed of a photocathode and a current multiplier component within a vacuumed glass envelope. The heart of its amplification lies in an *m*-stage dynode chain, a process rooted

in the principle of secondary emission. In an ideal scenario where we adhere to Poisson statistics, the average stage gain $\delta$ translates into a total gain of $\delta^m$ at the output (anode) of the PMT. This gain, crucial to our understanding, can be expressed as $\langle g \rangle$ or $\delta^m$ depending on the context.

Considering the noise evolution as the signal passes through each dynode stage, the overall mean square noise after the m stages will be the same as in the photocathode for a noise-free multiplier. However, if $\langle i_m^2 \rangle^{1/2} = (2eI_k\Delta f)^{1/2}\delta^m$ is considered, the overall gain will increase the square noise. We assume that the Dinot multiplier is a random phenomenon obeying Poisson statistics. We must modify the shot noise formula to allow for additional noise sources due to the multiplier. This equation requires the inclusion of the factor $\delta^m(\delta^{m+1} - 1)/(\delta - 1)$. When we add this decomposition, we get

$$\langle i_m^2 \rangle = 2eI_k\Delta f\left[\delta^m\left(\frac{\delta^{m+1} - 1}{\delta - 1}\right)\right], \tag{2.12}$$

Dividing $(S/N)_{op}$, the signal-to-noise ratio at the output, by $(S/N)_{ip}$, the signal-to-noise ratio at the input, and substituting the results following equations (2.3) and (2.12), we arrive at equation (2.13)

$$\frac{(S/N)_{op}^2}{(S/N)_{ip}^2} = \frac{\delta^m(\delta - 1)}{(\delta^{m+1} - 1)}. \tag{2.13}$$

In practice, δm+1 greatly exceeds unity; hence,

$$\frac{(S/N)_{op}^2}{(S/N)_{ip}^2} = \frac{\delta - 1}{\delta} = ENF \tag{2.14}$$

ENF stands for excess noise factor (ENF), which represents the ideal performance for an electron multiplier with Poisson statistics. However, the multiplier noise in real PMTs consistently exceeds the value obtained here. The actual ENF value can be calculated from a pulse height distribution without any assumptions on the theoretical value. This, known as the single electron response (SER), is obtained by illuminating the photocathode with a random single photon source. Calculating the variance of an experimental distribution leads to the ENF. ENFs are related to many other light detectors, mainly in how they degrade resolution, as shown in Table 2.2. The table shows the resolution capabilities of various light detectors assuming a preamplifier with an ENC of

1000 electrons, where η is the quantum efficiency (QE), and N is the number of photons in the signal.

Figure 2.2 provides a visual representation of three crucial aspects of an electron multiplier: The signal-to-noise (S/N) ratio diminishes as the number of stages increases; the S/N ratio benefits from an increase in the stage gain; and the first stage, in particular, must have a high gain. Graph showing S/N ratios as a function of the number of dynodes for various tap gains obtained from Equation (2.13). For m = 8, this curve is practically indistinguishable from the curve obtained for $[(\delta - 1)/\delta]^{1/2}$. The graph shows that the S/N ratios rapidly approach unity as δ increases. This latter requirement is easily met by setting $V_{\mathrm{k-d1}}$ higher than the inter-dynode voltages, typically by a factor of 2 to 3. From equation (2.5), it is evident that the rms Johnson noise $\langle i_j^2 \rangle^{1/2}$ increases as $R^{1/2}$. However, the high multiplier gain allows for the use of a relatively small resistance to counteract the contribution of this noise. Moreover, selecting a low-value load resistor ($R$) is essential if a wide bandwidth and, therefore, a good high-frequency response is desired.

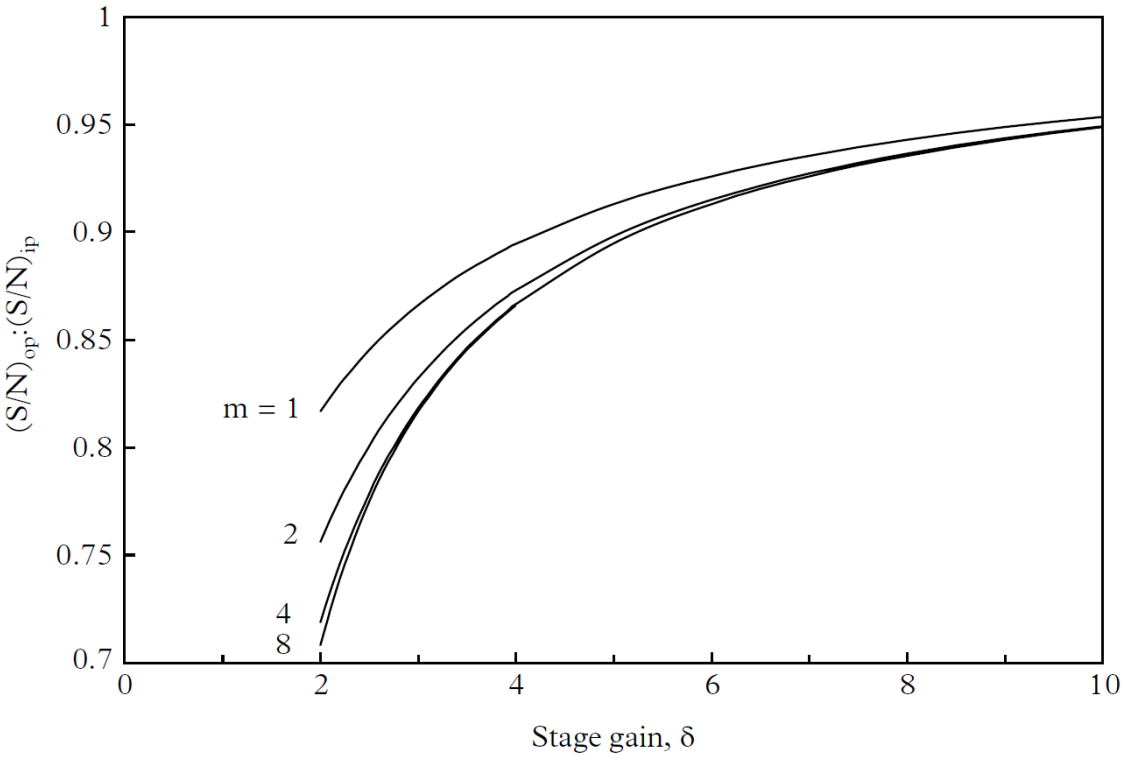


**Figure 2.2** Graph showing S/N ratios as a function of the number of dynodes for various tap gains obtained from Equation (2.13).

### 2.6.3 Light Detectors Categories

Light detectors can be divided into two broad categories: those that provide images and those that do not. The other two main subcategories are vacuum devices such as PMTs, microchannel plate PMTs (MCPPMTs), and hybrid PMTs, and solid-state devices such as PIN diodes, avalanche photodiodes (APDs), pixelated silicon PMs (SiPMs), and charge-coupled devices (CCDs).

**Table 2.2 Table of resolution capabilities of various light detectors assuming a preamplifier with an ENC of 1000 electrons.**

| Detector | η (%) | ENF | $\langle g \rangle$ | Resolution |
|---|---|---|---|---|
| **PMT** | 30 | 1.2 | $10^6$ | $(4/N)^{1/2}$ |
| **Fine-mesh PMT** | 30 | 2.0 | $10^6$ | $(6.7/N)^{1/2}$ |
| **MCPPMT** | 20 | 1.5 | $10^6$ | $(7.5/N)^{1/2}$ |
| **PIN diode** | 80 | 1 | 1 | $[1.25/N + (1250/N)^2]^{1/2}$ |
| **APD** | 80 | 10 | 100 | $[12.5/N + (12.5/N)^2]^{1/2}$ |
| **SiPM** | 30 | 1 | $10^6$ | $(3.3/N)^{1/2}$ |
| **VLPC** | 80 | 1 | $6x10^4$ | $(1.25/N)^{1/2}$ |
| **HPD** | 30 | 1 | $10^3$ | $[3.3/N + (3.3/N)^2]^{1/2}$ |
| **HAPD** | 30 | 1 | $10^5$ | $(3.3/N)^{1/2}$ |
| **Poisson limit** | | | | $(1/N)^{1/2}$ |

### 2.6.4 Structure of Photomultipliers

A photomultiplier tube is a type of vacuum tube typically enclosed in an evacuated glass tube. It includes an input window, a photocathode, focusing electrodes, an electron multiplier, and an anode. The schematic design of a photomultiplier tube is shown in Figure 2.3.

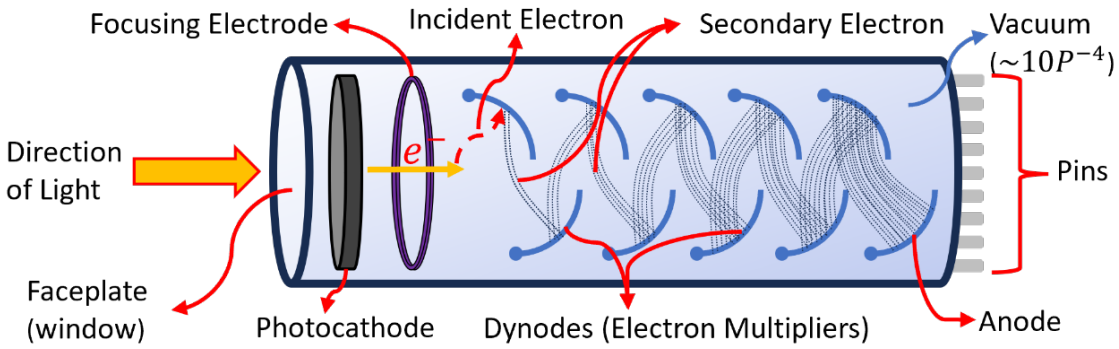


**Figure 2.3** Construction of a photomultiplier tube

The following procedures detect light that enters a photomultiplier tube and generates an output signal.

1. The input window lets light in.

2. External photoelectric effect: The photocathode's electrons are excited by light, releasing photoelectrons into the vacuum.

3. The focusing electrode accelerates and focuses photoelectrons into the first dynode, where secondary electron emission multiplies them. The mentioned secondary emission occurs repeatedly with every subsequent dynode.

4. The anode is ultimately responsible for gathering the amplified secondary electrons released by the final dynode.

### 2.6.5 Basic Characteristics of Photocathodes

This section provides an overview of photocathodes and window materials that have been utilized in practical applications throughout history. It also defines key terms associated with photocathodes, including radiant sensitivity (the ability of a photocathode to transform incoming photons into electrons), luminescent sensitivity (the ability of a photocathode to emit light when excited by photons), and quantum efficiency (electron emissions to photons incident on the photocathode).

### 2.6.5.1 Photocathode materials

Photocathodes typically consist of compound semiconductor materials containing alkali metals. It is preferable for these materials to possess a low work function. Currently, around 10 varieties of photocathodes are employed in real-world applications. Photocathodes are offered in two types: transmission, which is translucent, and reflection, which is opaque. The spectral response is subject to variation based on the specific mix and kind of photocathode and window material. The following are photocathode materials commonly used in photomultiplier tubes [43].

**Cs-I:**

Often referred to as "sun blind," Cs-I has little susceptibility to solar radiation. When it comes to wavelengths less than 115 nanometers, Cs-I is highly sensitive, but around 200 nanometers and beyond, its sensitivity rapidly decreases. Therefore, it is employed for the purpose of detecting UV radiation. Due to its high ultraviolet transmittance, synthetic silica or $MgF_2$ crystal is used as the window material. The $MgF_2$ crystal utilized as the entry window is incapable of transmitting wavelengths that are less than 115nm in length. It can be used to measure light with wavelengths shorter than 115nm by removing the entrance window in a vacuum environment and using a first dynode with Cs-I deposited on it instead of a photocathode.

**Cs-Te:**

Cs-Te, like Cs-I, is called "sun-blind" and lacks sensitivity to wavelengths beyond 300 nm. When using Cs-Te, both the transmission type and the reflection type have the same range of spectral response. However, the reflection type is more sensitive than the transmission type. For the entry window, $MgF_2$ or man-made silica is most often used.

**Sb-Cs:**

This photocathode is widely used in many applications. It has detection sensitivity in the UV and visible regions. The resistance of the Sb-Cs photocathode is reduced compared to that of the bialkaline photocathode. This allows a large current to flow in the cathode, which is useful when the light intensity to be evaluated is comparatively elevated. Sb-Cs is mainly used for reflection-type photocathodes [52,56].

**Bialkali (Sb-Rb-Cs, Sb-K-Cs):**

Because two types of alkali metals are used in these photocathodes, they are called "bialkaline" photocathodes. They provide improved sensitivity by obtaining a spectrum response from the UV to about 700nm. The transmission characteristics of these photocathodes have a spectrum response range that is comparable to that of the Sb-Cs photocathode. However, they possess greater sensitivity and lower levels of dark current. NaI (Tl) is also a commonly employed photocathode for scintillation counting in radiation measurements. Reflection-type bi-alkaline photocathodes employ identical materials, however produced through distinct manufacturing methods.

**High temperature, low noise Bialkali (Sb-Na-K):**

It has the same structure as bi-alkaline photocathodes. While normal bi-alkaline photocathodes can operate at around 50 degrees Celsius, Up to 175 degrees Celsius are not a problem for this photocathode. This allows it to be used in places like oil wells, where it is often exposed to high temperatures. Additionally, it enables the measurement of low-level light, such as applications involving the counting of photons, in an environment with little background noise.

**Multialkali (Sb-Na-K-Cs):**

A Multialkali photocathode is made using more than two kinds of alkali metals. It operates with high sensitivity in the spectral response range from the UV region to the region near 850nm. Because of this wide range, broadband spectrophotometers frequently employ this photocathode. Multialkaline photocathodes with wavelength response up to 900nm are also commercially available.

**Ag-O-Cs:**

Photocathodes using Ag-O-Cs are sensitive to transmission between 300 and 1200nm, while they exhibit a slightly narrower reflection-type spectral response region between 300 and 1100nm. Both reflection-type and transmission-type Ag-O-Cs photocathodes are generally used for detection in the near-infrared region [52,56].

**GaAsP (Cs):**

This conduction-type photocathode is a GaAsP crystal activated with a Cesium atom. In the visible spectrum, it possesses an extremely high quantum efficiency and no sensitivity in the UV region. Compared to alkaline photocathodes, it is more prone to encounter problems. from sensitivity degradation when exposed to high-intensity incident light.

**GaAs (Cs):**

This photocathode is used for both reflection-type and transmission-type photocathodes and is a GaAsP crystal activated with a Cesium atom. This GaAs(Cs) photocathode can sense light from UV to 900 nm and has a very sensitive spectral response curve between 300 and 850 nm. The transmission type can only respond to a smaller range of bands because it absorbs shorter ones. GaAs(Cs) photocathodes are more likely to suffer sensitivity degradation when exposed to high-intensity incident light than alkaline photocathodes.

**InGaAs (Cs):**

Compared to the GaAs photocathode, the InGaAs (Cs) photocathode works in a range of wavelengths that goes into the infrared. In the 900–1000 nm region, it provides a far superior signal-to-noise ratio than the Ag-O-Cs photocathode.

**InP/InGaAsP(Cs), InP/InGaAs(Cs):**

InP/InGaAsP(Cs) and InP/InGaAs(Cs) are field-assisted photocathodes that utilize a PN junction formed by growing InP/InGaAsP or InP/InGaAs on an InP substrate. When a bias voltage is applied to this photocathode, it lowers the transmission band barrier and increases sensitivity at long wavelengths such as 1.4 mm or even 1.7 mm. When these photocathodes are used at room temperature, they generate significant levels of dark current. Consequently, they need cooling to temperatures ranging from -60C to -80C when in operation.

### 2.6.6 Window Materials of Photomultipliers

In the previous section on photocathode materials, which are the light-sensitive materials used in the creation of photomultiplier tubes, we mentioned that the majority of photocathodes have a high level of sensitivity extending to the UV area. Ultraviolet radiation tends to be absorbed by the 'window material', a term used to describe the material that forms the front face of the photomultiplier tube and determines the short wavelength limit. Below are some of the window materials commonly used in photomultiplier tubes today, with some explanations.

**MgF2 crystal**

Alkali halide crystals, while superior in transmitting ultraviolet radiation, are prone to melting. In contrast, the practicality of Magnesium fluoride ($MgF_2$) crystal shines through. Its exceptional resistance to melting makes it a reliable choice as a window material, allowing 'vacuum ultraviolet radiation ', a type of ultraviolet radiation that is not easily transmitted through air, to pass through down to 115 nm.

**Sapphire**

Sapphire consists of $Al_2O_3$ crystal and has a transmittance that falls between that of UV-transmitting glass and synthetic silica in the ultraviolet range. Sapphire glass has a wavelength cutoff of around 150 nm, which is significantly smaller than that of synthetic silica.

**Synthetic silica**

Compared to 'fused silica ', a type of silica that is formed by melting high-purity silica and then cooling it into a glass, synthetic silica has a lower absorption level in the ultraviolet region and transmits ultraviolet radiation down to 160 nm. Silica has a very different coefficient of thermal expansion compared to Kovar alloy used for the body pins (tips) of photomultiplier tubes. This precludes the use of silica as a bulb body. Instead, borosilicate glass is used for the bulb body. A graded seal, which is a seal with a varying coefficient of thermal expansion, is then bonded to the synthetic silica bulb using a cascade of glasses with varying coefficients of thermal expansion. This graded seal is very fragile due to its additive structure, and this must be taken into account when using

these tubes. Another point is that helium gas can pass through the silica bulb, which can cause an increase in noise. Therefore, such tubes should not be operated or stored in the presence of helium.

**UV glass (UV transmitting glass)**

UV glass, as its name suggests, is a remarkably versatile window material that transmits ultraviolet radiation effectively. Its short wavelength segment extends up to 185 nm, demonstrating its adaptability and making it a reliable choice for a wide range of applications.

**Borosilicate glass**

Borosilicate glass, often referred to as 'Kovar glass' due to its close coefficient of thermal expansion to the Kovar alloy used in the ends of photomultiplier tubes, is the most widely used window material. However, it does not transmit UV radiation shorter than 300 nm, limiting its use for detecting radiation shorter than this wavelength.

### 2.6.7 Spectral response characteristics of Photocathode

In a photomultiplier, the photocathode converts the energy of the incident photons into photoelectrons. The conversion efficiency of the photocathode (photocathode sensitivity) depends on the wavelength of the incident light. This relationship between the photocathode and the wavelength of the incident light, known as the spectral response characteristic, is a crucial parameter that defines the performance of a photomultiplier tube. It is expressed in terms of radiation sensitivity and quantum efficiency.

#### 2.6.7.1 Radiation sensitivity

The photoelectric current produced by the photocathode divided by the incident radiation flux at a given wavelength is called radiation sensitivity. The unit of radiant sensitivity is amperes per watt (A/W). Relative spectral response characteristics, where the maximum radiation sensitivity is normalized to 100%, are also suitable for use.

### 2.6.7.2 Quantum efficiency

The quantum efficiency, a key performance indicator, is the ratio of the number of photoelectrons emitted from the photocathode to the number of incident photons. This efficiency, usually expressed as a percentage, is denoted by n. It's important to understand that the photocathode plays a crucial role in this process, as it's where a specific probability process occurs, leading to the emission of photoelectrons. The energies of photons with shorter wavelengths are greater than those with longer wavelengths, increasing the probability of photoemission. This explains why the maximum quantum efficiency occurs at a wavelength slightly shorter than the wavelength of the highest radiosensitivity. Quantum efficiency is defined as

$$\eta(\lambda) = \frac{\text{number of photoelectrons}}{\text{number of incident photons}}. \tag{2.15}$$

### 2.6.7.3 Light sensitivity

A complex setup is required to measure the spectrum response of a photomultiplier tube, which can be both expensive and time-consuming to set up. However, this precision is crucial in our work, as it allows us to evaluate the sensitivity of standard photomultiplier tubes in a more practical way, overcoming the potential disadvantages of this measurement method.

The lux is the unit used to quantify the illuminance on a surface located one meter distant from a point light source with an intensity of one candela (cd). A lumen is the unit used to measure the luminous flux when one lux of light passes across an area of one square meter. Luminous sensitivity refers to the ratio of the output current from the cathode or anode to the luminous flux (measured in lumens) emitted by a tungsten lamp operating at a dissipation temperature of 2856K. The light sensitivity value is a helpful measure for evaluating the sensitivity of photomultiplier tubes of the same kind. It is important to mention that the unit of luminous flux for conventional visual sensitivity is called "lumen". Therefore, photomultiplier tubes that operate within the spectral range of 350 to 750 nm are not acceptable.

Luminous sensitivity is divided into two parameters: cathode luminous sensitivity, which describes the performance of the photocathode in converting light into electric

current, and anode luminous sensitivity, which describes the performance of the anode in amplifying the electric current. Understanding these parameters is crucial for evaluating the overall sensitivity of a photomultiplier tube.

### 2.6.8 Basic Characteristics of Dynodes

This section provides an overview of the common types of dynodes that are currently being used. It also explains their key features, including collection efficiency and current gain. In addition to the type of dynode, the photocathode size and focusing method determine the electrical properties of a photomultiplier tube [57–61].

#### 2.6.8.1 Dynode types and features

There are many types of dynodes available. Each dynode type has a different gain, time response, homogeneity, and secondary electron collection efficiency depending on its construction and number of stages. The application in which it will be used determines which dynode type to choose. Figure 2.4 to Figure 2.11 show cross-sectional views of typical dynodes. The characteristics of these dynode types will be briefly described below. All drawings depicting the dynode types below are by Hamamatsu.

**1. Circular-cage Type Dynode**

The circular cage design offers the benefit of being small and is employed in all side-on photomultiplier tubes and specific head-on photomultiplier tubes. Additionally, it has a rapid time response. Figure 2.4 illustrates the cross-sectional views of circular-cage type dynode.

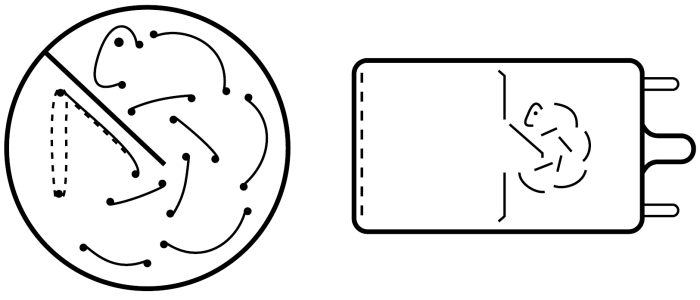

**Figure 2.4** Circular-cage Type Dynode

**2. Box-and-grid Type Dynode**

This variety is widely employed in head-on photomultiplier tubes and has exceptional photoelectron collection efficiency. Thus, photomultiplier tubes employing this dynode provide excellent uniformity and high detection efficiency. Figure 2.5 illustrates the cross-sectional views of box-and-grid type dynode.

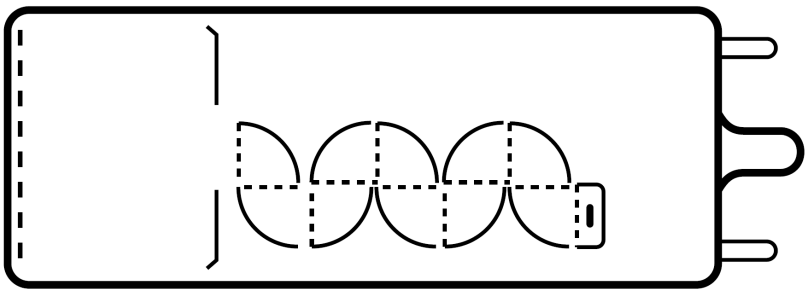

**Figure 2.5** Box-and-grid Type Dynode

**3. Linear-focused Type Dynode**

Similar to box-and-grid types, head-on photomultiplier tubes frequently employ linear-focused types. Its defining characteristics include rapid time response, high time resolution, and exceptional pulse linearity. Figure 2.6 illustrates the cross-sectional views of linear-focused type dynode.

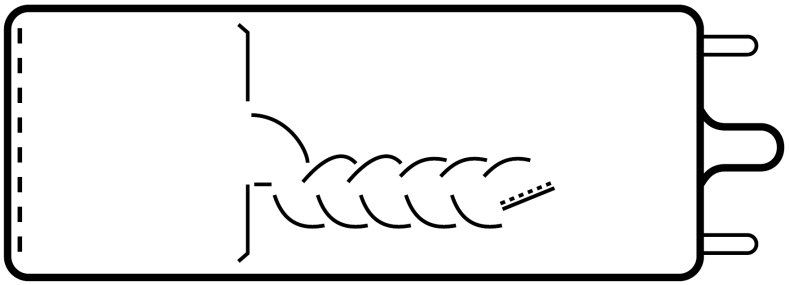

**Figure 2.6** Linear-focused Type Dynode

**4. Venetian Blind Type Dynode**

Venetian blinds are primarily utilized in head-on photomultiplier tubes with a sizable photocathode diameter. They generate an electric field that readily accumulates electrons. Figure 2.7 illustrates the cross-sectional views of venetian blind type dynode.

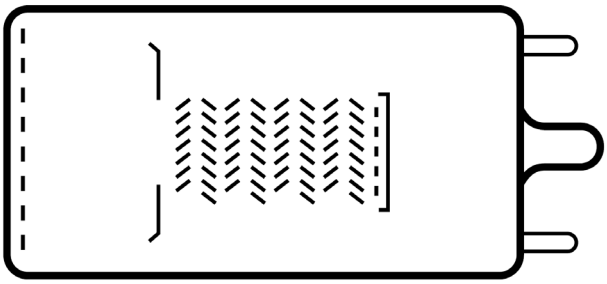

**Figure 2.7** Venetian Blind Type Dynode

**5. Mesh Type Dynode**

This variety of dynodes comprises mesh electrodes layered in close proximity. Two varieties exist: coarse and fine mesh. Both devices exhibit exceptional output linearity and strongly resist magnetic fields. When coupled with a cross-wire anode or multianode, the location of the incident light can be determined. The main purpose of fine mesh types is to support photomultiplier tubes in strong magnetic field applications. Figure 2.8 illustrates the cross-sectional views of mesh type dynode.

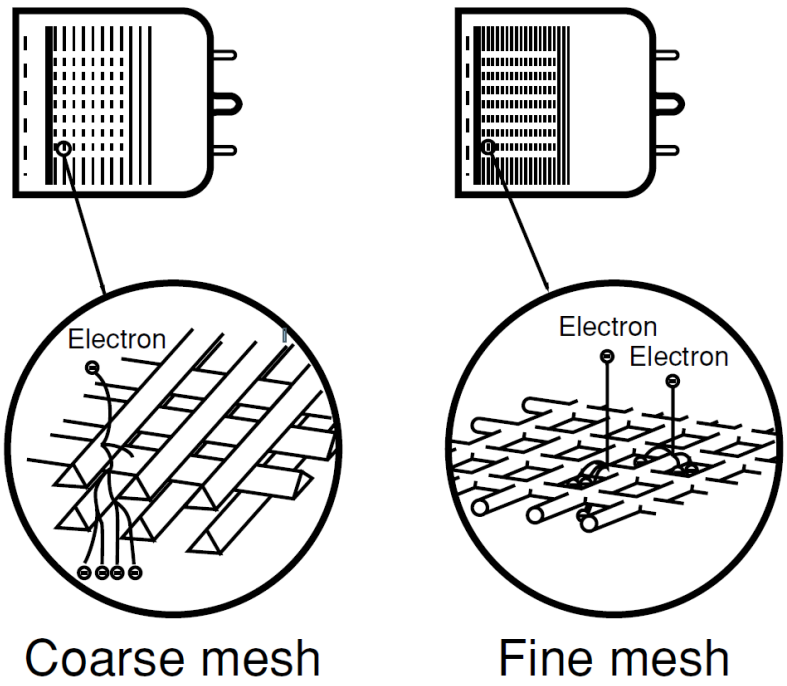


**Figure 2.8** Mesh Type Dynode

### 6. Microchannel Plate Type Dynode

This dynode structure is based on the one mm-thick microchannel plate (MCP). It demonstrates significantly enhanced time resolution compared to alternative discrete dynode structures. Additionally, it provides steady amplification in intense magnetic fields and can detect location when used in conjunction with a certain anode. Figure 2.9 illustrates the cross-sectional views of microchannel plate type dynode.

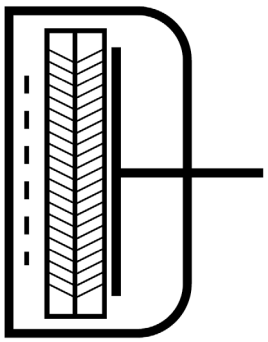

**Figure 2.9** Microchannel Plate Type Dynode

### 7. Metal Channel Type Dynode

The dynode structure comprises very thin electrodes created using advanced micromachining techniques and accurately arranged based on computer simulations of electron paths. Due to the proximity of each dynode, the electron path length is concise, which provides exceptional time characteristics and steady gain, even when subjected to magnetic fields. Figure 2.10 illustrates the cross-sectional views of metal channel type dynode.

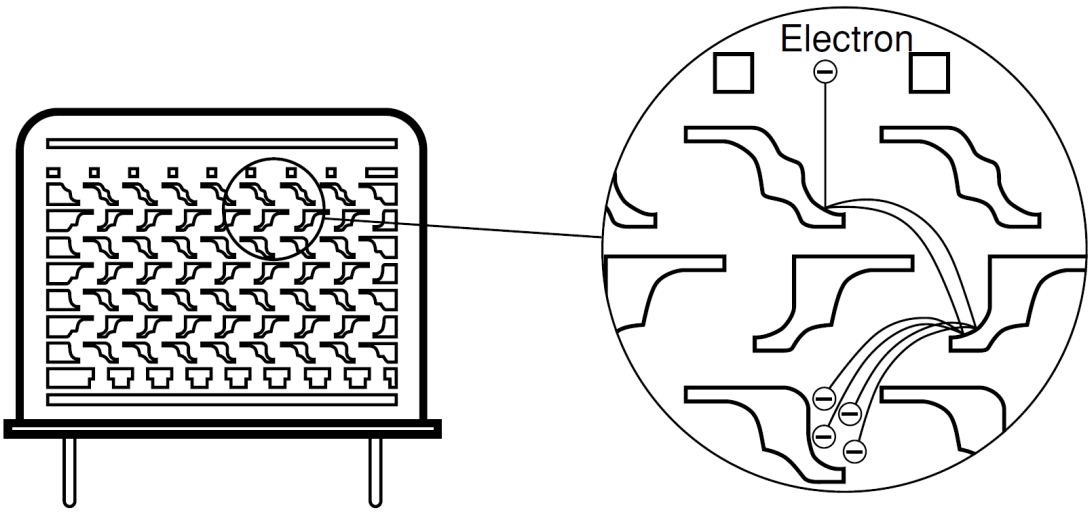


**Figure 2.10** Metal Channel Type Dynode

**8. Electron Bombardment Type Dynode**

In this configuration, photoelectrons accelerate by applying a high voltage and collide with a semiconductor material. This collision results in the transfer of energy from the photoelectrons to the semiconductor, leading to the generation of a gain. This straightforward configuration exhibits minimal noise, remarkable uniformity, and elevated linearity. Figure 2.11 illustrates the cross-sectional views of electron bombardment type dynode.

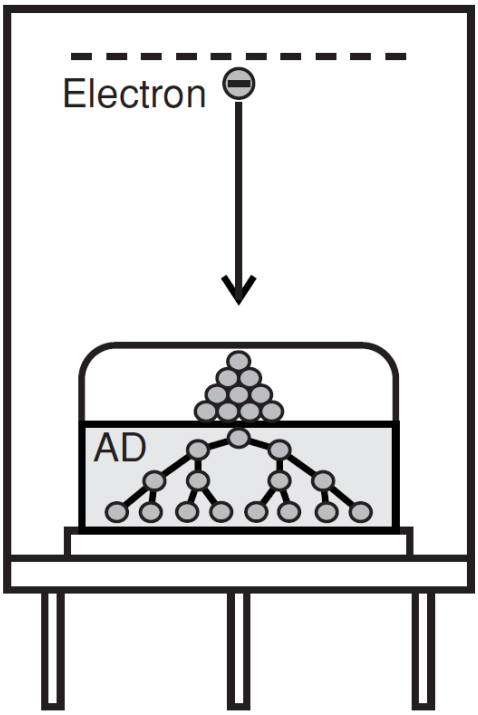


**Figure 2.11** Electron Bombardment Type Dynode

## 2.6.9 R7761 Photomultiplier Tube

Hamamatsu single anode R7761 PMT, which was previously used for collecting data in the CDF experiment at Fermi National Accelerator Laboratory (Fermilab) [3,62,63]. As shown in the Figure 2.12 and Figure 2.13 R7761 PMT has 19 dynode stages serving as secondary emissive electrodes in a fine mesh structure, and it has a length of 50 mm and a diameter of 39 mm with an operational window diameter of 27 mm [43].

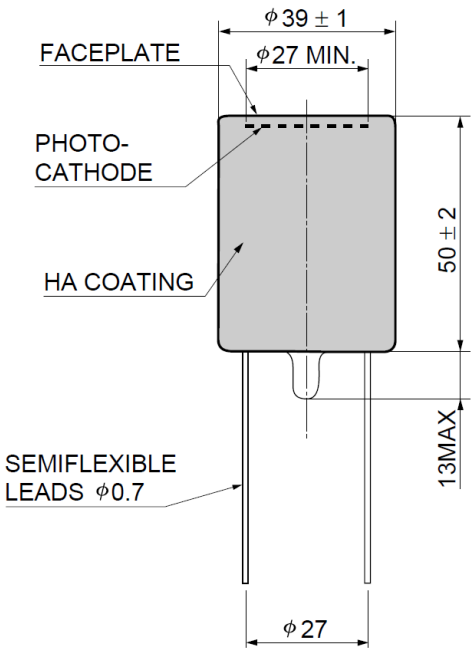


**Figure 2.12** Dimension of Hamamatsu R7761 Photomultiplier Tube.

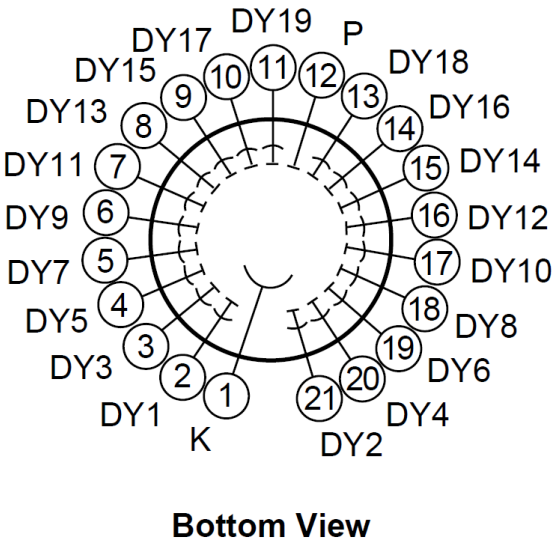


**Figure 2.13** Pin names and positions for Hamamatsu R7761 Photomultiplier Tube.

### 2.6.10 Modes of Operation of Radiation

There are three general modes of operation of radiation detectors: mean square voltage mode, current mode, and pulse mode. All detectors must be operated in pulse mode when measuring the energy of radiation of individual quanta. Pulse mode is an easy mode; thus, this mode is the most applied. In this mode, each quantum of radiation that interacts with the detector is recorded. These kinds of applications are classified as radiation spectroscopy. Radiation detectors produce data as pulse-type radiation and there are some methods to use to extract information from this data. Already the aim is to extract exact timing information about each data [23]. This process covers nuclear electronics[1,64–67].

## 2.7 The Effects of High Voltage on PCB

It is classified as low voltage between 0 and 50 volts and high voltage between 1000 and 500000 volts. Since we use a voltage between 1700V and 2400V in this study, we are working in the high voltage section. The effects of low and high voltage on the circuit are very different. Therefore, we realized our design by considering the adverse effects of high voltage during the circuit design process. Safety is a priority in our design process, considering elements such as the number of layers, the type of board, and the shape of the transmission paths and pads.

Today, the production of PCB boards that can withstand up to 40000 voltage values has only been possible with the fulfillment of certain conditions. There are elements to be considered in the design of these PCBs, which can be created up to approximately 40 layers. In our study, we preferred the FR4 board with a thickness of 1.6mm, which can provide insulation up to approximately 40kV. As the number of layers increases in a PCB with a certain thickness, the layers will approach each other, and the insulation feature will decrease, so we realized our design in the two layers (top and bottom), which is the lowest possible for our design. Since arcing between pins may occur at high voltage, we used round designs instead of angular designs in both paths and pads. For the same reason, we tried to make the soldering on the circuit in a round shape without leaving sharp edges.

### 2.7.1 Width of the Current Path on the PCB

One of the elements we pay attention to in circuit design is the width of the conduction trace. In order to determine the value of this width, the current passing through that path must be found. Since different modes have different resistance values, separate calculations must be made for each mode. In Mode 1, 1kΩ and 660kΩ resistors are added to the chain of 19 330kΩ resistors, while only 1kΩ resistors are added in Mode 2 and 3. These modes represent different operating conditions of the circuit, and the calculations help us ensure that the PCB can handle the current under these conditions. In this calculation, where we try to find the current value, we will do it according to 2000V, the optimum operating voltage of our PMTs. If the current calculation is made for Mode 1,

$$I_{\text{Mode 1}} = \frac{2000\text{V}}{1\text{k}\Omega + 660\text{k}\Omega + 19 \times 330\text{k}\Omega} = 0{,}000288\text{A} = 288\mu\text{A}$$

value is found. If calculated in the same way for Mode 2 and 3,

$$I_{\text{Mode 2 and 3}} = \frac{2000\text{V}}{1\text{k}\Omega + 19 \times 330\text{k}\Omega} = 0{,}000319\text{A} = 319\mu\text{A}$$

value is found.

Equation (2.13) gives the expression for the amount of current passing through a PCB depending on the width ($W$) of the current paths.

$$W = \frac{\left(\frac{I}{k \times T_{Rise}^{b}}\right)^{\frac{1}{c}}}{t \times 1.378} \tag{2.16}$$

For IPC-2221 external layers: k = 0.048, b = 0.44, c = 0.725 where k, b, and c are constants resulting from curve fitting to the IPC-2221 curves. The IPC-2221 standard is a generic printed circuit board qualification and acceptance standard for PCBs/PCBAs. These constants are derived from the specific characteristics of the PCB and the desired current-carrying capacity. In the board design, we made the width of the tracks 1mm. The specifications of our PCB board are FR4, 1 oz/ft$^2$ Thickness, 25°C Ambient Temperature, and 10°C Temperature rise ($T_{Rise}$). When we substitute these values into equation (2.13), it will be seen that the value of the current that can pass through 1mm wide tracks is 2.4A. This value meets the 288µA and 319µA values we need.

## 2.8 The Thermal Voltage (Boltzmann Constant)

In semiconductors, the Shockley diode equation, which governs the relationship between electric current flow and electrostatic potential across a p-n junction, is heavily influenced by a characteristic voltage. This voltage denoted by $V_T$, is thermal voltage, a crucial parameter in semiconductor physics. The thermal voltage is directly proportional to the absolute temperature T, as expressed in the equation below:

$$V_T = \frac{kT}{q}. \tag{2.17}$$

Here, $q$ is the magnitude of the electric charge on the electron, and its value is $1.602176634\times10^{-19}$ C, and $k$ is the Boltzmann constant defined to be precisely $1.380649\times10^{-23}$ J/K.

At room temperature 300 K (27 °C; 80 °F), substituting these values into equation 2.17 , we can calculate the thermal voltage, $V_T$, to be approximately 25.85 mV.

$$V_T = \frac{kT}{q} = \frac{1.380649 \times 10^{-23}[\mathrm{J/K}] \times 300\ \mathrm{K}}{1.6 \times 10^{-19}\mathrm{C}} = 25.85\ \mathrm{mV}. \tag{2.18}$$

We adopted this value as the reference for the –30mV threshold applied in our measurements throughout this study to veto the background signal in the room temperature.

## 2.9 Conclusion

In this chapter, after giving general information about radiation, various types of radiation are explained. The types of detectors used in particle detection are mentioned. After an overview of other types of detectors, we talk about photomultiplier tube detectors, which are the focus of our research. We explain the components and working principle of photomultiplier tubes. We describe the parameters that shape the spectral response characteristics of a photocathode. Finally, the technical specifications of the R7761 PMT we used in our study were discussed.

# Chapter 3

# Methods and Materials

## 3.1 Introduction

In this chapter, we describe in detail the preparation phase of the testing process, which is a crucial step in our thesis. This stage includes a series of procedures planned and implemented to ensure the accuracy and reliability of our results. This chapter explains the Secondary Emission Ionization (SE) Calorimetry technique. It also describes the design and fabrication of the electronic board for the operation of the R7761 photomultiplier detector. The simulation explains the differences between the design of manual and remote-controlled electronic boards. Finally, the operating modes are shown through screenshots of the computer interface program that controls the remote-control board via computer. In addition, we analyze the voltage-dependent signal size, dark current and gain measurements of the PMT we use.

## 3.2 Secondary Emission Ionization (SE) Calorimetry

Calorimetry in nuclear systems involves the utilization of methods to accurately measure the energy of particles by absorbing them in a material medium. Calorimetry plays a vital role in contemporary high-energy, nuclear reactors, and nuclear physics experiments. Recent advances in nuclear reactors and accelerators demand higher levels of performance from nuclear instrumentation systems in radiation hardness, higher luminescence, resolution, and speed. For this goal, the secondary emission ionization calorimetry has recently been introduced.

The PMT materials are known to be radiation-hard, but there are currently no commercially available SE modules specifically designed for this purpose (and not common) to use as secondary emission ionization calorimetry in high radiation

environments. To illustrate the SE process in the dynode chain and the potential application of such detectors in calorimetry, the biasing modes of PMTs will be modified. These modifications are related to the arrangement of the voltage dividers of the baseboard circuits. The photomultiplier tube with modified bases (known as using SE mode of operation) can be used as a secondary emission detector module in a secondary emission calorimeter prototype. The study will focus on the technical design of various operating modes and the characterization measurements of both secondary emission modes and the regular PMT mode. For this aim, Hamamatsu single anode R7761 PMTs will be characterized for use in a secondary emission ionization calorimetry study.

Secondary Emission Ionization calorimetry is a new technique used to measure electromagnetic shower particles in environments where radiation is extremely high. This technique is based on the ability to use the first dynode as a photocathode in order to continue the measurement of radiation in the event that the photocathode exposed to high radiation is disabled by burning.

## 3.3 Manual-Controlled Electronic Board Design for R7761 PMTs

### 3.3.1 Manual-Controlled Schematics Design for R7761 PMTs

The dynamic behavior of the photomultiplier tube will be modeled in Spice environments to simulate the electron multiplication between inter-dynode stages [68]. Proteus software has been used to design the schematic and PCB layout [69]. A general PMT Spice model based on a Hamamatsu PMT (e.g., R7761) system parameters will be developed. The goal of the model is to analyze different divider circuits (namely, uniform and tapered). The simulation results will be compared with the experimental results provided in the literature.

Operation of the R7761 photomultiplier tube requires a voltage source of at least -1700 V and a voltage divider circuit to allocate this voltage to the PMT's dynodes appropriately. In order to get high efficiency from the PMT, providing the appropriate voltage to the dynodes is mandatory. Since it is not economical or feasible to supply each dynode with a separate voltage source, a voltage divider circuit is necessary. Therefore,

a voltage divider circuit is usually used to supply the appropriate voltage to each dynode of the PMT, and a high-voltage power supply is used to feed this circuit. A stable voltage from the high-voltage source is crucial for the proper operation of the PMT. Since photomultiplier tubes have a very high sensitivity, they must be protected from light sources other than the radiation to be measured. Otherwise, high noise is generated, and signal acquisition becomes impossible. Using a sheath to protect it from magnetic fields prevents noise in the PMT. Due to the high number of PMT dynodes, such as R7761, capacitors are added to these dynodes to prevent the voltage drop between the dynodes near the anode. We added a 22nF decoupling capacitor to the last five dynodes of the voltage divider board we designed. Figure 3.1 shows the schematic diagram of the secondary emission voltage divider for R7761. The circuit schematic shows the baseboards that power and read data from a single PMT in the SE module.

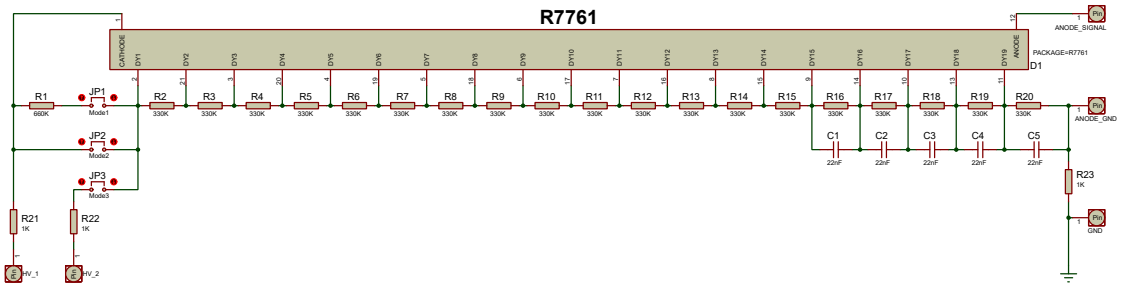


**Figure 3.1** Schematic diagram of the secondary emission voltage divider for R7761 PMTs.

### 3.3.1.1 Circuit Voltage Divider for 3 Modes

There are three different modes of operation for the baseboards of R7761 single-anode PMTs. Mode 1 and Mode 2, both with high voltage input on HV1 and Mode 3 with high voltage input on HV2. For data collection, ammeters and oscilloscopes will be used.

**Mode 1**: Normal divider or traditional (PM) mode: JP1 switch is closed. As shown in Figure 3.2, the voltage divider chain is unchanged and the potential difference gotten across the dynodes is equal, except for the 2 times potential across the Cathode-Dy1 gap. This is a reference design by Hamamatsu [4].

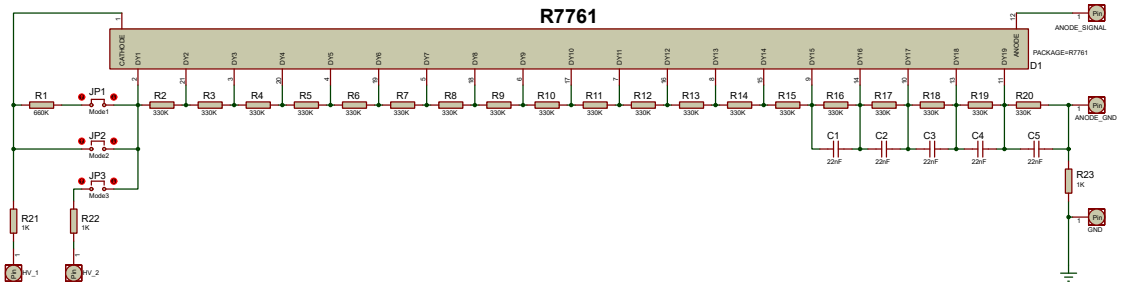


**Figure 3.2** Schematic diagram of the secondary emission voltage divider for R7761 PMTs for Mode 1

**Mode 2**: Cathode-first Dynode shorted: In this mode JP2 switch is closed. As shown in Figure 3.3, the bridging of the R1 resistor is enabled, and the potential across the Cathode-Dy1 gap is 0 volt.

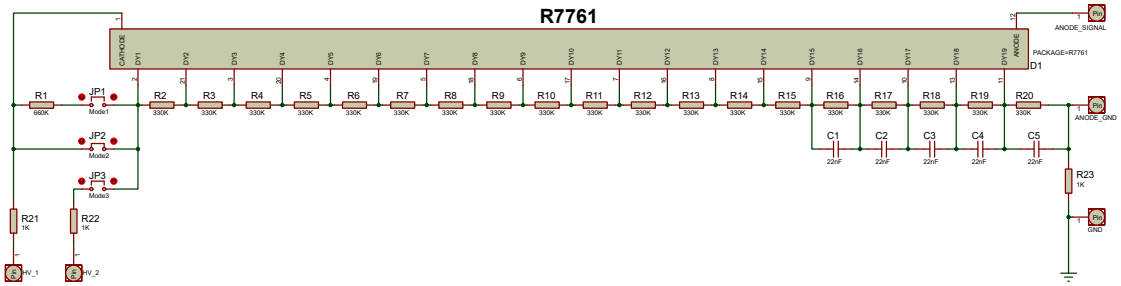


**Figure 3.3** Schematic diagram of the secondary emission voltage divider for R7761 PMTs for Mode 2

**Mode 3**: Cathode separated/independent/float mode: By closing the JP3 switch, the cathode is isolated from the rest of the divider chain. As shown in Figure 3.4, a second voltage input to the baseboard allows for the voltage present on Dy1. In this mode, if there is no second high voltage source, the photocathode may still charge.

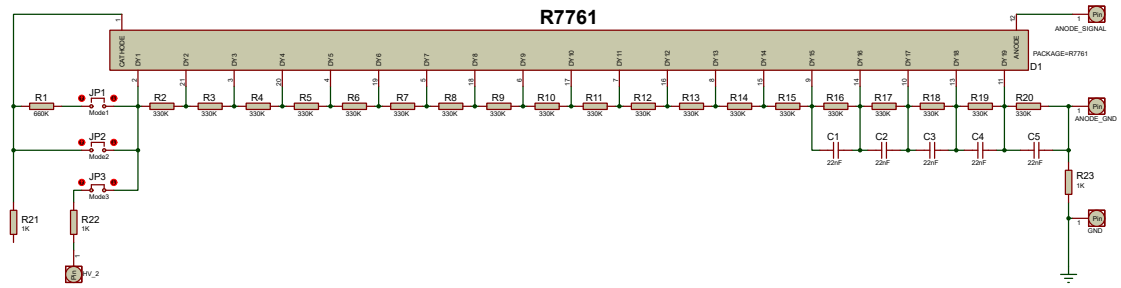


**Figure 3.4** Schematic diagram of the secondary emission voltage divider for R7761 PMTs for Mode 3

### 3.3.2 PCB Design, Manufacturing and Assembly of Manual-Controlled Board

A PCB, or Printed Circuit Board, is a flat board made up of copper sheets that have been etched and bonded onto a non-conductive base. It has lines, paths, tracks, and pads that link different spots on the board. These lines allow the routing of power and communications between actual devices.

A PCB layout of the manually controlled R7761 photomultiplier tube is shown in Figure 3.5. Figure 3.6 shows a three-dimensional representation of this schematic. Figure 3.7 shows the printed circuit board with all the soldering and assembly processes done. Two high voltage inputs are provided with SHV connectors while BNC connectors were used for the signal. As can be seen in the photo, the photomultiplier detector was wrapped with a light-impermeable foil and then taped with insulating tape to protect it from light.

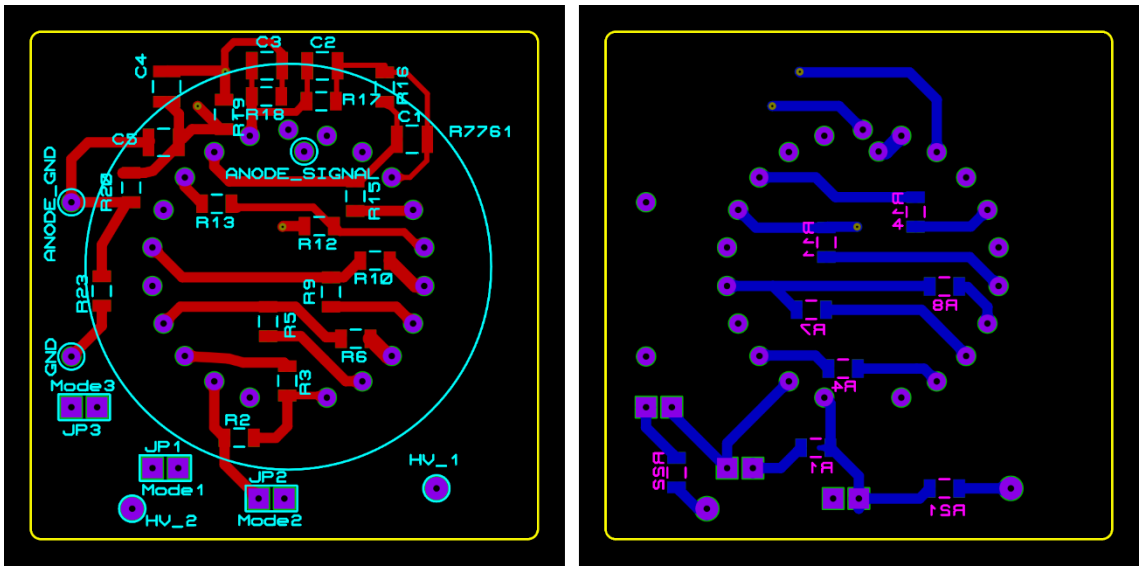


**Figure 3.5** PCB layout view of top side (left) and bottom side (right) for manual controlled R7761 type Photomultiplier tube.

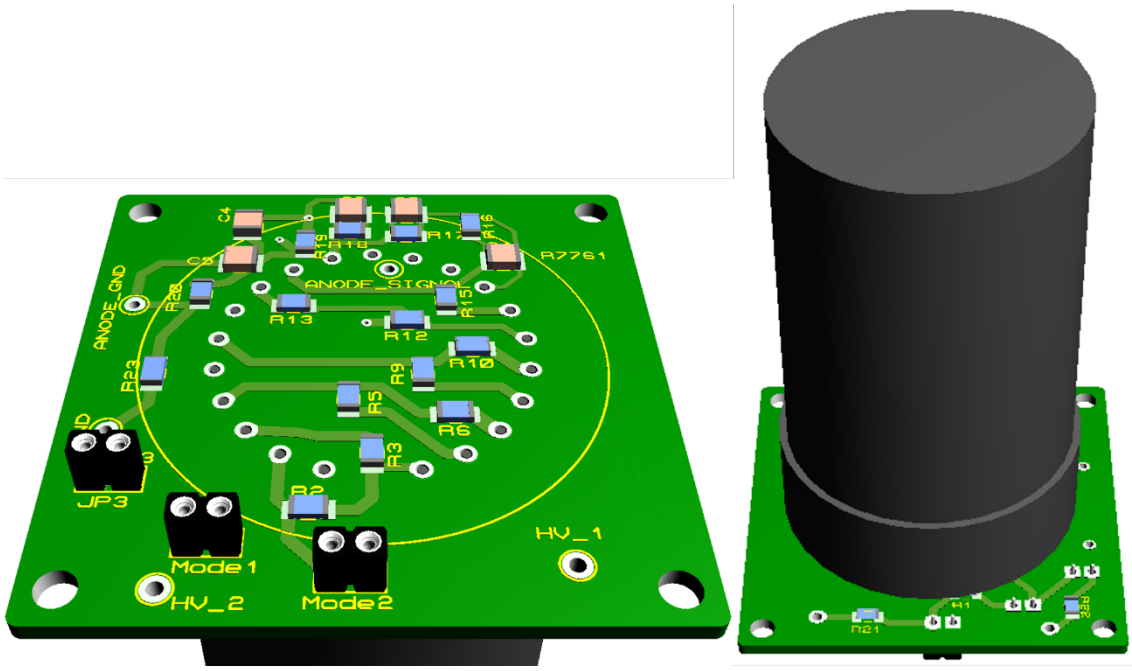


**Figure 3.6** 3D view of top side (left) and bottom side (right) for manual controlled R7761 type Photomultiplier tube.

**Figure 3.7** Image of the electronic board with all soldering and assembly processes completed.

## 3.4 Remote-Controlled Electronic Board Design for R7761 PMTs

### 3.4.1 Remote-Controlled Schematics Design for R7761 PMTs

This section will explain in detail how the high voltage supplied to the voltage divider circuit that drives the PMT is done for the three modes. Figure 3.8 shows the schematic diagram of the SE voltage divider circuit for remote-controlled R7761 photomultiplier tube. This circuit schematic shows the baseboards that power and read data from a single photomultiplier tube.

Understanding the high-voltage application points in the voltage divider circuit that drives the PMT is crucial. The only change for the different modes is the points at which the high voltage is applied to the circuit. So, three different high-voltage application points exist for the three modes. In the first mode, the high voltage is applied to the photocathode through a 1kohm resistor and to the first dynode through a 660kohm resistor. In the second mode, the high voltage is applied directly to the photocathode and the first dynode through a 1kohm resistor. Finally, in the third mode, the photocathode was utterly disabled, and the high voltage was applied directly to the first dynode through a 1kohm resistor. In all three modes, the applied voltage value gradually decreases after the first dynode point in the voltage divider circuit since the resistances are equal until it is divided equally and reach 0V at the anode.

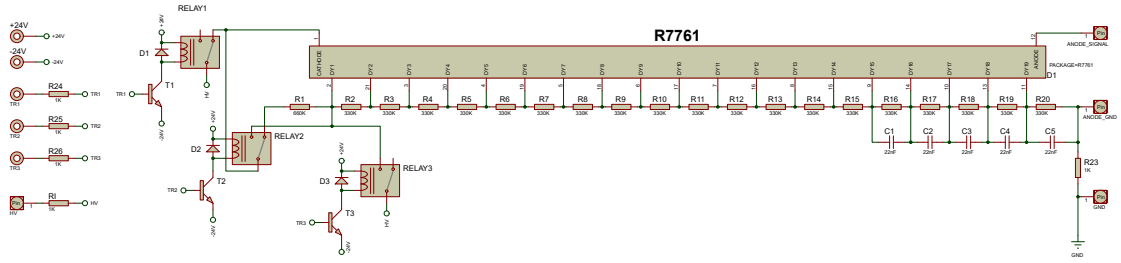


**Figure 3.8** Schematic diagram of the SE voltage divider circuit for remote-controlled R7761 photomultiplier tube.

The selection of relays for the high-voltage control circuit was not arbitrary. We meticulously chose them to ensure the circuit's performance. Relays were chosen for their affordability, accessibility, ease of control, and reliability as electronic circuit elements. Since the DC coil that switches these relays on and off operates with a nominal voltage

of 24V, these relays cannot be directly controlled with the Arduino, which can output 5V. One solution to overcome this problem is to use suitable transistors between the Arduino and the relays. The schematic connections of the relays and transistors are given in Figure 3.9 . The right transistor was chosen based on the nominal voltage and coil resistance of the relay we are using. This means that we need to supply the electronic circuit board externally with 24VDC to operate the relays. The 24V entering the DC coil of the relay will be connected to the collector of the transistor at the other end of the coil and reach the ground via the emitter. Therefore, the Collector-Emitter Voltage of the transistor must be more than 24V and the Collector Current (Continuous) must be more than 22.5mA. For the 2N3904 npn transistor we use, the Collector-Emitter Voltage value is 40V, and the Collector Current (Continuous) value is 200mA, so it easily meets the desired values.

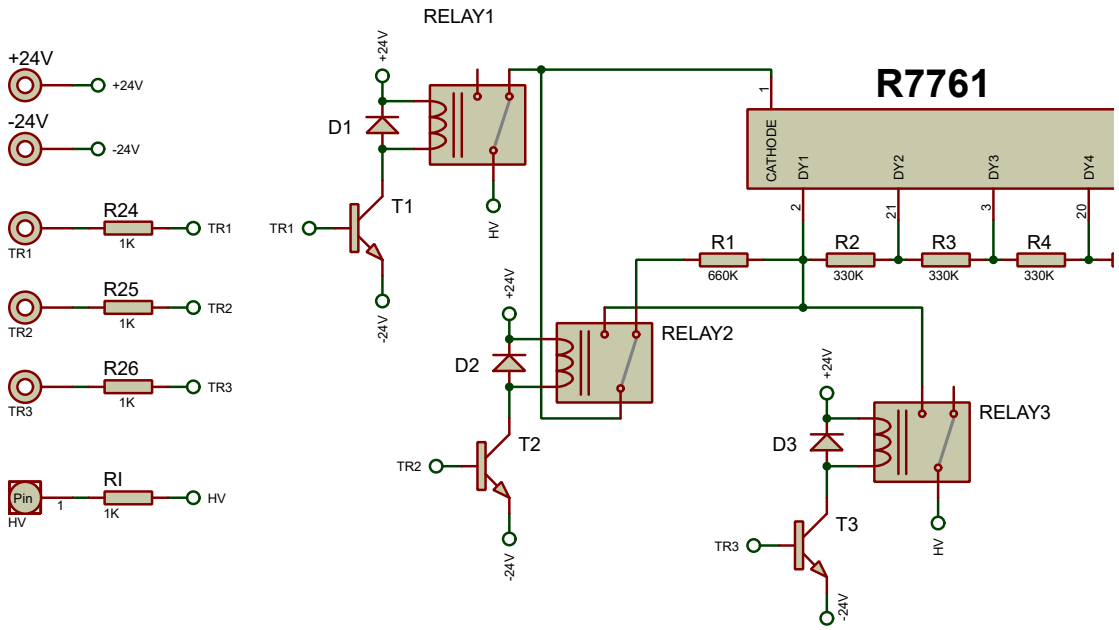


**Figure 3.9** The schematic connections of the relays and transistors in detail.

As mentioned above, since it is impossible to drive a relay with a 24V operating voltage directly with Arduino, it is necessary to put a suitable transistor in between. Depending on the value of the current in the Base leg of the transistor, the amount of current in the Collector leg changes. One factor that determines the value of the current in the Base leg is the value of the resistor connected to the Base leg. In our simulation studies, we can obtain the desired values when we connect a 1k ohm resistor to the Base leg. Figure 3.10a is the transistor-relay schematic, and the simulation result of this schematic is shown in Figure 3.10b. As shown in Figure 3.10b, the current flow in the

coil of the relay connected to the collector leg of the transistor is 0.0227702A ≅ 22.8mA. This value provides the 22.5mA value required for the relay to create a sufficient magnetic field to perform the switch function.

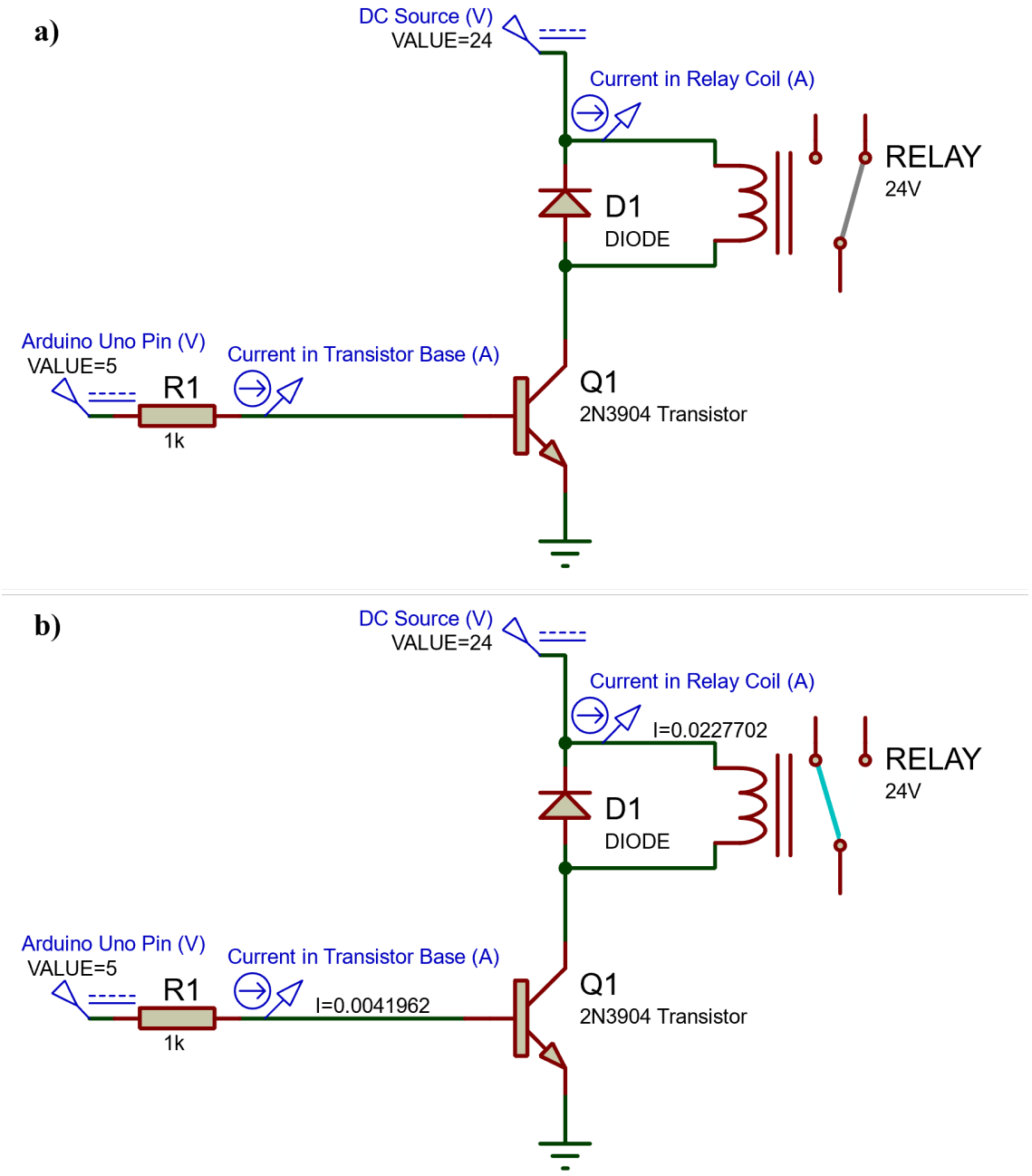


**Figure 3.10** Relay and Transistor simulation result **a)** when switch OFF **b)** when switch ON.

To compare the simulation result with the analytical solution, let us analyze the circuit using the schematic given in Figure 3.11. From $V_{CC}$ through C and E to GND, the equation becomes:

$$V_{CC} - I_C \times R_C = 0.$$

If we substitute their values:

$$24\text{V} - I_C \times 1\text{k}\Omega = 0$$

is found. If we subtract $I_C$ from here, $I_C = 24\text{mA}$ is found. This value is close to the 22.8mA value obtained as a result of simulation.

For the current starting at 5V and ending at GND via B and E, the equation becomes:

$$5\text{V} - I_B \times R_B - V_{BE} = 0.$$

If the values are substituted,

$$5\text{V} - I_B \times 1\text{k}\Omega - 0.7\text{V} = 0$$

is found. If we subtract $I_B$ from this equation, then $I_B = 4.3\text{mA}$ is found. It is seen that this value is close to the 4.2mA value obtained as a result of simulation.

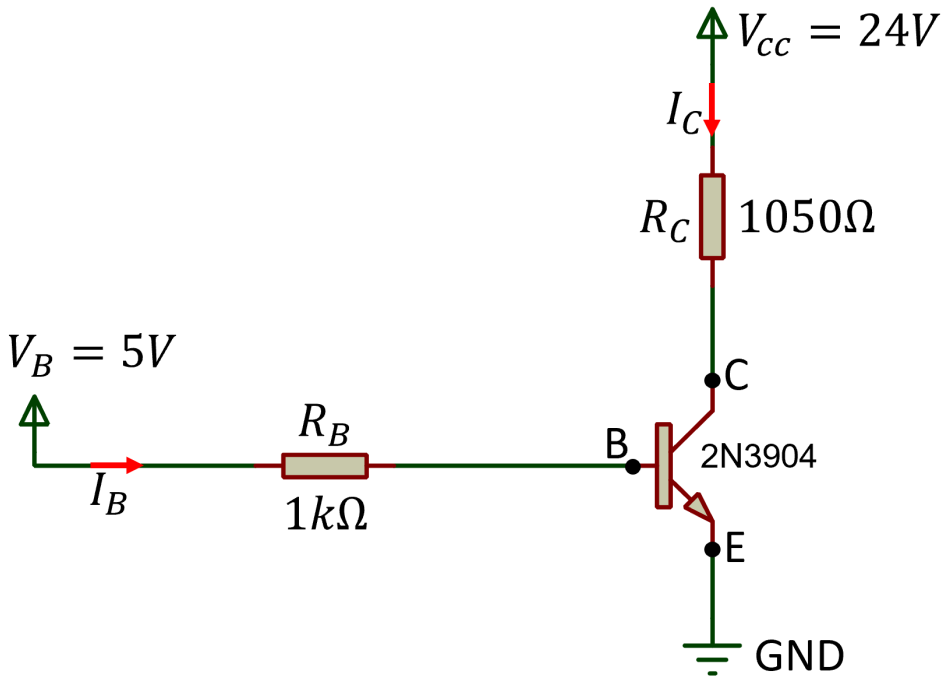


**Figure 3.11** Equivalent circuits drawn for solving the current values $I_C$ and $I_B$ in the relay and transistor circuit diagram by analytical method.

A potential problem in this design was also addressed: When the voltage applied to the relay is switched off, the field induced on the DC winding may cause reverse currents and cause the transistors to fail after a while. This problem was solved by connecting a diode in parallel to the two legs of the DC winding.

The on/off combinations of transistors by mode, as presented in Table 3.1, were not randomly chosen. This strategic design can be created in different ways. The electronic board design we made was created according to the combination given in Tablo 3.1. According to this design, all transistors must be in the LOW (deactivated - not energized) position for the first mode to be active. This choice was a preferential choice. Because the first mode is the basic mode, it eliminates the need to actively control the electronic board to operate in this mode. The second and third modes require active control of the circuit. For the second mode to be active, the first and third transistors must be LOW, and the second transistor must be HIGH (activated-energized). Finally, for the third mode to be active, the first and third transistors must be high. In this mode, whether the second transistor is LOW or HIGH does not change the circuit.

**Table 3.1: Transistors combination for modes.**

| | **MODE 1** | **MODE 2** | **MODE 3** |
|---|---|---|---|
| **TRANSISTOR 1** | LOW | LOW | HIGH |
| **TRANSISTOR 2** | LOW | HIGH | LOW/HIGH |
| **TRANSISTOR 3** | LOW | LOW | HIGH |

### 3.4.2 PCB design, Manufacturing and Assembly of Remote-Controlled Board

A PCB layout of the remote controlled R7761 photomultiplier tube is shown in Figure 3.13 and Figure 3.14. Figure 3.15 represents a three-dimensional representation of this schematic. Figure 3.12 shows the printed circuit board with all the soldering and assembly processes done. Two high voltage inputs are provided with SHV connectors while BNC connectors were used for the signal. As can be seen in the photo, the photomultiplier detector was wrapped with a light-impermeable foil and then taped with insulating tape to protect it from light.

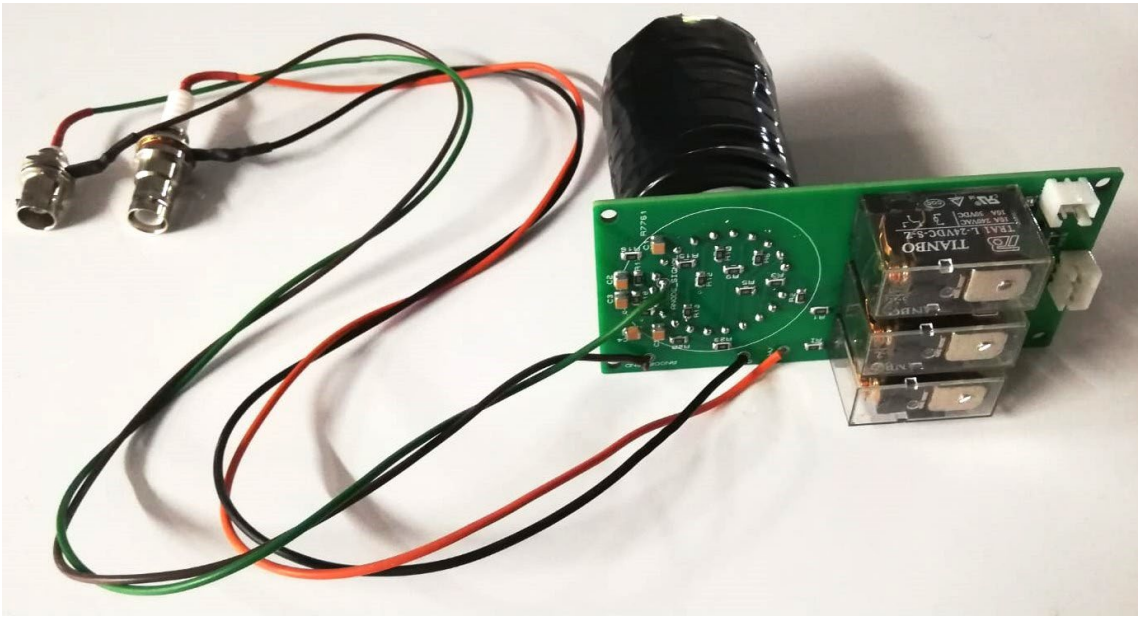

**Figure 3.12** Image of the remote-controlled electronic board with all soldering and assembly processes completed.

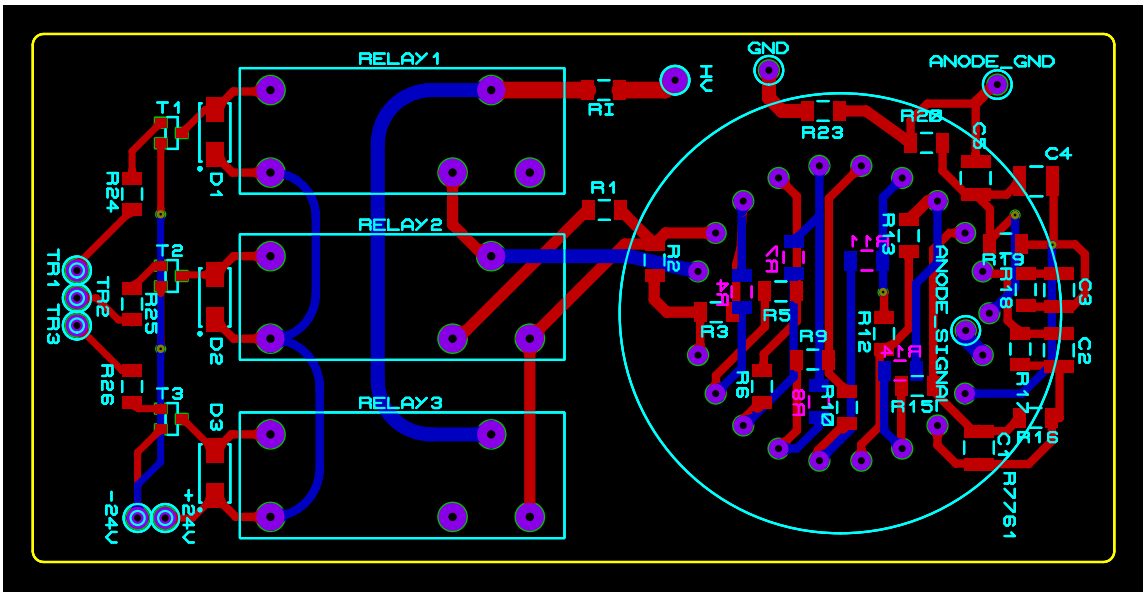


**Figure 3.13** Top and Bottom side PCB layout of the remote controlled R7761 photomultiplier tube.

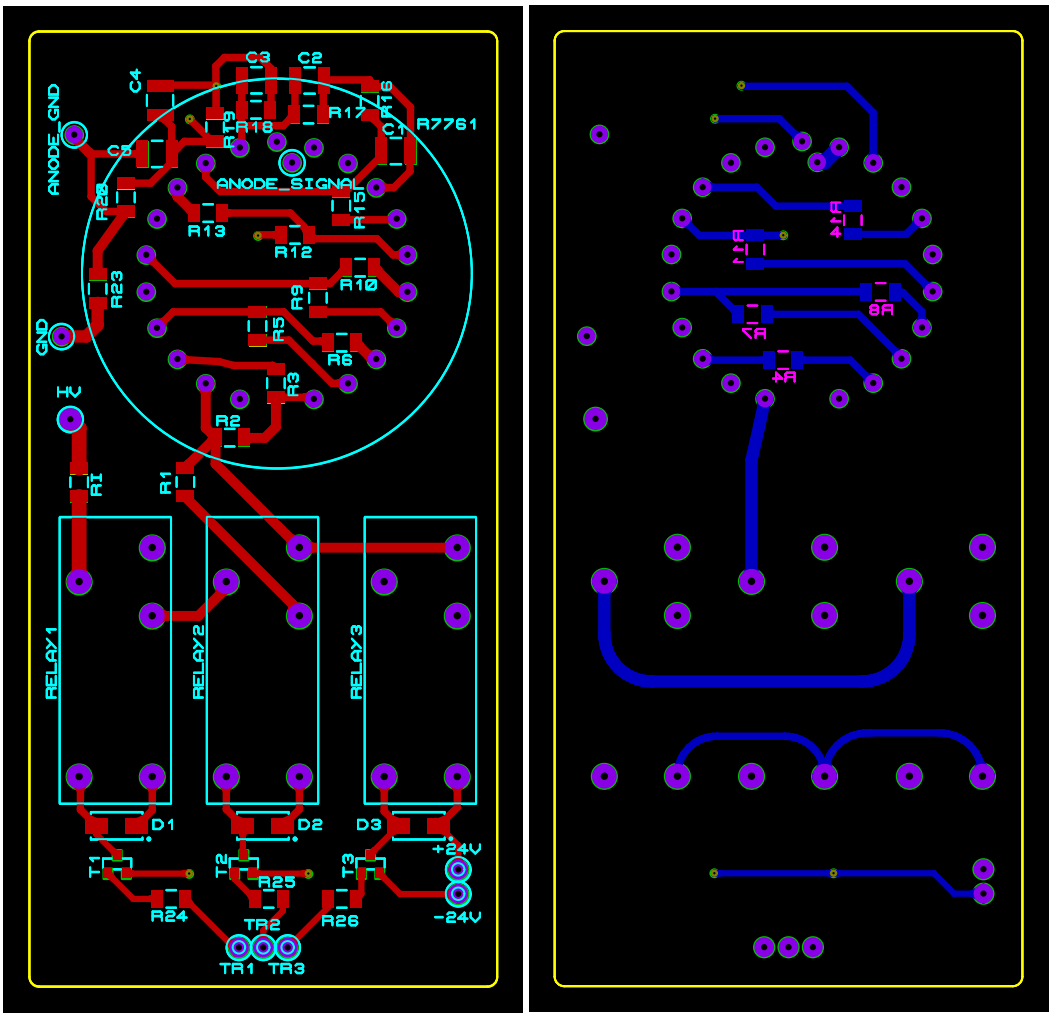


**Figure 3.14** Top (left) and Bottom (right) side PCB layout of the remote controlled R7761 photomultiplier tube.

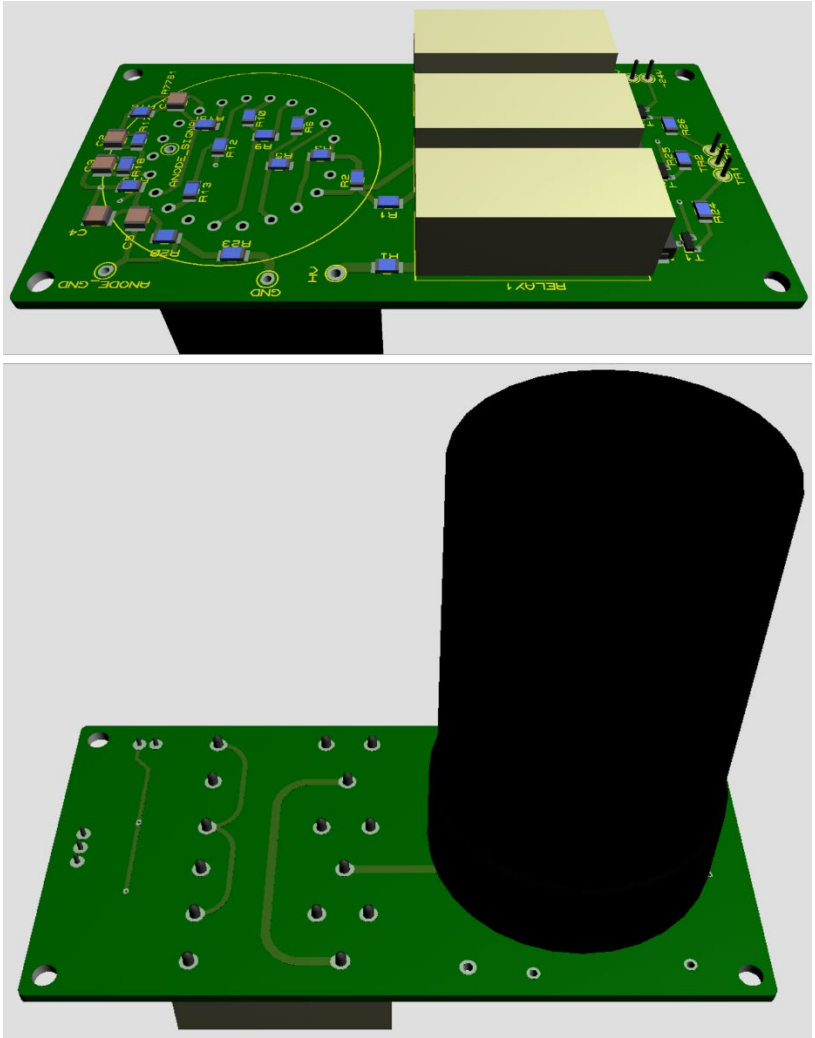

**Figure 3.15** 3D view of the top and bottom, respectively, for the remotely controlled R7761 type Photomultiplier tube.

The test process with the remotely controlled card used for radiation measurements is given in Figure 3.16. The board module is ready for testing by soldering circuit elements to the electronic board and covering the photomultiplier tube with a light-proof foil. Two voltage sources are connected to the module: first, a high voltage connected to the cathode of the photomultiplier tube, and second, a 24V voltage source connected to the DC coil of the relays. The relays are controlled by an Arduino Uno computer through a serial connection, with an interface written for this study. The signal from the anode of the photomultiplier is transferred to the oscilloscope via a BNC connector. The data obtained by collecting a sufficient number (40k-140k hits) of signals triggered at -30mV is transferred to the computer environment, and graphs are drawn.

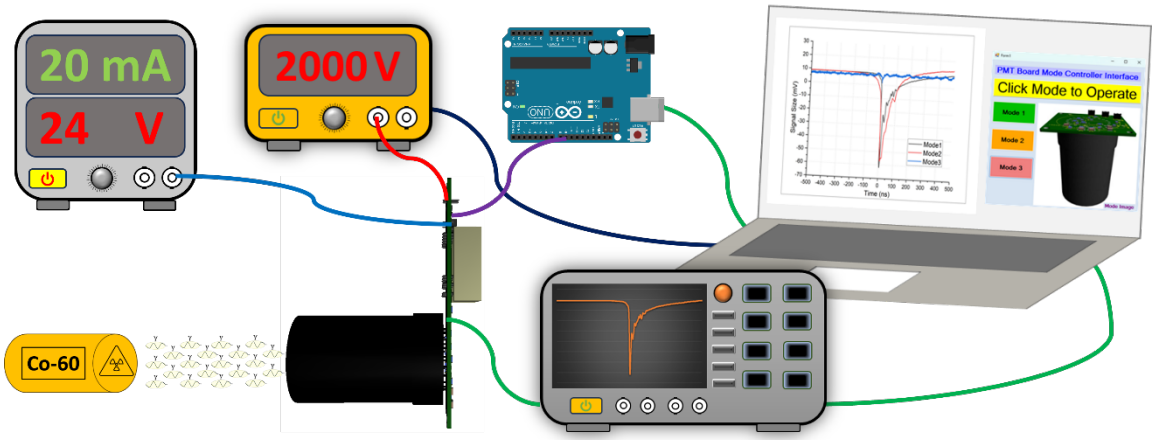


**Figure 3.16** Graphical design of an experimental process for characterization and analysis with the remote-controlled board for Co-60 Gamma ray source.

### 3.4.3 Graphical User Interface for Remote-Controlled Board

The Arduino Uno board was used to turn on and off the relays used to operate different modes on the remote-controlled card [70]. The open-source electronics platform Arduino consists of simple hardware and tools. Arduino boards can interpret input signals and convert them into corresponding output signals. Arduino was coded in C++, and the code used is given in Appendix B. Arduino was connected to the computer via serial communication. The graphical user interface (GUI) program for controlling the modes was written in C#, and the C# code of the program is given in Appendix A. The screenshot of the main page and the modes are given in Figure 3.17.

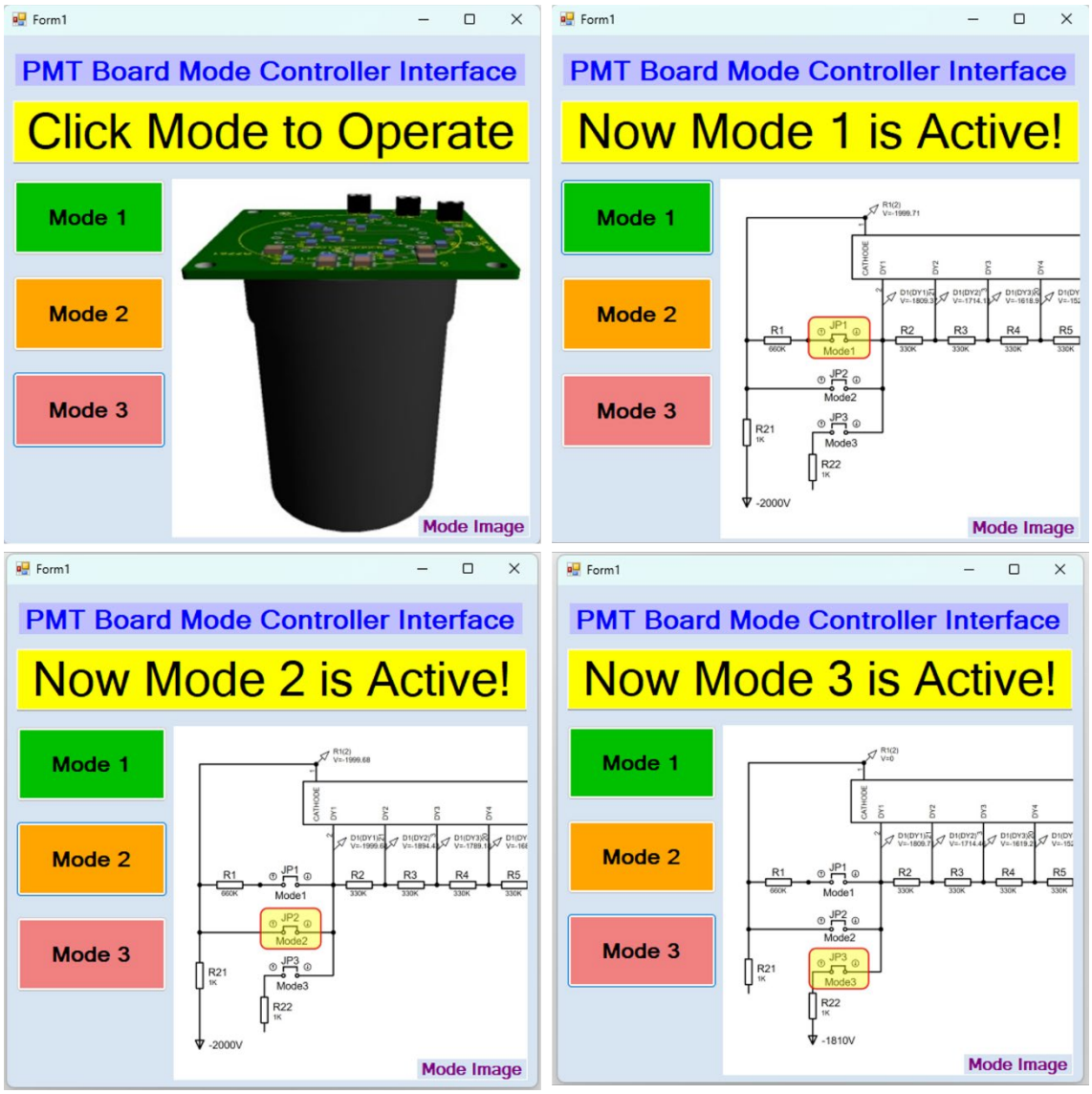


**Figure 3.17** The screenshots of main (left top) and modes windows of the remote-controlled board's GUI.

# 3.5 Signal Characterization of the PMT Mode

The strength of the signal received from the PMT varies according to the value of the applied voltage. Notably, the signal size increases within a specific operating voltage range as the applied voltage increases. Figure 3.18 shows the signal size of the cosmic background for 1800V, 2000V, and 2200V, while Figure 3.19 shows the signal size of Co-60 Gamma radiation. These signal sizes variations are given in Table 3.2. The signal sizes of the PMT mode are increasing with the increasing voltage for both cosmic and gamma radiation, as expected.

**Table 3.2: Approximate signal sizes of cosmic background and Co-60 Gamma radiation for 1800V, 2000V and 2200V voltages applied to the PMT**

| | 1800V | 2000V | 2200V |
|---|---|---|---|
| **Cosmic Background** | 44.0 | 46.0 | 61.7 |
| **Co-60 Gamma** | 35.9 | 49.4 | 78.8 |

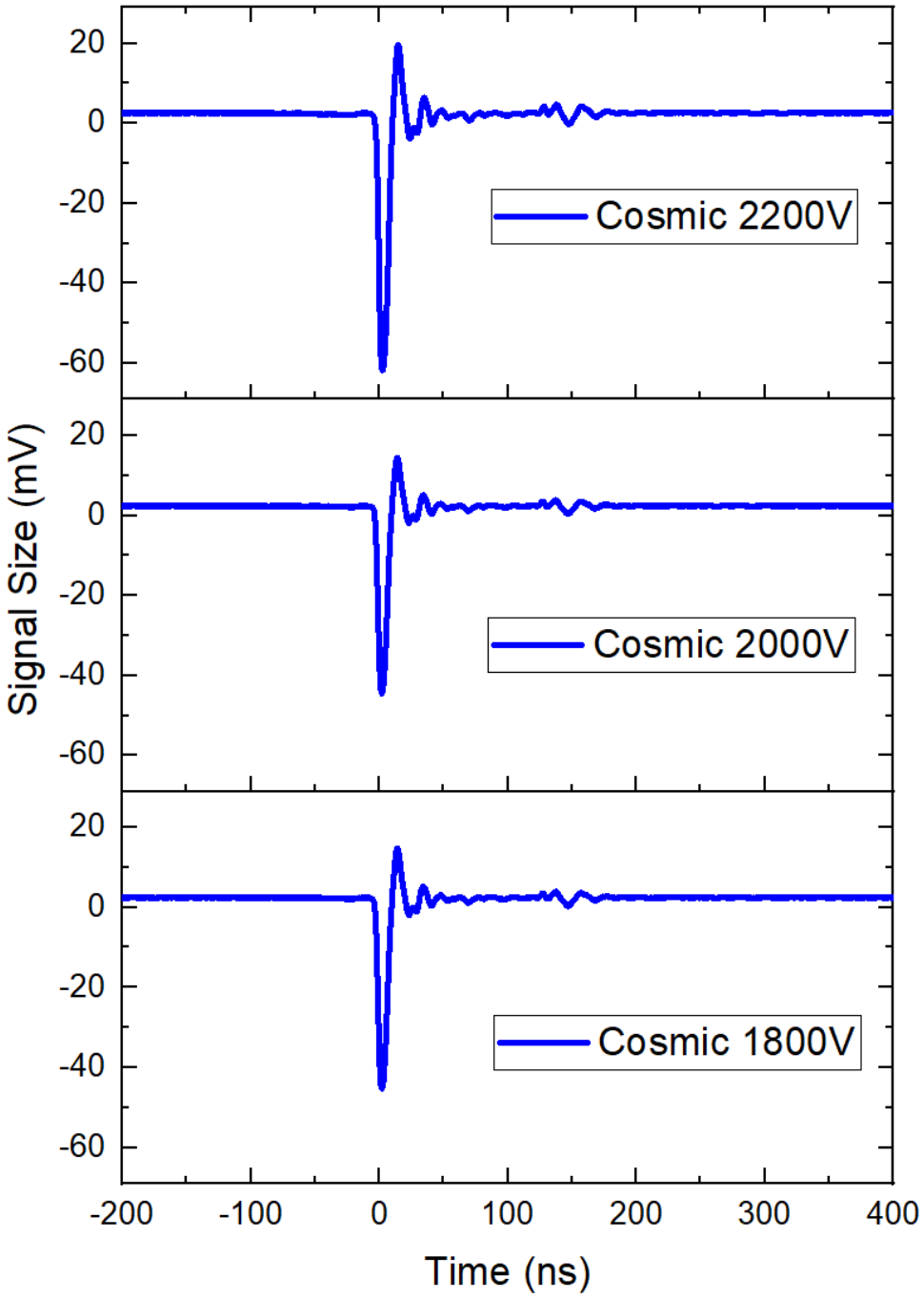


**Figure 3.18:** Pulse shapes of cosmic background radiation for 1800V, 2000V and 2200V voltages applied to the PMT.

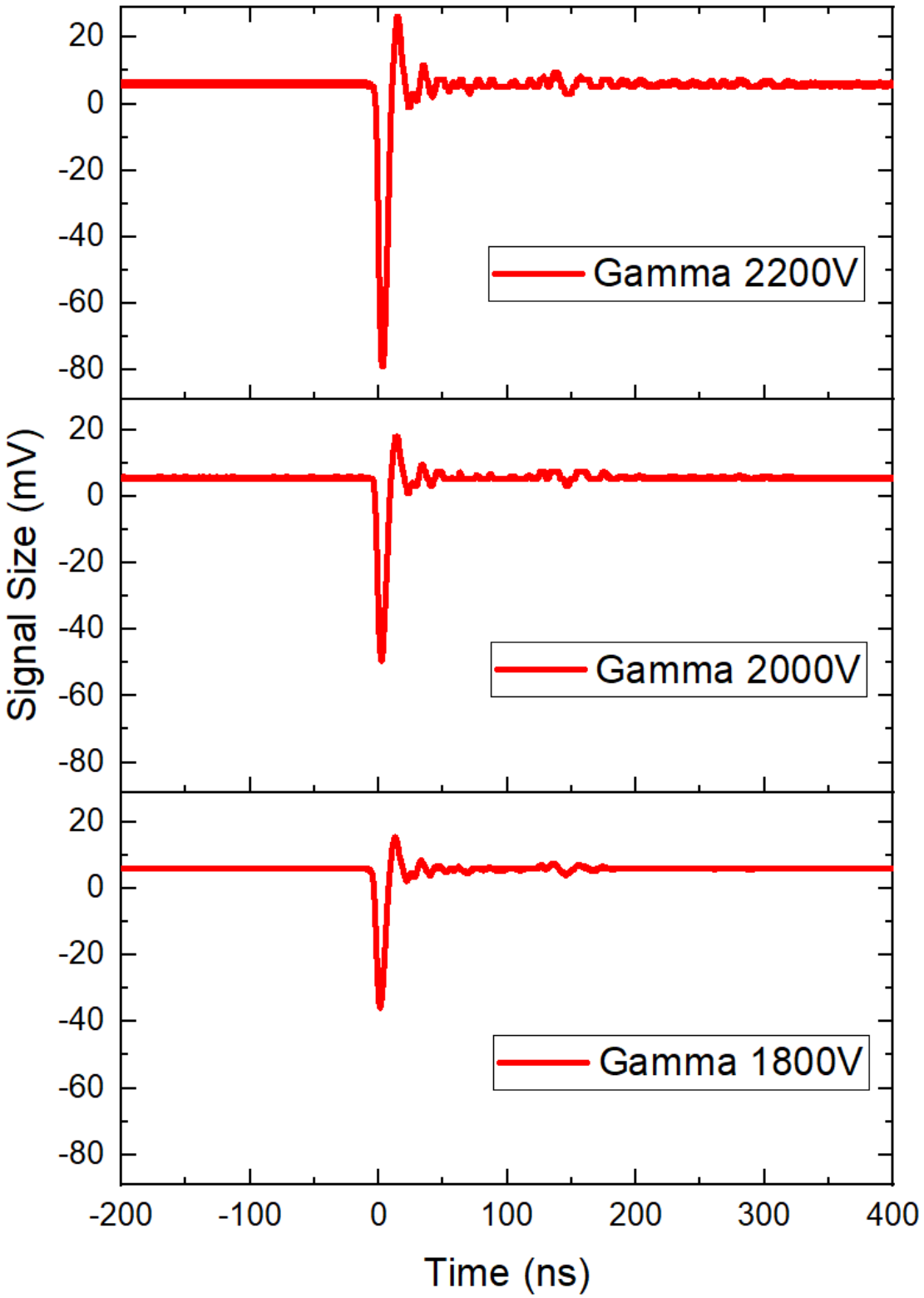


**Figure 3.19:** Pulse shapes of Co-60 Gamma radiation for 1800V, 2000V and 2200V voltages applied to the PMT.

Figure 3.20 shows the linearization graph of the signal size corresponding to 1800V, 2000V, and 2200V values for both cosmic background and Co-60 Gamma radiation.

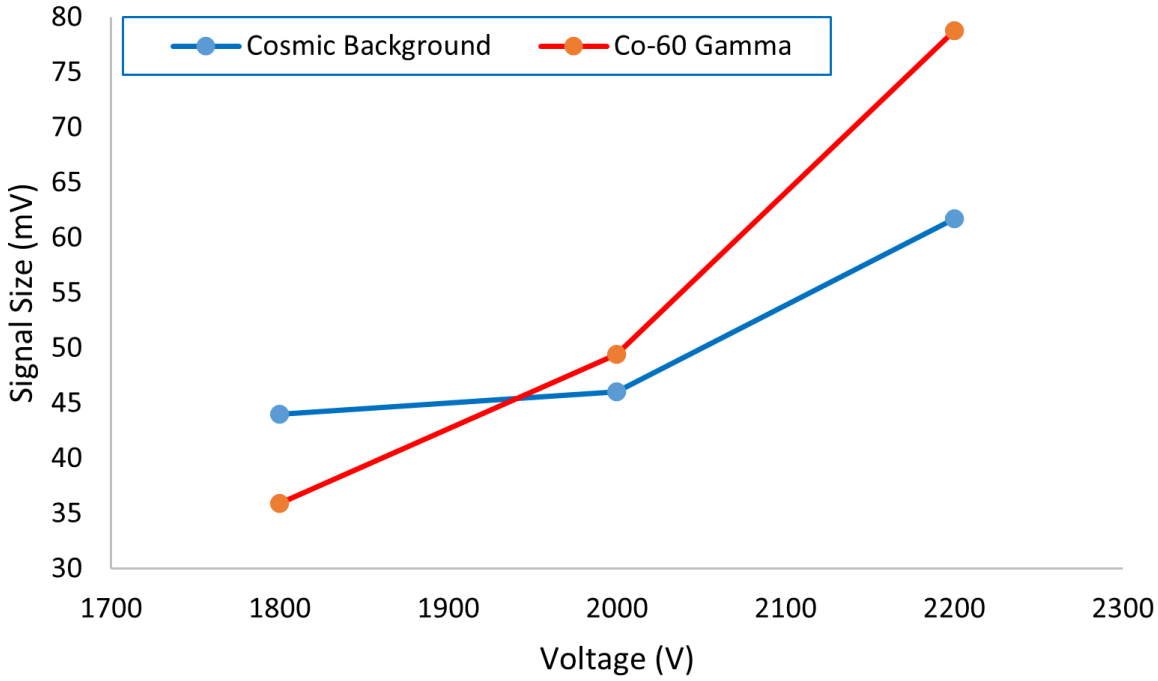


**Figure 3.20:** Linearization graph of R7761 photomultiplier tube

## 3.6 Dark Current Measurement of the Used PMT

Photomultiplier tubes are designed to detect very small amounts of light and current. To achieve this, the PMT must be operated in complete darkness. Even in such a controlled environment, a small amount of current, known as dark current, flows through the PMT. It is crucial to keep this dark current as minimal as possible, as it significantly affects the PMT's performance. The measured dark current values for all different voltages are below 1 nano-amperes (nA), which shows that they all have low dark currents. The dark current graph measured at 1500V, 1800V, 2000V, and 2200V is shown in Figure 3.21 [43]. In most PMTs, the dark current typically remains within a few nA. Despite its very small magnitude, dark current significantly influences the PMTs detection performance due to background noise. The well-known sources of dark current are thermionic emission of electrons, leakage of current, emitted electrons, and ionization of residual gases. Notably, dark current is highly sensitive to the application of high voltage, as shown in Figure 3.21.

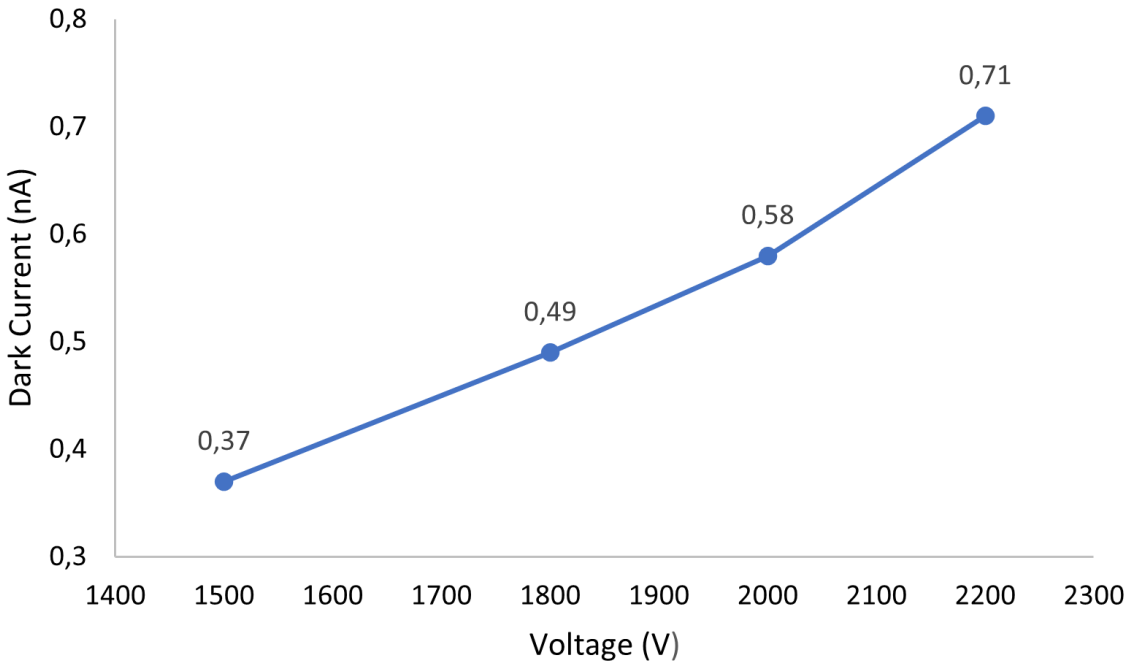


**Figure 3.21:** Dark current graph of the PMT as a fuction of the applied voltages.

# 3.7 Gain Measurement of the Used PMT

Current amplification or gain (μ) in photomultiplier tubes is expressed as in Equation 3.1.

$$\mu = \mathrm{A} \times \mathrm{E}^{k \times n} \tag{3.1}$$

Here, μ is the gain, A is a constant, E is supplied voltage, k is a constant determined by electrode structure and material, and n is the number of dynode stages. As seen in Eq. 3.1, the gain $\mu$ is proportional to the power $k \times n$ of the supply voltage. R7761 photomultiplier tubes with 19 dynodes have a high gain, $10^5$-$10^6$. This high gain significantly amplifies the sensitivity of the tube to the applied high voltage. For one percent of the output stability of a photomultiplier tube, the power supply stability must be kept within 0.1 percent. This means that a PMT's gain is sensitive to changes in the high-voltage power supply, such as drift, ripple, temperature stability, input regulation, and load regulation. The gain graph of the PMT measured at 1500V, 1800V, 2000V, and 2200V is shown in Figure 3.22 [43]. All modes demonstrate stable operation, with mode 1 and Mode2 exhibiting particularly good linear gain in response to applied voltages.

In general, the dark current and gain distributions of the R7761 PMTs used for CDF experiment at Fermilab can be found in the reference [4].

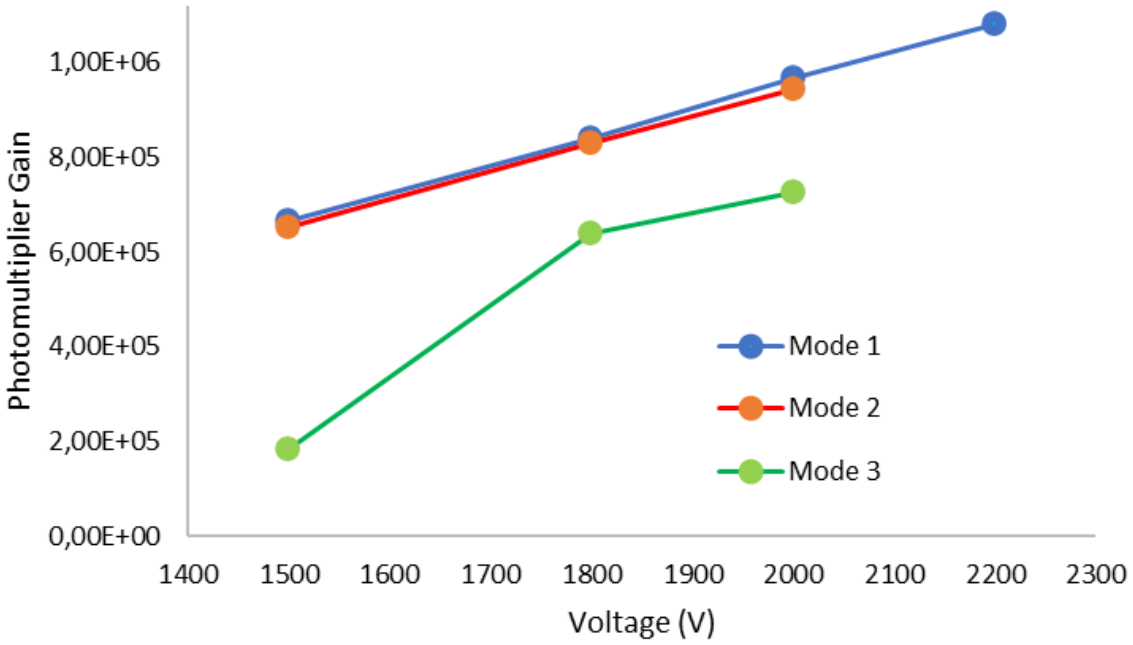


**Figure 3.22:** The gains of all three modes of the PMT as a function of the applied voltages.

## 3.8 Conclusions

In this chapter, we describe the preparation for the radiation testing process, which was essential to ensure the accuracy and reliability of our results. After explaining the Secondary Emission Ionization (SE) calorimetry technique, the design and fabrication of the electronic board for the operation of the R7761 photomultiplier detector was explained. The results obtained by simulation explained the differences between the design of manual and remote-controlled electronic boards. Finally, the operating modes were demonstrated through screenshots of the computer interface program that controls the remote-control board through the computer. The codes for this program are given in Appendixes A and B. In addition, we analyzed the voltage-dependent signal size, dark current and gain measurements of the PMT we used.

# Chapter 4

# Results and Discussion

## 4.1 Introduction

In this chapter, we give the technical background for the experimental process and then explain the testing process and the measurements we have obtained, showing them on graphs. First, we give detailed information about the studies carried out to solve problems in particle detectors operating in high-radiation environments. Then, we discuss one of these solutions, the secondary electron calorimeter. Then, the electronic boards designed and manufactured for the thesis is be tested with the R7761 photomultiplier tube. Finally, the data obtained from our tests with cosmic background radiation and gamma rays are presented and interpreted with graphs.

## 4.2 Particle Detectors in High Radiation Environments

Particle detectors and calorimeters for high radiation environments are sophisticated instruments that measure and analyze subatomic particles [23–25,67,71]. These particle detectors and calorimeters play a significant role in various fields, such as particle physics, high-energy physics, nuclear physics, medical physics, and space applications [6]. Due to the increasing instantaneous luminosity and unprecedented radiation conditions at particle physics and high-energy physics accelerators, the demand for precision, robustness, and reliability in radiation-resistant particle detectors and ionization calorimeters remains paramount.

Scintillation calorimeters operating in high radiation environments are exposed to high radiation levels due to the increased brightness and collision energy, and this radiation may cause damage to the photocathodes of the calorimeters. Experimental groups previosuly reported the effects of radiation damage on the operational

performance of detectors [72–74]. Although there is a real need to develop low-cost, radiation-resistant calorimeters, studies on this subject matter are very limited. To solve this problem, Albayrak et al. and Bilki et al. developed a design based on the principle of Secondary Emission (SE) that will act as a radiation-resistant calorimeter [3,75,76]. Secondary emission ionization calorimetry emerges as a promising frontier, offering enhanced performance in energy resolution and radiation hardness compared to conventional detection techniques [3,5,65,76]. SE calorimeters employ sheet-type or mesh-type transmission dynodes as their dynamic detection medium. In this system, hadronic particles trigger secondary electrons directly from arrays of the dynodes, interacting with the sampling or absorption medium. Eventually, the emitted electrons go through amplification between downstream dynodes and reach the anode [2–5,22,76,77].

Photons incident on a Photomultiplier Tube (PMTs) detaches photoelectrons from the photocathode. Then, the detached photoelectrons are accelerated by an electric field applied between the photocathode and the first dynode, which impacts the first dynode and causes multiple electrons to be knocked out. These secondary electrons, increasingly detached from the first dynode, are again accelerated by an electric field applied between the first and the second dynode and intrude on the second dynode. This process is repeated as many times as the number of dynodes and finally reaches approximately $10^6$ electrons at the photomultiplier tube's anode. For this process to occur, one or more photoelectrons must be removed from the cathode of the PMTs [2,4,6,71,76,77].

The SE photocathode consists of a metal oxide thin film similar in structure to the dynodes of PMTs. Many photocathodes are made of semiconductor compounds containing alkali metals with low work function values, such as Cs-I, Cs-Te, Sb-Cs, and GaAs [43]. The photocathode of a PMT is usually burned out under high-radiation exposure, so primary photoelectrons cannot be generated, and no signal is received from the anode. The working principle of the SE module is based on generating primary electrons from the first dynode to form a secondary electron array when the photocathode is disabled during the operation. [2,3,43,76,77]. This SE module is also useful for measuring the energy of electromagnetic shower particles interacting with the cathode and dynode materials. In this case, without using scintillators for calorimeters, high energetic particles are detected, and their energy is measured.

Here, we investigated three different voltage configurations for the newly developed SE module and the characterization tests were conducted by using cosmic and gamma radiation sources. Through design and testing, the performance of SE modules under such conditions holds significant importance in developing the frontier of particle detectors and ionization calorimeters.

## 4.3 Technical Design

In this study, the SE modules were modified from conventional PMTs. The main difference of the SE module is that the photocathode and the entire dynode chain are used as SE surfaces for signal acquisition. The construction of the SE module resembles that of the PMT, although with modifications. The difference between the SE module and the PMT lies in its ability to utilize the entire dynode chain as an SE surface for signal acquisition instead of the photocathode, which loses its function. While the most significant signal is initially generated in the photocathode, functioning optimally, it undergoes amplification at the first and continuous dynodes. Therefore, in the new design, the SE modules are sensitive not only to photons but also to electromagnetic and hadronic particles [3,5].

This integrated approach allows for a comprehensive study of signal acquisition and sensitivity in different voltage conditions, shedding light on the performance of SE modules under cosmic and gamma radiation sources. The prototype SE module was assembled using a Hamamatsu single anode R7761 PMT, which was previously used for collecting data in the CDF experiment at Fermi National Accelerator Laboratory (Fermilab) [3,62,63]. The R7761 PMT has 19 dynode stages serving as secondary emissive electrodes in a fine mesh structure, and it has a length of 50 mm and a diameter of 39 mm with an operational window diameter of 27 mm. This prototype was tested with cosmic and gamma rays. Figure 4.1 shows an image of the first SE module. An electronic board was specifically designed and fabricated for the first SE module, as shown in Figure

3.1, which displays the circuit diagram of the electronic board that powers a single PMT and reads the signal from its anode.

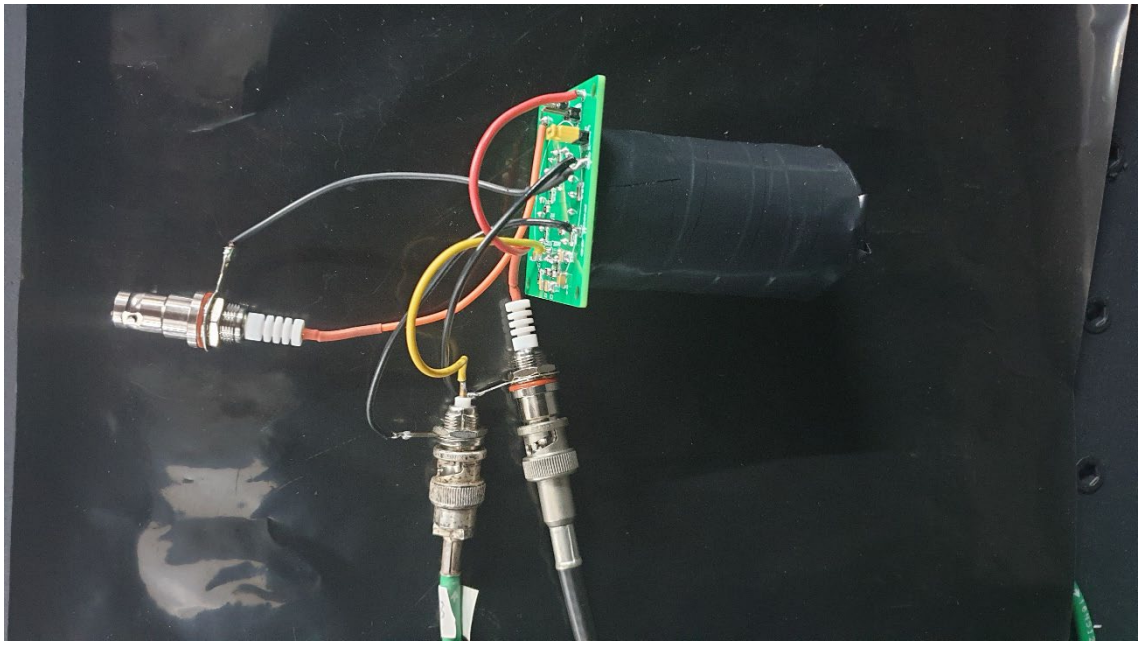

**Figure 4.1** An image of the developed SE module with electronic board on insulated film in dark box.

Three distinct modes of operation are made available for R7761 PMTs on the baseboard. The details of these modes are mentioned below.

### 4.3.1 First Mode

In this mode, also called normal divider mode, the scheme of the photomultiplier voltage divider circuit is preserved. The first mode is activated by closing the JP1 switch and opening the JP2 and JP3 switches as shown in Figure 4.2. Only the resistance between the photocathode and the first dynode has twice the value of the resistances in the voltage divider circuit chain. Since the resistances between subsequent dynodes are equal, the potential difference of the dynode chain is equal. This schematic is based on the Hamamatsu reference design. Cosmic ray measurement tests showed that the first measurable signals from the R7761 PMT started at around –1700V (DC), but the optimum measurement voltage for the three modes was observed at around –2000 V. Therefore, the simulation was carried out by supplying –2000 V to the voltage divider circuit. According to the PSPICE-based simulation for a voltage value of -2000V, -1999.71 V at the photocathode, -1809.37 V at the first dynode, and approximately 95V

between each dynode in the sequential dynode chain, dropping to 0 V at the anode. The reason for measuring -1999.71 V at the photocathode is due to the 1 kΩ resistor connected between the high-voltage power supply and the photocathode. The voltage difference between the photocathode and the first dynode is predicted to be 190V, about twice the value of 95 V in the dynode chain.

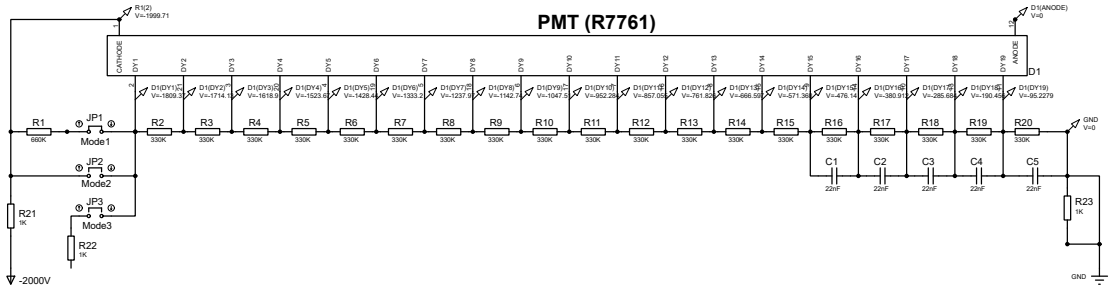


**Figure 4.2** Schematic circuit diagram of the SE voltage divider for R7761 PMTs for Mode 1.

### 4.3.2 Second Mode

There is a 660 kΩ resistor in the first mode between the photocathode and the first dynode, resulting in a potential difference between the photocathode and the first dynode. This resistance is removed in the second mode, and the photocathode and the first dynode are directly connected (short-circuited). This mode is created by closing the JP2 switch and opening the JP1 and JP3 on the electronic circuit board as shown in Figure 4.3. Therefore, there is no potential difference between the photocathode and the first dynode, so the voltage values at these two points are the same. When –2000 V is applied in the voltage simulation, -1999.68 V is observed at these points. Due to a 1 kΩ resistor connecting between the high voltage source and the connected photocathode-first dynode node, the voltage drops about 0.32 V. In the dynode chain after the first dynode, approximately 105.25 V drops between each dynode, reaching 0 V at the anode.

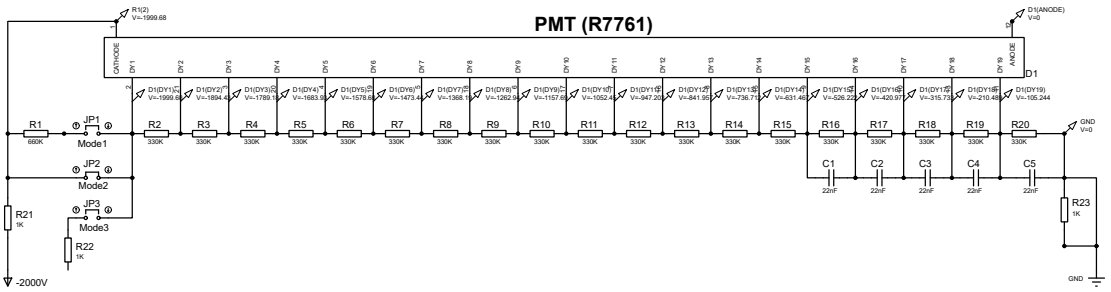


**Figure 4.3** Schematic circuit diagram of the SE voltage divider for R7761 PMTs for Mode 2.

### 4.3.3 Third Mode

Unlike the first and second modes, the photocathode is wholly deprived of voltage in the third mode. In this mode, which requires a second power supply to be connected to the circuit, the dynode chain must be separated from the photocathode and fed by this different high-voltage source. This mode was created by turning on switches JP1 and JP2 on the electronic circuit board and turning off switch JP3. In this mode, the voltage value will be 0 V because the photocathode is disconnected from the voltage divider circuit, but there are two cases for the voltage of the first dynode: -1810 V in the first mode and –2000 V in the second mode as shown in Figure 4.4 and Figure 4.5. The voltage value of the other dynodes in the voltage divider circuit is the same as in the first mode for –1810 V and in the second mode for –2000 V.

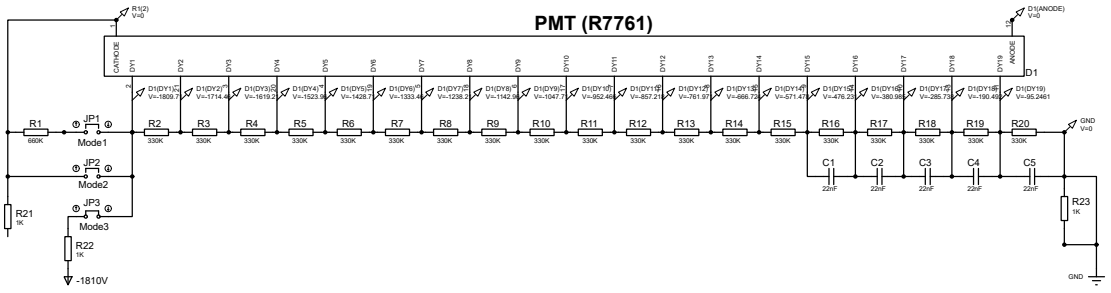


**Figure 4.4** Schematic circuit diagram of the SE voltage divider for R7761 PMTs for Mode 3 at -2000V at first dynode.

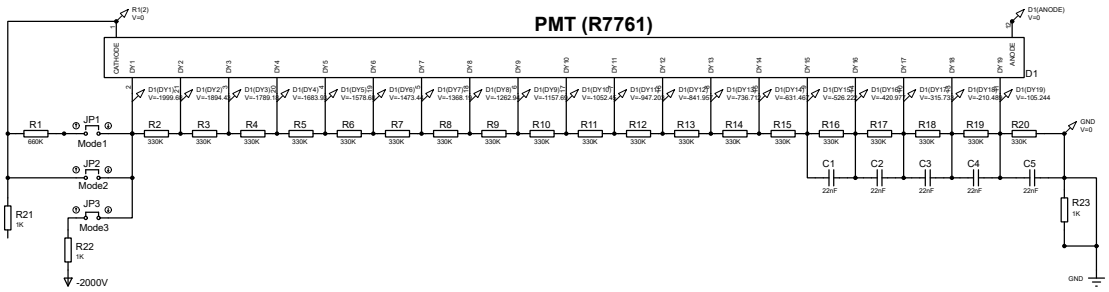


**Figure 4.5** Schematic circuit diagram of the SE voltage divider for R7761 PMTs for Mode 3 at -1810V at first dynode

# 4.4 Experimental Setup

Before proceeding with the radiation tests, we performed characterization tests on the voltage divider electronic board. First, voltage jumps, or short circuit situations were tested since they use high voltage. Problems were observed in the circuit due to the high voltage, and the necessary isolations were made. After determining that the board had no problem by using proper equipment, the SE module was developed by soldering the photomultiplier tube to the electronic board. The photomultiplier tube was covered with light-insulating foil and black insulating tape to prevent light entering the tube. The PMT module was also wrapped in light-insulating foil and placed in a dark box. All measurements were performed in such an environment, which can be seen in Figure 4.6.

**Figure 4.6** Experimental setup for cosmic and gamma radiation tests

The module was then connected to a high-voltage source, and voltage was gradually applied from 0 V up to -2000 V, where we obtained a clear signal. We first conducted cosmic background radiation tests before moving on to gamma-ray testing. The measurement scheme for the cosmic ray test is shown in Figure 4.7 and the measurement scheme for the gamma test is shown in Figure 4.8. The results of these tests are used to distinguish and compare the radiation from gamma rays.

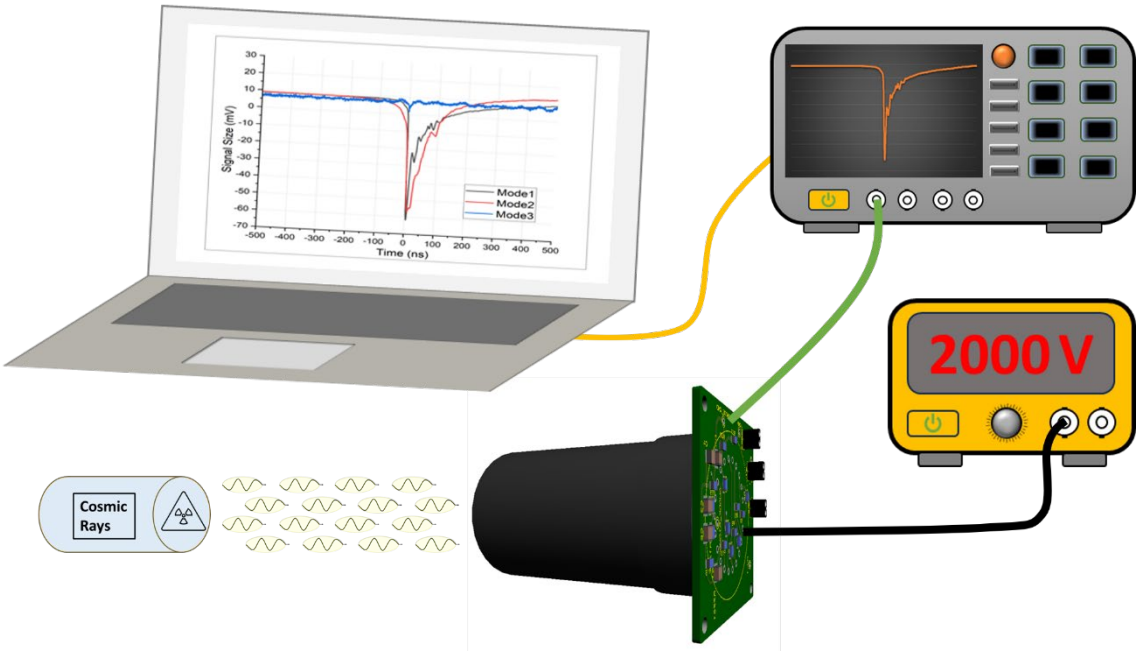


**Figure 4.7** Graphical design of experimental process for characterization and analysis for cosmic rays.

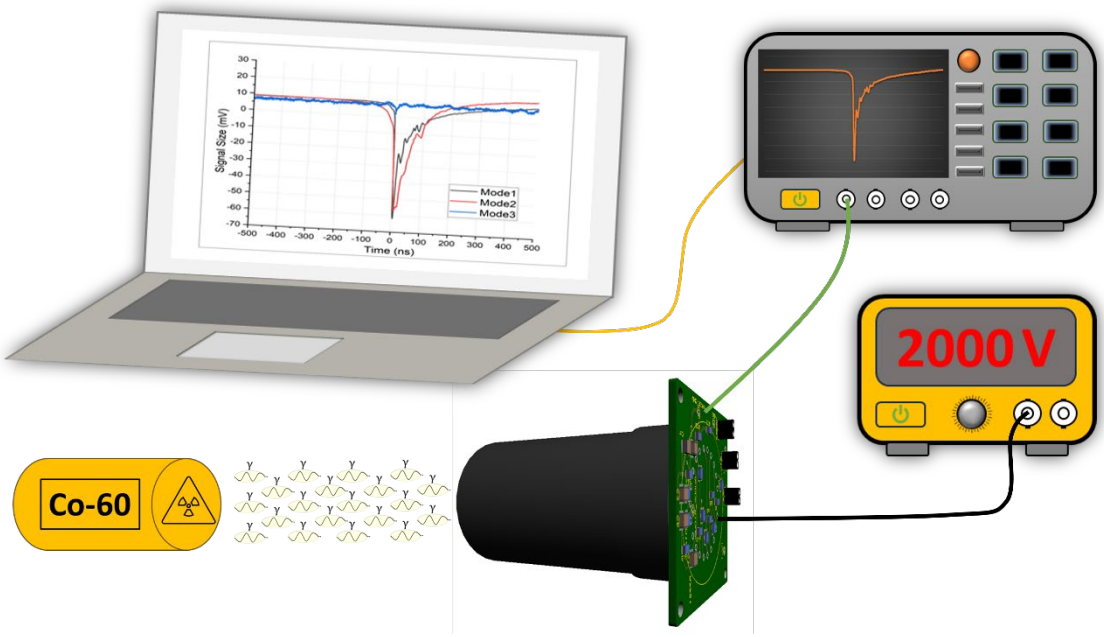


**Figure 4.8** Graphical design of experimental process for characterization and analysis for Co-60 Gamma rays source.

The photodetector tube module, powered by a negative high-voltage power supply, was connected to an oscilloscope, and triggered at –30 mV as shown in Figure 4.6. Since the secondary electrons generated in each mode occur at different frequencies, the measurements were taken based on a specific time interval. The signal collected by the scope was taken in the fast-frame mode of the oscilloscope, and in each mode, we made sure that the sum of the signal received was stable. This result was achieved by recording in between 1k-110k hit (kh) events depending on the mode and radiation source. The data recorded on the oscilloscope were transferred to the computer, and graphs were obtained.

## 4.5 Experimental Results

All three SE module modes were tested with cosmic background radiation and a Co-60 (3.7 MBq) gamma radiation source. For each test, the same experimental setup was used, and the experimental data were taken at room temperature.

### 4.5.1 Cosmic Background Radiation Results

The new module in three different setups is tested with cosmic radiation in a darkbox at our lab at room temperature. Figure 4.9 to Figure 4.14 shows the normalized waveform results of all three modes. For the cosmic radiation test, -30 mV threshold was

applied for all 3 modes, and 40kh events, 8kh events, 1kh events were taken in the fast-frame mode of the oscilloscope for Mode 1, Mode 2, Mode 3 at –1810 V, and Mode 3 at –2000 V, respectively. All three modes were powered at negative 2000 V and all the acquired data in waveform (WFM) and comma-separated values (CSV) format were comprehensively analyzed. In Figure 4.9, the 10mV offset was due to the setting of the oscilloscope. As shown in Figure 4.9, Mode 1 and Mode 2 have significant signal sizes as compared to Mode 3, which is due to the cosmic particle interactions. The approximate signal sizes: ~70 mV for Mode 1, ~65 mV for Mode 2, ~8 mV for Mode 3 at –1810 V and ~15 mV for Mode 3 at –2000 V. This shows that Mode 3 is not responsible for cosmic radiation even at high voltages. The reason is that the photocathode is fully excluded from the voltage-divider chain, so the cosmic interaction's surface area decreases significantly. As expected, the signal width of Mode 2 is wider than Mode 1 because in Mode 2 both photocathode and first dynode are shorted. This causes an after-pulse addition to the primary signal due to cosmic interactions with photocathode material.

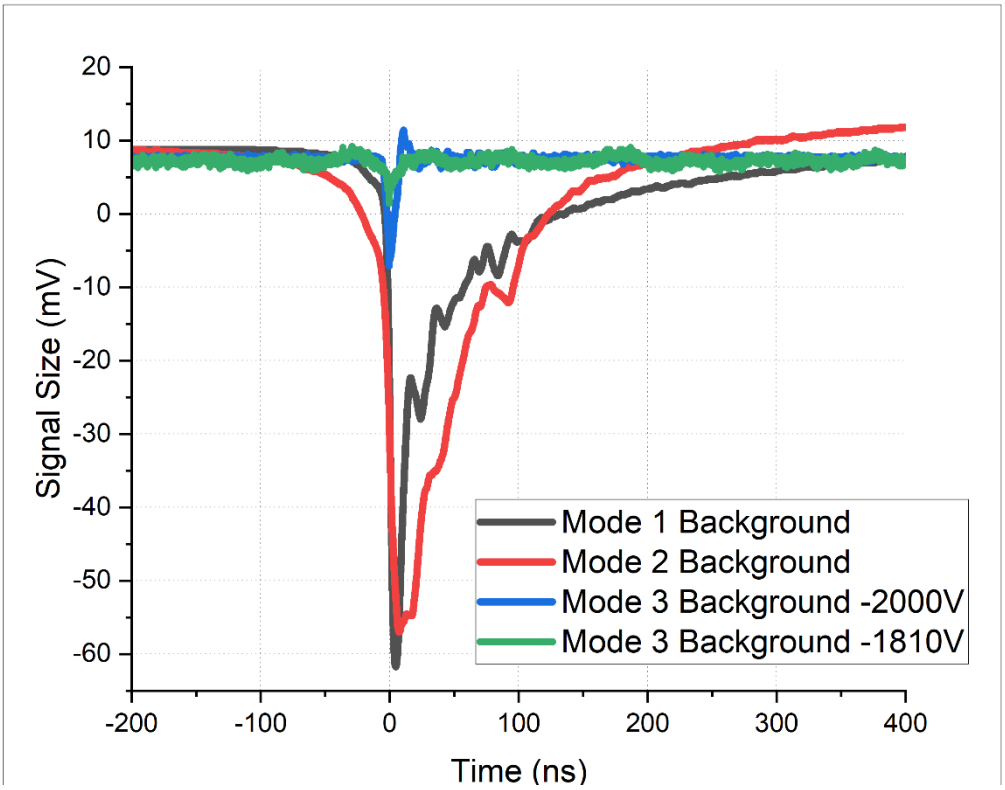


**Figure 4.9** Cosmic background radiation test results for all three modes.

### 4.5.2 Co-60 Gamma Radiation Results

All three modules were also tested for Co-60 gamma radiation. A -30mV threshold was uniformly applied for all 3 modes. Afterward, event counts of 110kh, 130kh, 50kh, and 90kh were obtained in the fast-frame mode of the oscilloscope for Mode 1, Mode 2, Mode 3 with bias voltage of –1810 V, and Mode 3 with a bias voltage of -2000 V, respectively.

As demonstrated in Figure 4.10, Mode 1 and Mode 2 exhibit comparable signal sizes in contrast to Mode 3 for gamma radiation detection. The approximate signal sizes are as follows: ~63 mV for Mode 1, ~46 mV for Mode 2, ~43 mV for Mode 3 at –1810 V and ~47 mV for Mode 3 at –2000 V.

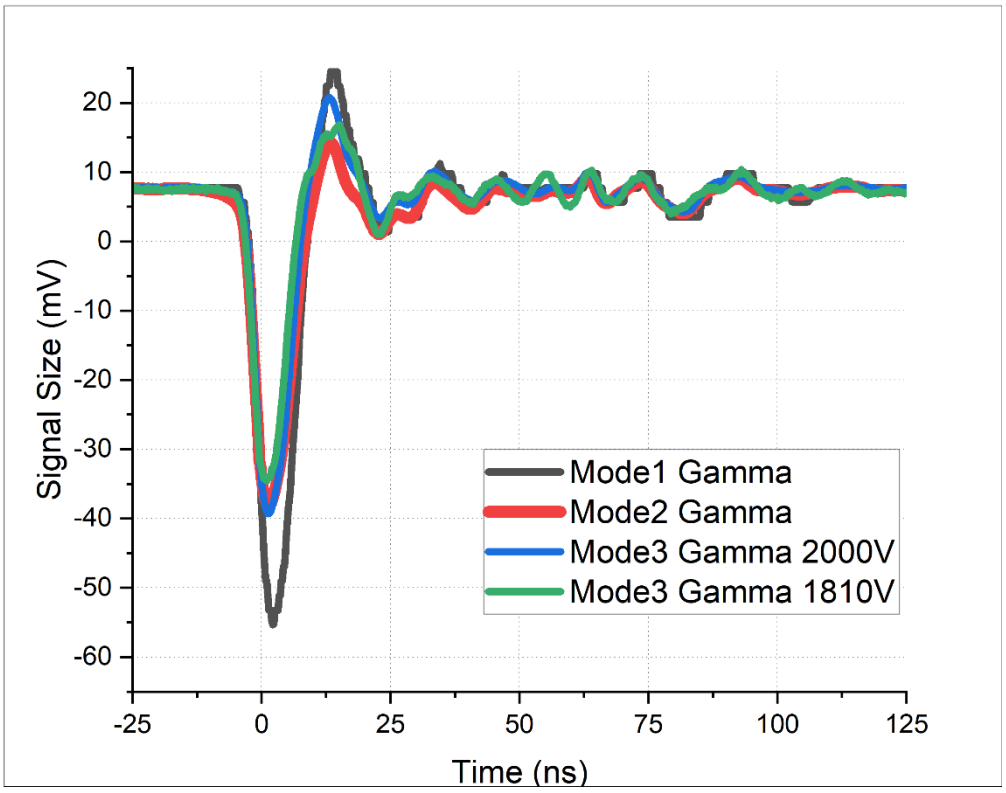


**Figure 4.10** Co-60 gamma source test results for all three modes.

Figure 4.11 shows the compared cosmic background and Co-60 gamma radiation response of Mode 1, which reveals significant variations in signal characteristics between background and gamma radiation. The background signal demonstrates a width of 58 ns and the full width at half maximum (FWHM) is 23 ns. The gamma radiation signal shows a narrower width of 14 ns and an FWHM of 8 ns. The wider width of the background

signal is attributed to the flux of the higher energetic cosmic particles forming the background radiation.

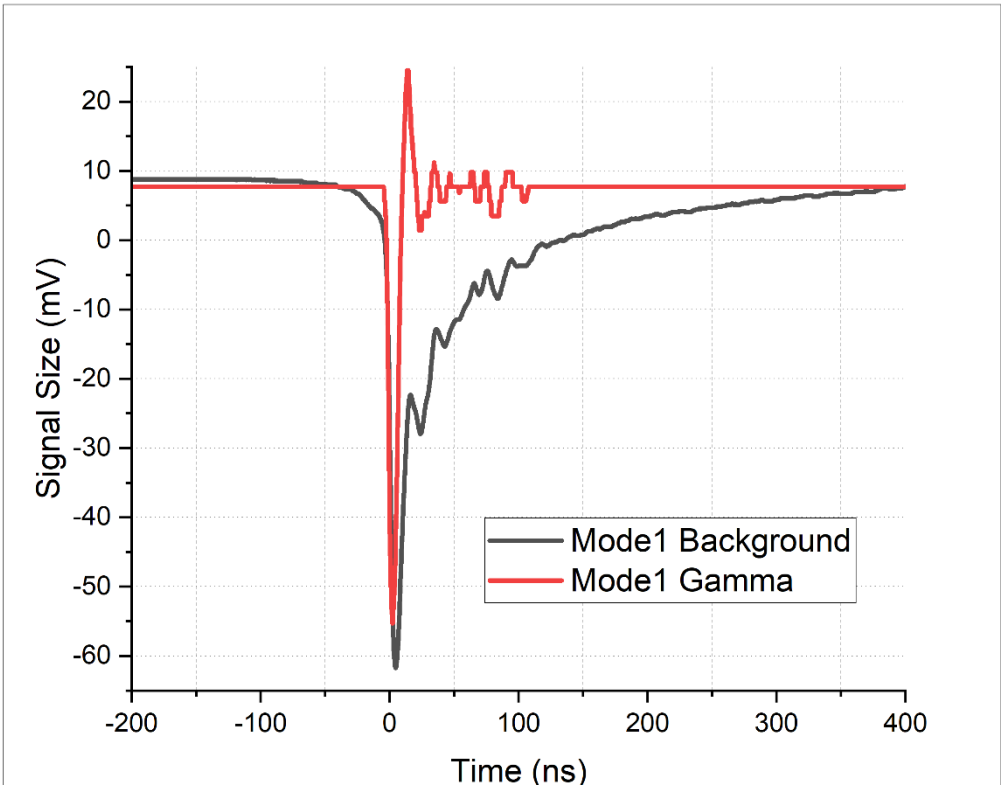


**Figure 4.11** Cosmic background and Co-60 gamma source radiation test results for Mode 1.

Figure 4.12 compares the signals in Mode 2 as a response to cosmic radiation and the Co-60 gamma radiation. It shows the background signal's width is 680 ns and the FWHM is 53 ns, while the gamma signal's is 20 ns and the FWHM is 7 ns. Such a detector system is not desirable for measuring cosmic background radiation because the background signal width is too broad, even though it gives a high peak value. The short-circuiting of the photocathode and the first dynode in the Mode 2 design causes the surfaces forming the secondary electrons to grow. This leads to the formation of a broad tail behind the peak. The gamma radiation peak is lower than the cosmic radiation peak but shows a steep peak. This indicates that our new detector system functions well for electromagnetic interactions.

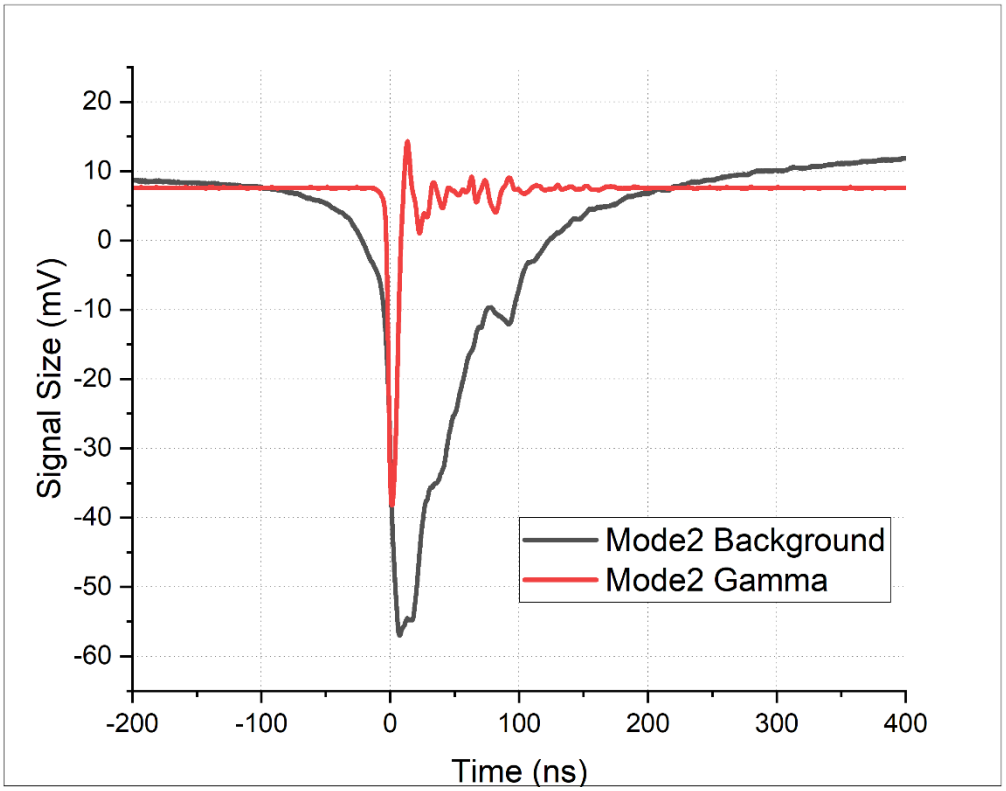


**Figure 4.12** Cosmic background and Co-60 gamma source radiation test results for Mode 2.

Figure 4.13 shows the cosmic background compared to the Co-60 gamma radiation response of Mode 3 at –1810 V. Figure 4.14 illustrates the cosmic background and Co-60 gamma radiation response of Mode 3 at –2000 V. As mentioned above, two conditions determine the voltage value of the first dynode: first, the value of-1810 V in Mode 1 and –2000 V in Mode 2. Measurements were taken for these two voltage values in cosmic background and gamma radiation tests. These measurement results are given in Figure 4.13 and Figure 4.14. Figure 4.13 shows that for -1810V, no background signal is observed, and the gamma signal has a width of 16 ns and FWHM of 6 ns. Figure 4.14 shows that for –2000 V, the width of the background signal is 18 ns and FWHM is 3 ns, while the width of the gamma signal is 18 ns and FWHM is 6 ns. Looking at the background radiation curves, no peak was obtained at –1810 V, while a peak of ~16 mV was obtained at –2000 V. In additional tests, peaks around ~50 mV were observed when –2300 V and -2400 V were applied outside the operating voltage of the detector.

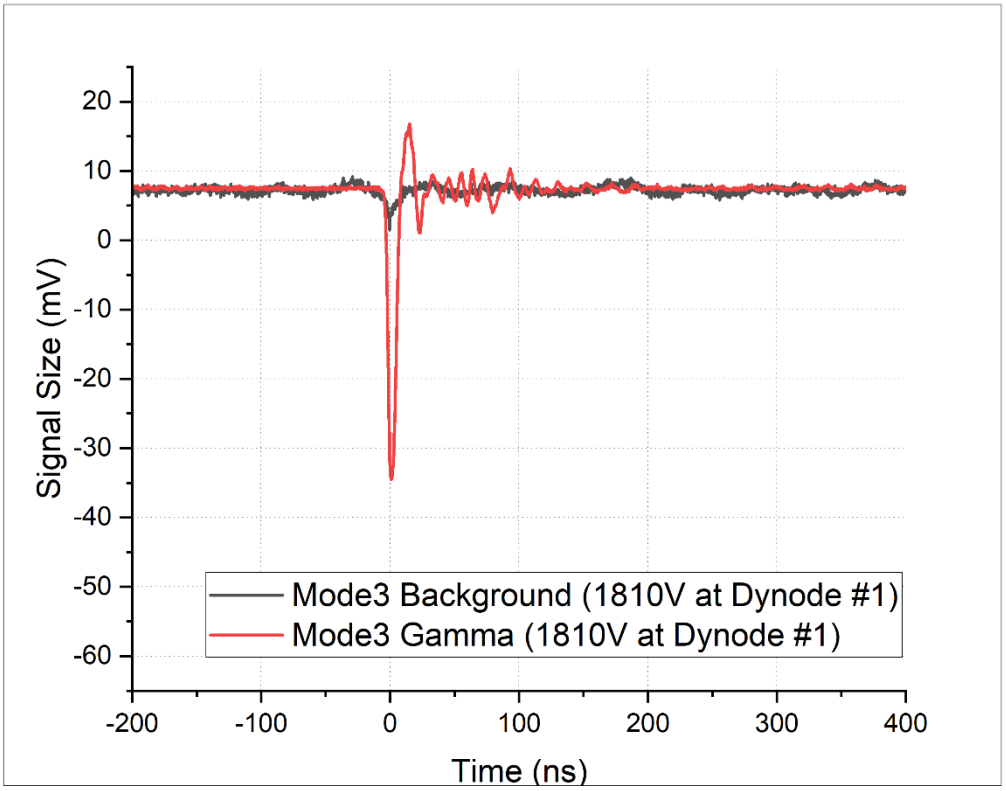


**Figure 4.13** Cosmic background and Co-60 gamma source radiation test results for Mode 3 when –1810V voltage applied to the first dynode.

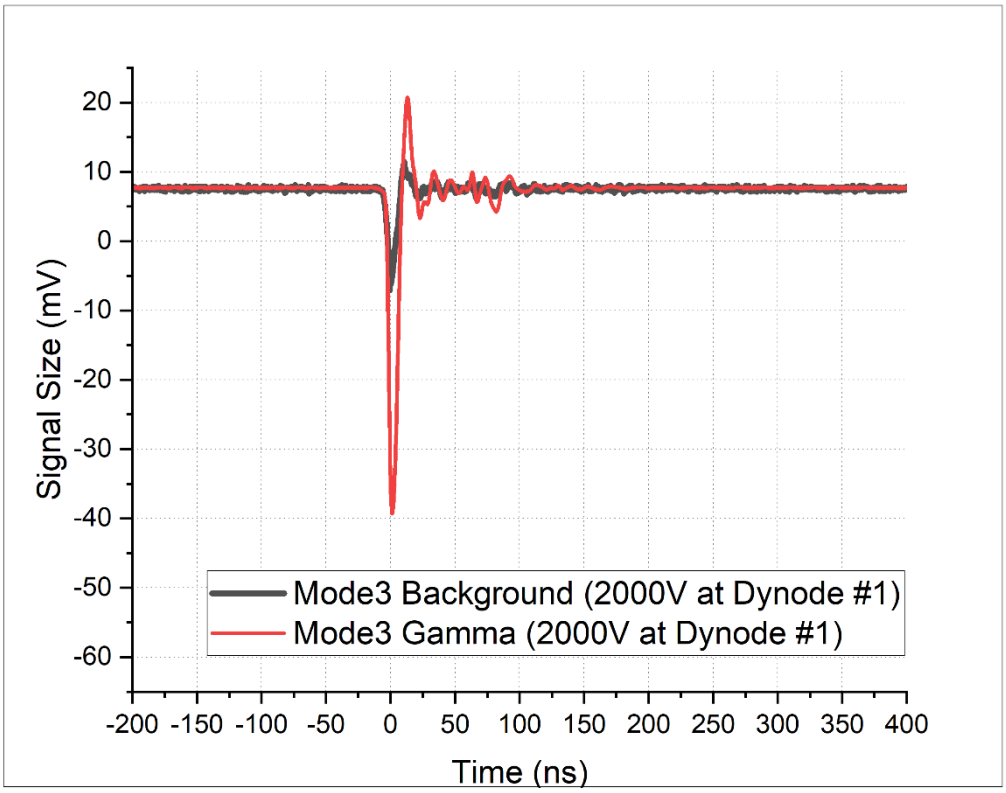


**Figure 4.14** Cosmic background and Co-60 gamma source radiation test results for Mode 3 when –2000V voltage applied to the first dynode.

Although, the results show higher peak values for the cosmic background, the low flux density of the cosmic radiation contributes to the larger signal width. However, the Co-60 gamma radiation plots show a steep peak with a narrow signal width, indicating that the detector system is well-suited for the gamma radiation and electromagnetic shower interactions.

The sizes, widths, FWHM values and number of hits per second of the signals received with cosmic background and Co-60 Gamma in all modes are tabulated in Table 4.1.

**Table 4.1: Cosmic Background and Co-60 Gamma radiation measurement results**

| Radiation Type | Mode | Signal Size (apprx) (mV) | Signal Width (apprx) (ns) | FWHM (apprx) (ns) | hits/s |
|---|---|---|---|---|---|
| **Cosmic** | Mode1 | 70 | 58 | 23 | 3,56 |
| | Mode2 | 65 | 680 | 53 | 0,24 |
| | Mode3 -1810V | 8 | - | - | - |
| | Mode3 -2000V | 15 | 18 | 3 | 0,06 |
| **Gamma** | Mode1 | 63 | 14 | 8 | 2778 |
| | Mode2 | 46 | 20 | 7 | 6,67 |
| | Mode3 -1810V | 43 | 16 | 6 | - |
| | Mode3 -2000V | 47 | 18 | 6 | 1,58 |

## 4.6 Detecting Gamma and Neutron Particles with Integrated Gadolinium (Gd)-Doped Glass

Elements such as Gadolinium (Gd), Boron (B), and Lithium (Li) are frequently utilized for neutron detection. We used gadolinium (Gd)-doped glass to enhance the efficacy of the PMTs in detecting gamma and neutron particles. Gd possesses a markedly greater neutron capture cross-section for low-energy neutrons (<1 eV) compared to other elements. In contrast to other materials, Gd demonstrates no variations in its neutron capture cross-section within the energy range of 1 eV to 500 eV. Gadolinium isotopes have significant efficacy in neutron capture and gamma ray production. When Gd-157 reacts with neutrons, it converts to Gd-158 and emits gamma radiation. Gd-157 is

extensively utilized in neutron detectors due to its superior neutron capture cross-section compared to other elements, retaining this sensitivity across various energy levels. This integration offers advantages such as heightened efficiency in neutron detection attributable to Gd's elevated neutron capture cross-section, greater overall sensitivity, and signal resolution of the PMTs, and improved resilience in high-radiation conditions.

We carried out the substrate preparation and gadolinium (Gd) thin film deposition process as follows. Flat glass slides measuring 75x52mm with a thickness of 1 mm were utilized as substrates for the deposition of Gd thin film layers. In advance of deposition, the substrates underwent a sequential ultrasonic bath treatment in acetone, isopropanol, and deionized water, followed by nitrogen gas drying to eliminate any impurities. Gadolinium thin films were deposited on the prepared glass substrates utilizing the Electron Beam Evaporation (E-beam) process. Gd thin film layers of two different thicknesses, 100nm and 500nm, were grown. In the test process, two 500nm Gd-coated glasses were used for 1000nm measurements and three 500nm Gd-coated glasses were used for 1500nm measurements. The E-beam deposition technique was performed at a base pressure of $10^{-7}$Pa in a high vacuum chamber to reduce oxidation and contamination during deposition. Initially, the prepared glass substrates were positioned within the E-beam chamber, which was then evacuated to a pressure of $5x10^{-7}$ Pascal (Pa). Upon beginning of the procedure, an electric current was applied to a conductive filament, resulting in its heating and subsequent electron emission. A voltage of approximately 6 kilovolts was subsequently supplied between the center and filament to propel the electrons towards the granular Gd designated for deposition. A robust magnetic field channels these electrons into beams, subsequently directing them towards the deposition material. Upon collision, the high-energy electrons induced the evaporation of the substance, which then deposited onto the glass substrates. The thicknesses of the formed Gd film layers were measured in situ during deposition utilizing a crystal microbalance (QCM) incorporated into the E-beam deposition chamber. This real-time monitoring facilitated accurate regulation of the film's thickness. The fabrication procedures for the Glass-Gd are illustrated in Figure 4.15.

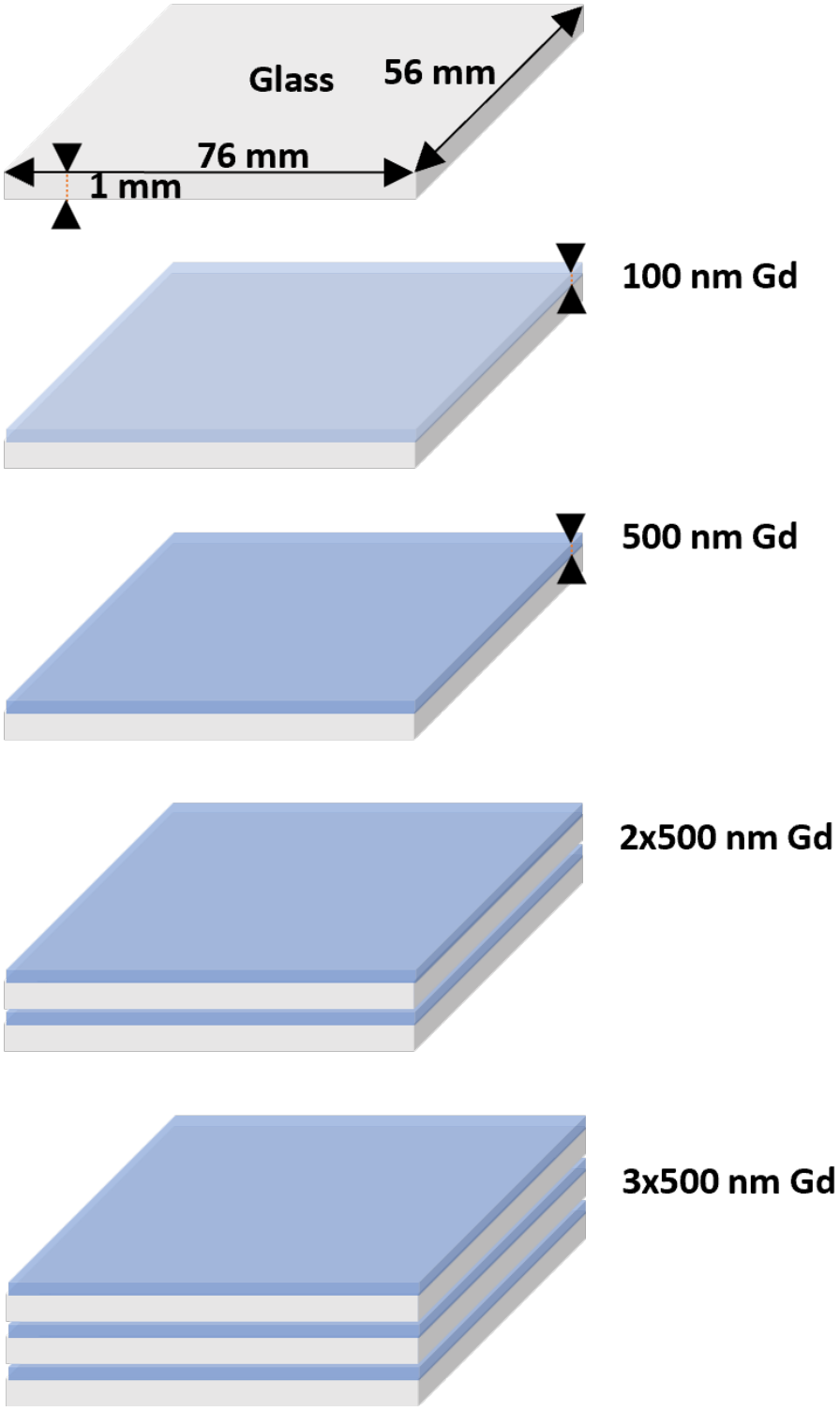


**Figure 4.15:** Fabrication of Gadolinium (Gd) Thin Film Layers on Glass Substrates by E-beam Deposition Techniques.

Table 4.2 gives the approximate values of the signal sizes obtained as a result of measurements with Gd-coated glasses with 100nm, 500nm, 1000nm, and 1500nm thickness for Mode 1, 2, and 3 radiated with the neutron source (Am-241/Be, 3.3 MBq).

**Table 4.2: The approximate signal sizes of Mode 1, 2 and 3 with a Gd-coated sample mounted on the PMT due to neutron irradiation.**

| Gd Thickness (nm) | Mode1 (mV) | Mode2 (mV) | Mode3 (mV) |
|---|---|---|---|
| **100** | 88,68 | 39,67 | 37,05 |
| **500** | 87,23 | 39,81 | 36,94 |
| **1000** | 86,97 | 38,88 | 35,09 |
| **1500** | 85,78 | 39,02 | 35,75 |

Figure 4.16 shows the pulse shapes of all three modes obtained from measurements with Gd-coated glasses with thicknesses of 100nm, 500nm, 1000nm, and 1500nm due to neutron irradiation. As seen in Figure 4.16, the highest signal size can be obtained in Mode1. The signal sizes of modes 2 and 3 are close to each other and approximately half the size of Mode1. From this, we can conclude that Mode1 is the most suitable mode for Gd-coated measurements even if Mode2 and Mode3 are also sensitive to the Gd-coated measurements. It is also observed that the Gd coating thickness for all modes does not significantly change the signal strength. Therefore, in the range we have studied, applying a certain Gd coating thickness is unnecessary to keep the signal strength at a certain level.

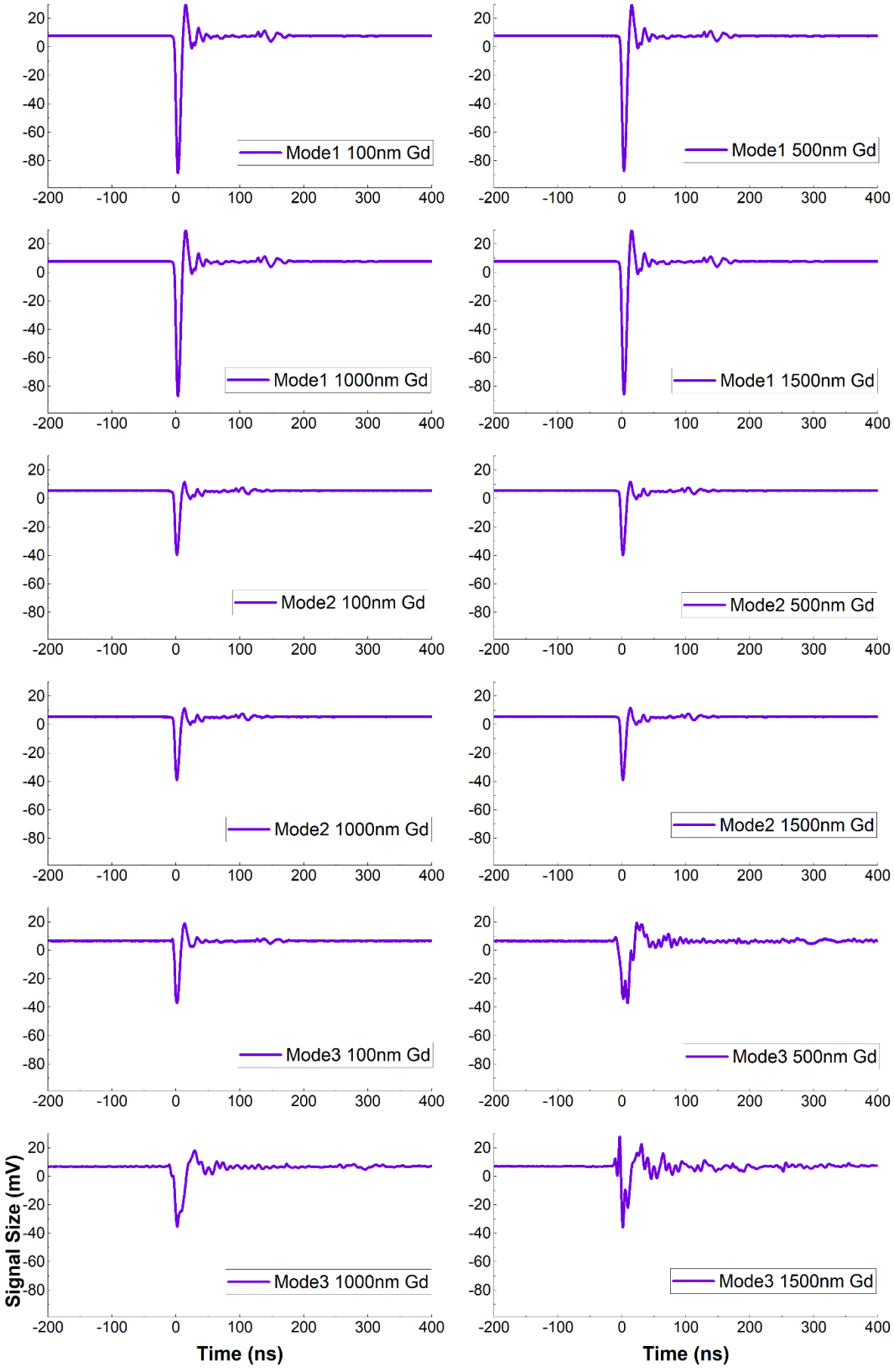


**Figure 4.16:** Pulse shapes of all three modes of the SE calorimetry module with Gd-coated glasses with thicknesses of 100nm, 500nm, 1000nm, and 1500nm due to neutron irradiation.

Figure 4.17 displays the linearization plot of the approximate signal sizes obtained from measurements with Gd-coated glasses with thicknesses of 100nm, 500nm, 1000nm, and 1500nm for Mode 1, 2, and 3 due to neutron irradiation.

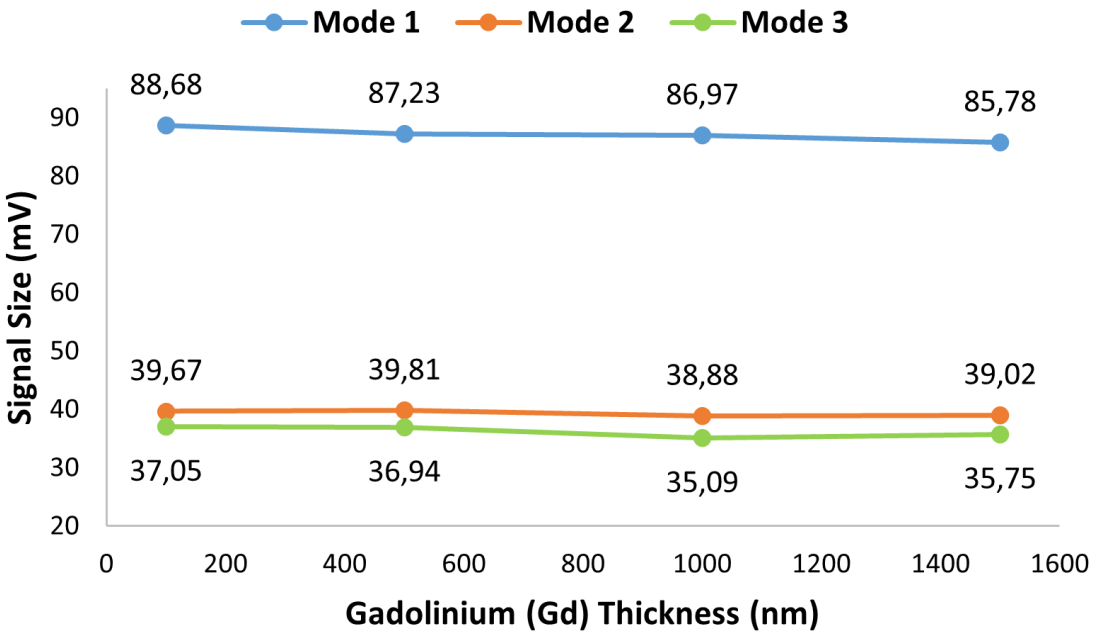


**Figure 4.17:** The signal sizes of all three modes versus Gd thickness due to neutron irradiation.

Figure 4.18 illustrates the pulse shapes due to cosmic rays, gamma rays, neutron, and beta (Sr-90, 3.7 kBq) irradiation. All are obtained in Mode 1 using a 500 nm thick Gadolinium (Gd)-coated glass mounted on the PMT. As shown in the Figure 4.18, the neutron signal is significantly larger compared to the signals from the other radiation sources. This heightened response to neutrons is attributed to Gadolinium's high neutron capture cross-section, which enhances the detector's sensitivity to neutrons. In contrast, the signals from cosmic rays, gamma rays, and beta radiation are identical in magnitude, indicating a similar response to these forms of radiation. This uniformity suggests that the detector, while efficient at all sources mentioned above, has a particularly strong sensitivity to neutrons (as developed with Gd-coated materials) making it well-suited for applications that require precise neutron detection.

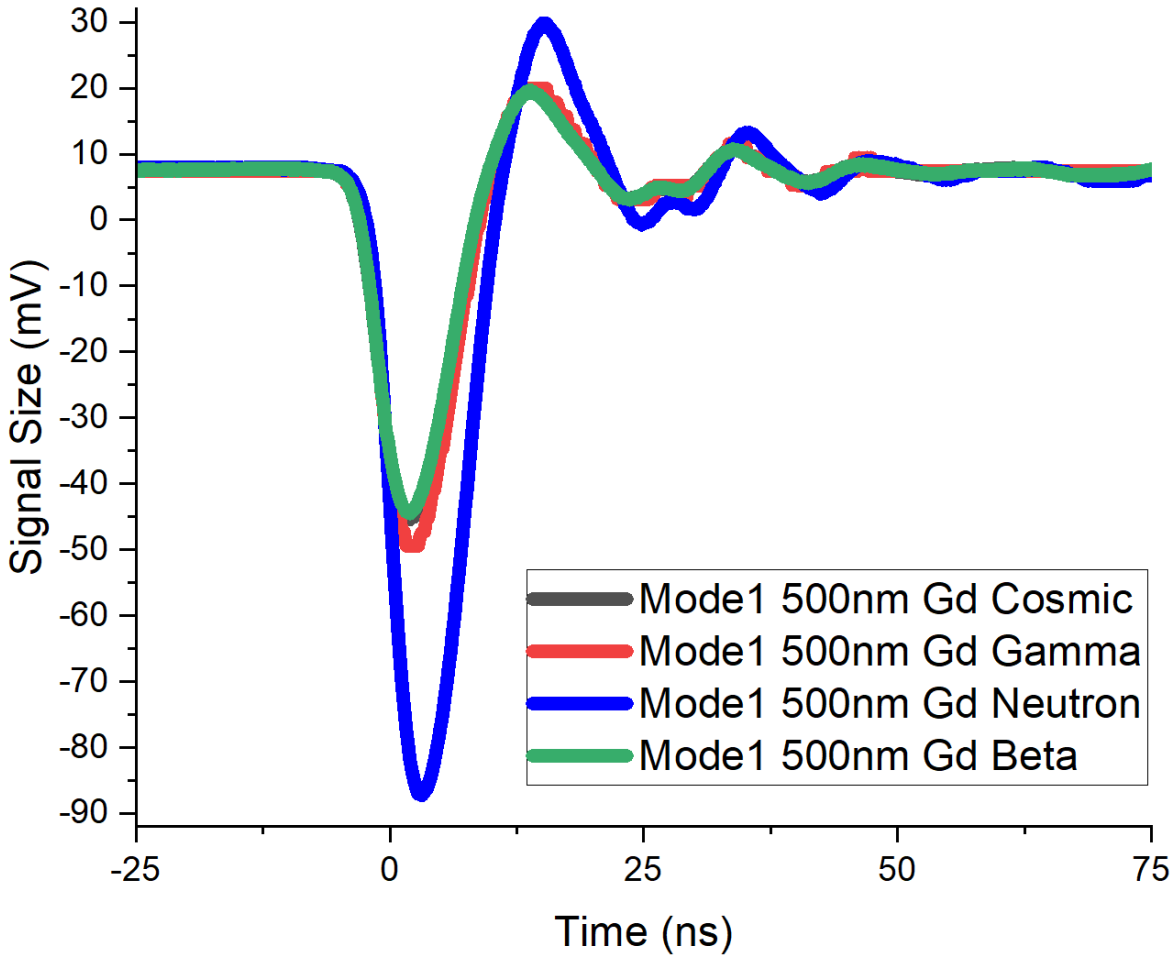


**Figure 4.18:** The pulse shape comparison of the Mode 1 coupled with 500nm thick Gd-coated glass for Cosmic, Gamma, Neutron and Beta irradiation.

Figure 4.19 displays the pulse shape distrubitions of all three modes coupled with a 500 nm thick Gd-coated glass due to neutron irradiation. Among the three modes, Mode 1 consistently produces the most distinct neutron signals, showcasing a significant enhancement attributed to the Gd coating. In contrast, Mode 3 exhibits noticeable signal distortion, indicating reduced accuracy in neutron detection under these settings. Mode 2 also provides less pronounced signals compared to Mode 1, though without the severe distortions seen in Mode 3. The larger neutron signal observed in Mode 1 emphasize its superior sensitivity and suitability for neutron measurements, as the Gd layer effectively amplifies the detector's response to neutrons. This comparison highlights the critical role of mode selection in ensuring accurate and reliable neutron detection. Mode 1 emerges as the optimal choice, while Modes 2 and 3 are less effective, particularly for precise measurements, emphasizing the importance of careful calibration and configuration when

using Gd-coated detectors. The double-pulse shape of the Mode 3 is believed to be due to the afterpulse interaction of the delayed gammas produced by Gd atoms due to the capture of the neutrons. Both Mode 2 and Mode 3 would be developed as a sensitive modes to neutrons after careful optimization studies.

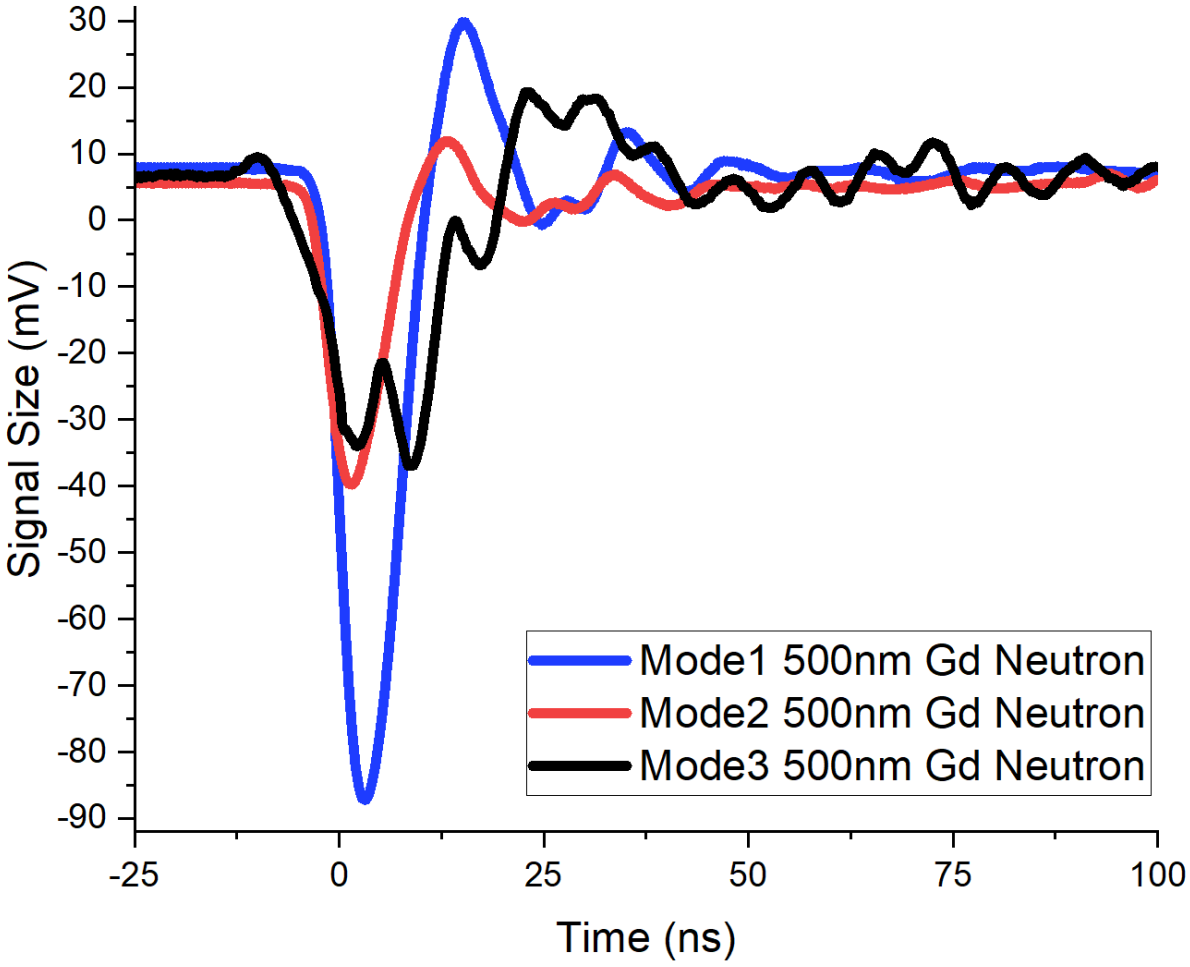


**Figure 4.19:** Pulse shape comparison of all three modes coupled with a 500nm thick Gd-coated glass due to neutron irradiation.

## 4.7 Conclusions

In this chapter, we talk about particle detectors operating in high radiation environments. First, we provided information about the studies to solve the problems of particle detectors operating in high-radiation environments. Then, we explain one of these solutions, the secondary electron calorimeter. Then, the electronic cards designed and produced for the thesis were designed and manufactured, and the results of the R7761 photomultiplier tube tests were obtained. Finally, the data obtained from our characterization tests with cosmic background radiation, gamma rays, Beta particles and neutron irradiation are presented and explained with graphs.

# Chapter 5

# Conclusions and Future Prospects

## 5.1 Conclusions

In this study, three novel Secondary Emission (SE) Ionization Calorimetry modules with a remote-controlled electronic board were developed from conventional Photomultiplier Tubes (PMTs). All three modes and the electronic board were simulated and tested for electronic characteristics. All three SE modes were tested with cosmic background radiation, Co-60 gamma source, Sr-90 Beta source, and Am-241/Be neutron source in a dark box at room temperature.

The experimental results confirm the expected outcomes regarding the signal sizes and width disparity between the Modes conditions. Mode 1 and Mode 2 have larger signal sizes than Mode 3, which illustrates that Mode 3 is not responsible for cosmic radiation even at high voltages. Also, the wider signal width observed in Mode 2, attributed to the shorting of both the photocathode and first dynode, underscores the impact of the cosmic interactions with metal-oxide materials, resulting in after-pulse additions to the first signal. The comparative analysis of the three Modes graphs reveals a significant temporal mismatch between cosmic radiation and Co-60 gamma radiation signals. This difference is attributed to the inherent characteristics of the radiation sources: cosmic radiation exhibits low flux with high-energy particles, while Co-60 gamma radiation shows a high flux with lower energy. The results showed that all three modes are functional as expected. Also, the integrated modes with a 500-nm thick Gd glass were tested, and they gave a promising result for the newly developed SE module, which is suitable for neutron applications.

Developing such modules is critical for radiation-resistant nuclear and high-energy detectors, which are used in high-radiation environments. This integrated approach sheds light on a future comprehensive study of signal acquisition and sensitivity for particle detectors in harsh radiation zones such as accelerators, space, and nuclear applications.

## 5.2 Societal and Scientific Impacts

Nuclear Instruments and Particle Detector Technologies are classified as one of critical technologies according to the 12th Development Plan of the Turkish Government. Detectors, calorimeters, and accelerators are so important for natural science experiments to solve the mysterious problems in Physics, and related fields. In addition, the detector technologies are crucial for medical, industrial and homeland security applications such as cancer therapy, diagnostic instrumentation, monitoring nuclear waste nonproliferation, biomedicine, and drug development, etc. A higher level of performance of calorimeters, including high resolution, fast response time and good radiation hardness features, is demanded for novel technological developments. The prospects for future advances in calorimetry are bright. The nature of new capabilities, and hence of the applications, will depend on broad areas such as research & development, and reindustrialization. Hence, working in this area will be beneficial to industry and society.

## 5.3 Future Prospects

Since the research and development studies of nuclear electronics, which is the subject of this thesis, are limited in our country, this study offers a good environment for future studies in the field. While the electronic cards we have developed are currently tailored for the R7761 photomultiplier detector, the knowledge and experience we have gained in their design and production opens exciting possibilities. We are confident that this expertise will allow us to adapt these cards for use with various other photomultiplier tubes, paving the way for diverse applications in the future.

Since the photomultiplier tubes are fabricated and mass-produced, calibration tests are required. We can perform characterization tests in our laboratory for the newly developed electronic modules. Here, we produced new modules for a single PMT but in future, we can produce new modules for both several types and multiple PMTs.

In this study, we switched between modes and turned the high voltage on and off by using remote controlled environment. However, the HV power supply unit's application was used to control the high-voltage source in general. In the future, we are aiming to develop a more comprehensive module that will be useful for controlling and data acquisition of the HV power supply, and data taking remotely.

In this study, we developed a new Secondary Emission (SE) module by altering the design of the photomultiplier tube technology, but in the future, we would like to develop an extremely sensitive and radiation-resistant SE detector from scratch in a clean-room environment.

# BIBLIOGRAPHY


[1] P.W. Nicholson, Nuclear electronics, (1974).

[2] D.R. Winn, Y. Onel, Secondary Emission Calorimeter Sensor Development, J Phys Conf Ser 404 (2012) 012021.

[3] B. Bilki, K. Dilsiz, H. Ogul, Y. Onel, D. Southwick, E. Tiras, J. Wetzel, D.R. Winn, Secondary Emission Calorimetry, Instruments 6 (2022) 48. https://doi.org/10.3390/INSTRUMENTS6040048.

[4] E. Tiras, K. Dilsiz, H. Ogul, D. Southwick, B. Bilki, J. Wetzel, J. Nachtman, Y. Onel, D. Winn, Characterization of photomultiplier tubes in a noveloperation mode for Secondary Emission IonizationCalorimetry, Journal of Instrumentation 11 (2016).

[5] E. Tiras, Beam test results of Secondary Emission Ionization Calorimetry modules at Fermilab, Nucl Instrum Methods Phys Res A 1049 (2023) 168083. https://doi.org/10.1016/J.NIMA.2023.168083.

[6] L. Cerrito, Radiation and Detectors: Introduction to the Physics of Radiation and Detection Devices, 1st ed., Springer, 2017.

[7] P.A.M. Dirac, The quantum theory of the electron, Proceedings of the Royal Society of London. Series A, Containing Papers of a Mathematical and Physical Character 117 (1928) 610–624.

[8] C.D. Anderson, The Positive Electron, Physical Review 43 (1933) 491.

[9] R.H. Dicke, P.J.E. Peebles, P.G. Roll, D.T. Wilkinson, Cosmic black-body radiation., Astrophysical Journal, Vol. 142, p. 414-419 142 (1965) 414–419.

[10] A.A. Penzias, R.W. Wilson, A measurement of excess antenna temperature at 4080 MHz, in: A Source Book in Astronomy and Astrophysics, 1900–1975, Harvard University Press, 1979: pp. 873–876.

[11] J.C. Mather, et al., A Preliminary Measurement of the Cosmic Microwave Background Spectrum by the Cosmic Background Explorer (COBE) Satellite, ApJL 354 (1990) L37. https://doi.org/10.1086/185717.

[12] J.C. Mather, et al., Measurement of the Cosmic Microwave Background Spectrum by the COBE FIRAS Instrument, ApJ 420 (1994) 439. https://doi.org/10.1086/173574.

[13] R. Bellotti, F. Cafagna, M. Circella, C.N. De Marzo, R.L. Golden, S.J. Stochaj, M.P. De Pascale, A. Morselli, P. Picozza, S.A. Stephens, Balloon measurements of cosmic ray muon spectra in the atmosphere along with those of primary protons and helium nuclei over midlatitude, Physical Review D 60 (1999) 052002.

[14] R. Bellotti, F. Cafagna, M. Circella, G. De Cataldo, C.N. De Marzo, N. Giglietto, P. Spinelli, R.L. Golden, S.A. Stephens, S.J. Stochaj, Measurement of the negative muon spectrum between 0.3 and 40 GeV/c in the atmosphere, Physical Review D 53 (1996) 35.

[15] M. Boezio, V. Bonvicini, P. Schiavon, A. Vacchi, N. Zampa, D. Bergström, P. Carlson, T. Francke, P. Hansen, E. Mocchiutti, Energy spectra of atmospheric muons measured with the CAPRICE98 balloon experiment, Physical Review D 67 (2003) 072003.

[16] M. Boezio, P. Carlson, T. Francke, N. Weber, M. Suffert, M. Hof, W. Menn, M. Simon, S.A. Stephens, R. Bellotti, Measurement of the flux of atmospheric muons with the CAPRICE94 apparatus, Physical Review D 62 (2000) 032007.

[17] S. Coutu, J.J. Beatty, M.A. DuVernois, S.W. Barwick, E. Schneider, A. Bhattacharyya, C.R. Bower, J.A. Musser, A. Labrador, D. Müller, Energy spectra, altitude profiles, and charge ratios of atmospheric muons, Physical Review D 62 (2000) 032001.
[18] B.T. Cleveland, T. Daily, R. Davis, Jr., J.R. Distel, K. Lande, C.K. Lee, P.S. Wildenhain, J. Ullman, Measurement of the Solar Electron Neutrino Flux with the Homestake Chlorine Detector, Astrophys J 496 (1998) 505–526. https://doi.org/10.1086/305343/FULLTEXT/.
[19] A. Fermi, Enrico; Zannoni, On the Quantization of the Monoatomic Ideal Gas, (1999).
[20] P.A.M. Dirac, On the theory of quantum mechanics, Proceedings of the Royal Society of London. Series A, Containing Papers of a Mathematical and Physical Character 112 (1926) 661–677.
[21] A. Borrelli, Bose—Einstein Statistics, Compendium of Quantum Physics (2009) 74–78.
[22] W.R. Leo, Techniques for nuclear and particle physics experiments: a how-to approach, 2nd ed., Springer-Verlag, 1994.
[23] G.F. Knoll, Radiation Detection and Measurement, Proceedings of the IEEE 69 (2010) 830.
[24] J. Sharpe, Nuclear Radiation Detectors, Methuen & Co, Ltd., London, UK (1964).
[25] W.J. Price, Nuclear radiation detection, (1958).
[26] B. Rossi, H. Staub, Ionization chambers and counters, (1949).
[27] D.H. Wilkinson, Ionization Chambers and Counters, Cam, (1950).
[28] J.W. Boag, F.D. Pilling, T. Wilson, Ionization chambers for electron dosimetry, Br J Radiol 24 (1951) 341–344.
[29] J.W. Boag, J. Currant, Current collection and ionic recombination in small cylindrical ionization chambers exposed to pulsed radiation, Br J Radiol 53 (1980) 471–478.
[30] J.W. Boag, Ionization chambers, The Dosimetry of Ionizing Radiation 2 (1987) 169–243.
[31] D. Aliaga-Kelly, D.R. Nicoll, Recent developments in scintillation detectors, Nuclear Instruments and Methods 43 (1966) 110–115.
[32] G. Dearnaley, D.C. Northrop, Semiconductor counters for nuclear radiations, Wiley, 1966.
[33] A. Coche, P. Siffert, Lithium Drifted Silicon and Germanium Detectors in Semiconductor Detectors, G. Bertolini and A. Coche, Eds, (1968).
[34] G. Dearnaley, A.B. Whitehead, The semiconductor surface barrier for nuclear particle detection, Nucl. Instrum. Meth. 12 (1961) 205.
[35] F.S. Goulding, Semiconductor detectors for nuclear spectrometry, I, Nucl. Instrum. Meth. 43 (1966) 1.
[36] F.S. Goulding, Y. Stone, Semiconductor radiation detectors, Science (1979) 170 (1970) 280.
[37] A.H.F. Muggleton, Semiconductor devices for gamma ray, X ray and nuclear radiation detection, J Phys E 5 (1972) 390.
[38] P.A. Tove, Review of semiconductor detectors for nuclear radiation, Sensors and Actuators 5 (1984) 103–117.
[39] J.W. Mayer, Semiconductor detectors for nuclear spectrometry, II, Nuclear Instruments and Methods 43 (1966) 55–64.

[40] J.M. Hollander, The impact of semiconductor detectors on gamma-ray and electron spectroscopy, Nuclear Instruments and Methods 43 (1966) 65–109.
[41] H. Hertz, Ueber einen Einfluss des ultravioletten Lichtes auf die electrische Entladung, Ann Phys 267 (1887) 983–1000. https://doi.org/10.1002/ANDP.18872670827.
[42] A. Einstein, Über einen die Erzeugung und Verwandlung des Lichtes betreffenden heuristischen Gesichtspunkt, Ann Phys 322 (1905) 132–148. https://doi.org/10.1002/ANDP.19053220607.
[43] H. Photonics, Photomultiplier Tubes: Basics and Application, 2006.
[44] G.A. Morton, H.M. Smith, H.R. Krall, The Performance of High-Gain First-Dynode Photomultipliers, IEEE Trans Nucl Sci 16 (1969).
[45] G.A. Morton, R.M. Matheson, M.H. Greenblatt, Design of Photomultipliers for the Sub-Millimicrosecond Region, IRE Transactions on Nuclear Science 5 (1958).
[46] G.A. Morton, Nuclear Radiation Detectors, Proceedings of the IRE 50 (1962).
[47] V.K. Zworykin, G.A. Morton, L. Malter, The Secondary Emission Multiplier-A New Electronic Device, Proceedings of the Institute of Radio Engineers 24 (1936).
[48] H.M. Smith, J.E. Ruedy, G.A. Morton, Performance of a Photomultiplier with a Porous Transmission Dynode, IEEE Trans Nucl Sci 13 (1966).
[49] G.A. Morton, H.M. Smith, R. Wasserman, Afterpulses in Photomultipliers, IEEE Trans Nucl Sci 14 (1967).
[50] B.K. Lubsandorzhiev, On the history of photomultiplier tube invention, Nucl Instrum Methods Phys Res A 567 (2006) 236–238.
[51] H. Iams, B. Salzberg, The Secondary Emission Phototube, Proceedings of the Institute of Radio Engineers 23 (1935) 55–64. https://doi.org/10.1109/JRPROC.1935.227243.
[52] V.K. Zworykin, G.A. Morton, L. Malter, Technical papers: The secondary emission multiplier—a new electronic device, Proceedings of the Institute of Radio Engineers 24 (1936) 351–375. https://doi.org/10.1109/JRPROC.1936.226435.
[53] J.R. Young, Some observations on transmission secondary emission, J Appl Phys 28 (1957) 512.
[54] T. Hiruma, PHOTOEMISSIVE MATERIALS-AN INTERFACE BETWEEN PHOTON AND ELECTRON, SAMPE JOURNAL 24 (1988) 35–40.
[55] H. Bruining, Physics and Applications of Secondary Electron Emission, McGraw-Hill Book Co., New York, 1954.
[56] V.K. Zworykin, J.A. Rajchman, The Electrostatic Electron Multiplier, Proceedings of the IRE 27 (1939) 558–566. https://doi.org/10.1109/JRPROC.1939.228753.
[57] A.M. Yakobson, Estimation of the multiplication coefficient of a secondary electron multiplier with a continuous dynode, Radiotekh. Electron 11 (1966) 1825.
[58] K.J. Van Oostrum, CAD in light optics and electron optics, Philips Technical Review 42 (1985) 69–84.
[59] K. Oba, M. Ito, Computer Analysis of the Temporal Properties of a Microchannel Plate Photomultiplier, in: Advances in Electronics and Electron Physics, Elsevier, 1985: pp. 343–354.
[60] H. Bruining, Physics and Applications of Secondary Electron Emission: Pergamon Science Series: Electronics and Waves—a Series of Monographs, Elsevier, 2016.
[61] J.R.M. Vaughan, A new formula for secondary emission yield, IEEE Trans Electron Devices 36 (1989) 1963–1967.
[62] A. Artikov, J. Boudagov, D. Chokheli, G. Drake, M. Gallinaro, M. Giunta, J. Grudzinski, J. Huston, M. Iori, D. Kim, M. Kim, N. Kimura, S. Kuhlmann, S.

Lami, R. Miller, K. Nakamura, L. Nodulman, A. Penzo, K. Sato, J. Suh, N. Turini, F. Ukegawa, Y. Yamada, CDF Central Preshower and Crack Detector Upgrade, (2007). https://arxiv.org/abs/0706.3922v1 (accessed April 4, 2024).
[63] C. Grozis, et al, The time of flight detector at CDF, Nucl Phys B Proc Suppl 93 (2001) 344–347.
[64] E. Kowalski, Nuclear electronics, Springer-Verlag, 2013.
[65] H. Spieler, Semiconductor detector systems, Oxford university press, 2005.
[66] E. Kowalski, Analog-to-Digital Converters, in: Nuclear Electronics, Springer, 1970: pp. 151–212.
[67] E. Kowalski, Radiation Detectors and Related Circuits, in: Nuclear Electronics, Springer, 1970: pp. 4–74.
[68] N. Krihely, SPICE model of photomultiplier tube under different bias conditions, IEEE Sens J 14 (2014) 3606–3610. https://doi.org/10.1109/JSEN.2014.2329181.
[69] PCB Design and Circuit Simulator Software - Proteus, (n.d.). https://www.labcenter.com/ (accessed June 7, 2022).
[70] What is Arduino? | Arduino, (n.d.). https://www.arduino.cc/en/Guide/Introduction (accessed May 3, 2024).
[71] S.N. Ahmed, Physics and Engineering of Radiation Detection, 2015.
[72] S. Liao, R. Erasmus, H. Jivan, C. Pelwan, G. Peters, E. Sideras-Haddad, A comparative study of the radiation hardness of plastic scintillators for the upgrade of the Tile Calorimeter of the ATLAS detector, J Phys Conf Ser 645 (2015) 012021. https://doi.org/10.1088/1742-6596/645/1/012021.
[73] P. Perret, X. Vilasís-Cardona, (on behalf ofthe LHCb Collaboration), Performance of the LHCb calorimeters during the period 2010-2012, J Phys Conf Ser 587 (2015) 012012. https://doi.org/10.1088/1742-6596/587/1/012012.
[74] V. Khachatryan, et. al., Dose rate effects in the radiation damage of the plastic scintillators of the CMS hadron endcap calorimeter, Journal of Instrumentation 11 (2016) T10004. https://doi.org/10.1088/1748-0221/11/10/T10004.
[75] B. Bilki, Secondary emission calorimetry R and D, 2014 IEEE Nuclear Science Symposium and Medical Imaging Conference, NSS/MIC 2014 (2016). https://doi.org/10.1109/NSSMIC.2014.7431155.
[76] A. Albayrak-Yetkin, B. Bilki, J. Corso, P. Debbins, G. Jennings, V. Khristenko, A. Mestvirisvilli, Y. Onel, I. Schmidt, C. Sanzeni, D. Southwick, D.R. Winn, T. Yetkin, Secondary Emission Calorimetry: Fast and Radiation-Hard, (2013).
[77] R.G. Lye, A.J. Dekker, Theory of Secondary Emission, Physical Review 107 (1957) 977.

# APPENDIX A

**Table 0.1 C# Code**

```
     using System;
     using System.Collections.Generic;
     using System.ComponentModel;
     using System.Data;
     using System.Drawing;
     using System.Linq;
     using System.Text;
     using System.Threading.Tasks;
     using System.Windows.Forms;

     namespace Controller1
     {
         public partial class Form1 : Form
         {
             public Form1()
             {
                 InitializeComponent();
                 serialPort1.Open();
             }
             private void Mode1On_Click(object sender, EventArgs e)
             {
                 // Sent command to the arduino to turn Mode1 on
                 serialPort1.Write("A");
                 textBox1.Text = "Now Mode 1 is Active!";
                 // Add Image
                 PictureBoxModes.Image = new
Bitmap("C:\\Users\\npara\\Desktop\\ModeImages\\Mode1HImage.jpg");
             }
             private void Mode2On_Click(object sender, EventArgs e)
             {
                 // Sent command to the arduino to turn Mode2 on
                 serialPort1.Write("B");
                 textBox1.Text = "Now Mode 2 is Active!";
                 // Add Image
                 PictureBoxModes.Image = new
Bitmap("C:\\Users\\npara\\Desktop\\ModeImages\\Mode2HImage.jpg");
             }
             private void Mode3On_Click(object sender, EventArgs e)
             {
                 // Sent command to the arduino to turn Mode3 on
                 serialPort1.Write("C");
                 textBox1.Text = "Now Mode 3 is Active!";
                 // Add Image
                 PictureBoxModes.Image = new
Bitmap("C:\\Users\\npara\\Desktop\\ModeImages\\Mode3HImage.jpg");
             }
             private void textBox1_TextChanged(object sender, EventArgs e)
             {
             }
             private void label1_Click(object sender, EventArgs e)
             {

             }
         }
     }
```

# APPENDIX B

**Table 0.2 C++ Code**

```
String data;
char dl;

void setup() {
  // put your setup code here, to run once:
Serial.begin(9600);
pinMode(11, OUTPUT);
pinMode(12, OUTPUT);
pinMode(13, OUTPUT);

}

void loop() {
  // put your main code here, to run repeatedly:
  if(Serial.available()){
    data = Serial.readString();
    dl = data.charAt(0);
    if(dl=='C') {
      digitalWrite(11, HIGH);
      digitalWrite(12, LOW);
      digitalWrite(13, HIGH);
      }
      if(dl=='B') {
      digitalWrite(11, LOW);
      digitalWrite(12, HIGH);
      digitalWrite(13, LOW);
      }
    else if (dl == 'A'){
      digitalWrite(11, LOW);
      digitalWrite(12, LOW);
      digitalWrite(13, LOW);
    }
  }
}
```

# CURRICULUM VITAE

| | |
|---|---|
| 2006 – 2011 | B.Sc., Physics, Erciyes University, Kayseri, Türkiye |
| 2011 – 2016 | M.Sc., Physics, Erciyes University, Kayseri, Türkiye |
| 2018 – Present | Ph.D., Electrical and Computer Engineering, Abdullah Gül University, Kayseri, Türkiye |

**SELECTED PUBLICATIONS AND PRESENTATIONS**

**J1)** Paran N., Tiras E., Tekgun B., Abubakar S., Development and Radiation Test of a Secondary Emission Ionization Calorimetry Module, Radiation Measurements, (Submitted – Under Review).

**J2**) Paran N., Ertaş M., Nonequilibrium Hysteresis Properties of Double Perovskite Sr2FeMoO6: Glauber dynamics approach, Physica A: Statistical Mechanics and its Applications, (Submitted – Under Review).

**J3**) Paran N., Ertaş M., Nonequilibrium phase diagrams in a multilayer Ising ferrimagnet system: The Glauber type stochastic dynamics approach, Chinese Journal Of Physics, cilt.89, p.980-990, 2024.

**J4**) Şarlı N., Paran N., Ablay G., Ocak H. Y., Yıldız Y. G., Dikici Yıldız D.Key role of high-Tc twinned martensitic materials to gain a magnetic actuation higher than 15% Sensors and Actuators A: Physicalcilt.332, ss.1-7, 2021.

**C1)** Paran N., Tıraş E., Tekgün B., Abubakar S., Cosmic and Gamma Radiation Test of a Developed Secondary Emission Ionization Calorimetry Module, 11th International Conference on Material Science and Nanotechnology for Next Generation (MSNG-2024), Çanakkale, Türkiye, 22-25 May 2024, p.1-2

**C2)** Paran N., Tıraş E., Tekgün B., Abubakar S., Akar M., İkincil Emisyon İyonizasyon Kalorimetresi için ArGe Çalışamaları, YEFİST 2024 İstanbul Yüksek Enerji Fiziği Çalıştayı, İstanbul, Türkiye, 18-19 May 2024, p.14-15